DEVELOPMENT OF FUNCTIONAL NEAR-INFRARED OPTICAL COHERENCE TOMOGRAPHY

ACADEMISCH PROEFSCHRIFT

ter verkrijging van de graad van doctor
aan de Universiteit van Amsterdam
op gezag van de Rector Magnificus
prof. Dr. D.C. van den Boom
ten overstaan van een door het college voor promoties
ingestelde commissie,
in het openbaar te verdedigen in de Agnietenkapel
op woensdag 14 maart 2012, te 14:00 uur

door

Vitali Mikhailovich Kodach

geboren te Grodno, Wit-Rusland

Promotor: Prof. dr. A.G.J.M. van Leeuwen

Co-promotores: Dr. J. Kalkman
Dr. ir. D.J. Faber

Overige Leden: Prof. dr. ir. M.J.C. van Gemert
Prof. dr. C.J.F. van Noorden
Prof. dr. J.F. de Boer
Prof. dr. A.F.W. van der Steen
Dr. E.A.J.M. Bente

Faculteit der Geneeskunde

TABLE OF CONTENTS

CHAPTER 1

Introduction

Medical imaging is a discipline where the fields of mathematics, physics, biology, and medicine are combined in the acquisition, computation and interpretation of three-dimensional images of (human) tissue. A variety of imaging modalities that provide information about morphological structure and function of biological tissues has been developed. These modalities are based on electromagnetic waves (magnetic resonance imaging, X-ray computed tomography, confocal microscopy), sound (ultrasonography), or nuclear tracers (positron emission tomography, single photon emission computed tomography). In the last decades, these medical imaging modalities have become a key tool in disease diagnosis, treatment monitoring, and disease prevention.

Compared to other imaging techniques, optical imaging is low-cost, can be used in non-contact arrangements, has a small form factor, and does not use ionizing radiation. The main disadvantage is its limited imaging depth, which is caused by the strong scattering of light in biological tissues.

Optical coherence tomography (OCT) is a relatively new optical imaging technique. OCT is the optical analogue of ultrasound imaging, in which light (instead of acoustic waves) backscattered from tissue structures is detected. Due to the high speed of light, the path length that the light has travelled into the tissue is determined using low-coherence interferometry (instead of time of fight as for acoustic pulses) [1]. With OCT, high resolution (2-10 µm) cross-sectional images of biological tissues up to 1-2 mm deep can be acquired. Figure 1-1 shows an overview of many medical imaging modalities based on their imaging

depth and spatial resolution. As can be seen, OCT fills up the gap that is present between confocal microscopy and high frequency ultrasound.

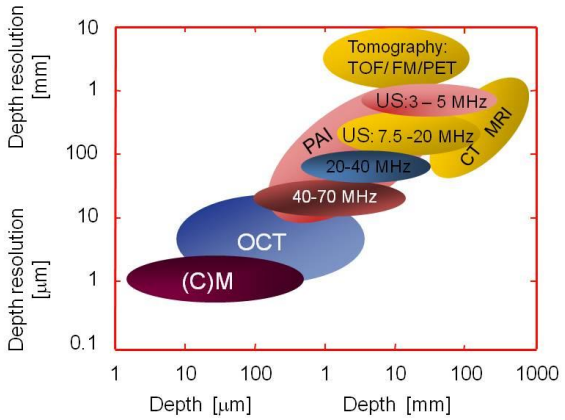

Figure 1-1. Axial (depth) resolution and obtainable imaging depth for biomedical imaging modalities: single photon emission computed tomography (SPECT), positron emission tomography (PET), X-rays computed tomography (CT), magnetic resonance imaging (MRI), ultrasound (US) (various frequencies), photoacoustic imaging (PAI), optical coherence tomography (OCT) and (confocal) microscopy ((C)M).

OCT has found many applications in medicine, e.g. in ophthalmology, where cross-sectional retinal imaging provides previously inaccessible information about the condition of the retina. OCT is also used for visualization of the anterior segment of the eye, which is particularly important in the diagnosis of glaucoma. Using a fiber optic probe, OCT can also be applied endoscopically. Imaging of (vulnerable) plaques, imaging of stent placement, and characterization of the structural integrity of the vasculature in the coronary artery provide valuable information for diagnosis and treatment of vascular diseases. Currently, OCT is being evaluated in many fields of medicine, including dentistry, dermatology, urology, and developmental biology [2-14].

The field of OCT is a continuously developing cycle, in which clinical applications lead to more research, which leads to improved technology, which opens up new applications. Furthermore, besides imaging, different features of the backscattered light can be analyzed, for example its spectral content, polarization state, and Doppler shift, which can be used to determine functional parameters of the tissue as blood oxygen saturation, tissue birefringence and blood flow, respectively [15-21]. Consequently, next to the improvement of OCT system performance, also the extraction of more functional, i.e. morphological and/or physiological information, from the OCT signal is currently being investigated.

OCT PRINCIPLE

In its most basic form, OCT is based on low coherence interferometry with a Michelson interferometer. Figure 1-2 shows a schematic representation of a time-domain OCT (TD-OCT) setup. A collimated beam from a light source is split into a reference and sample arm. Light, back-reflected by the scanning mirror in the reference arm, and backscattered from the tissue

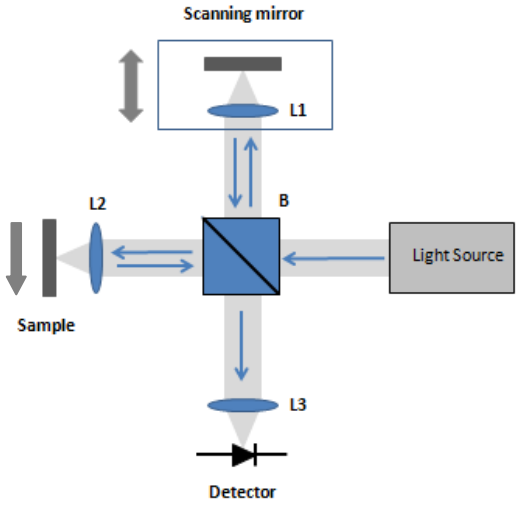

Figure 1-2. Schematic drawing of Michelson interferometer based OCT setup. B – beamsplitter; L1, L2 and L3 are reference, sample and detector arm lenses correspondingly.

under study in the sample arm, is combined and directed on the photo detector. The electric field at the detector is the sum of the sample E_S and reference arm E_R fields. The detector measures the intensity of the detected light I_D, which, in case of a single reflector in the sample arm and a monochromatic light source, is proportional to the square of the total field given by:

$$I_D \sim |E_R|^2 + |E_S|^2 + 2E_R E_S \cos(k\Delta L) \quad (1\text{-}1)$$

where ΔL is the optical path length difference between the reference and sample arms of the interferometer, and k is the wave number [22]. For a broadband light source as used in OCT, equation 1-1 is integrated over the source spectrum. If the reference arm is scanned, interference fringes are generated as a function of time as long as the optical path length difference ΔL is within the coherence length of the light source. The frequency of the interference signal is determined by the reference mirror velocity and the wavelength of the light, the amplitude of the interference signal is determined by the backscattering properties of the sample. Note that the first two terms in Equation 1-1 describe the DC offset of the signal, which in general is rejected by band-pass filtering and/or lock-in detection at the modulation frequency. The third term is the interferometric signal, containing information about the depth-dependent reflectivity of the sample. In a time-domain OCT system without focus tracking, the

OCT detector current $i_d(\Delta L)$ is equal to the field-backscatter profile of the sample $r(z)$ as function of depth z ($z=\Delta L/2n$) convoluted with the complex coherence function $\gamma(\Delta L/c)$ [23]. The OCT detector current signal as a function of z is given by

$$i_d(z) = \eta \,\mathrm{Re}\left\{\gamma\left(\frac{2zn}{c}\right)\right\} \otimes h(z)r(z)\sqrt{P_r P_s} \tag{1-2}$$

where η is the detector conversion factor from the incident light power to the electric current, $Re\{\}$ is the real part of the complex coherence function, n is the refractive index of the medium, c is the speed of light in vacuum, $h(z)$ is the confocal point spread function describing the change of the OCT signal as a function of distance between the probed location z in the sample and the focus position z_0 [24]. The powers P_r and P_s are the powers from the reference and sample arm, respectively. Since the reference mirror position at each moment is known, i.e. ΔL is controlled, the in-depth image of a sample can be reconstructed as a function of z by longitudinal scanning of the reference arm. Finally, a three-dimensional image of the sample can be obtained by lateral scanning of the sample to acquire a 2D array of depth scans.

The axial resolution in medium with refractive index n is determined by the central wavelength λ_0 of the light source. Assuming a Gaussian shaped spectrum with a full width at half maximum spectral bandwidth $\Delta\lambda$, the axial resolution δz can be calculated as:

$$\delta z = \frac{2\ln 2\lambda_0^2}{n\pi\Delta\lambda} \tag{1-3}$$

The lateral resolution of the OCT system is decoupled from the axial resolution and is determined by the focusing optics of the sample arm. Assuming a Gaussian beam with diameter D ($1/e^2$ width), focused by the lens with focal length f, diameter of the focal spot is calculated as:

$$\delta x = \frac{4\lambda_0 f}{\pi D} \tag{1-4}$$

FOURIER-DOMAIN OCT

A superior approach to the depth ranging using a moving reference mirror is the acquisition of the interferometric signal as a function of the optical wavenumber with a fixed group delay [25]. This method, called Fourier-domain OCT, has two forms. Spectral-domain OCT (SD-OCT) uses a broadband light source and a spectrometer in the detection arm to detect the interference spectrum [26]. The second approach, swept-source OCT (SS-OCT), employs the single detector in the detector arm (similar to TD-OCT), but instead of a broadband light source,

a wavelength sweeping laser is used [27-29]. The swept laser has a narrow instantaneous linewidth, which is rapidly tuned through a broad optical bandwidth.

In Fourier-domain OCT, a single reflector in the sample arm results in a periodic fringe in the *k*-space domain whose frequency and amplitude are directly proportional to the depth and reflectance of the sample, respectively. In the case of multiple reflectors, a multitude of sinusoids are superimposed. The reflection coefficient from all depths can be simultaneously determined by Fourier transformation of the measured interference spectrum.

The maximum imaging depth z_{max} in Fourier-domain OCT is determined as:

$$z_{\max} = \frac{\lambda_0^2}{4n\delta\lambda} \tag{1-5}$$

where $\delta\lambda$ is the sampling wavelength interval.

Fourier-Domain OCT has several advantages over TD-OCT. First of all, the absence of a mechanically scanned mirror in the reference arm makes higher data acquisition rates possible. Second, Fourier-domain OCT measures all depths simultaneously. Thirdly, the sensitivity of FD-OCT is higher than TD-OCT. Typically FD-OCT has 20-30 dB better sensitivity than TD-OCT (for the same data acquisition rate) [30-32]. In practice, the sensitivity advantage of FD-OCT is used to increase the imaging speed, which is especially useful for measurements on humans.

For SS-OCT the development of rapid swept lasers with large bandwidths and high output powers is required. Although the stationary mirror in the reference arm and single photo detector in the detector arm simplify the optical design of the OCT system, all complexity is moved to the design of the swept light source. To achieve high axial resolution in OCT applications, the swept laser should have a broad spectral output. For large imaging depths a narrow instantaneous linewidth is required which preferably is much smaller than the sampling wavelength interval (equation 1-5), otherwise the fringe visibility becomes very small at the maximum imaging depth. Finally, for in-vivo imaging, high sweep rates are needed. Still, comparing SD-OCT and SS-OCT, swept-source OCT is a more advantageous method due to the larger depth range (smaller instantaneous linewidths are easily achieved), the possibility to do balanced detection for a suppression of the relative intensity noise, and compact OCT layout.

To achieve good sweeping performance, different lasers and different tuning techniques are demonstrated. In general, OCT applications require lasers with a broad emission spectrum (e.g. dye, semiconductors, Ti:Sapphire gain material). Tuning can be performed mechanically or electronically, for which the latter is preferred due to a more stable performance. However, the time necessary to build-up lasing from the spontaneous emission is a fundamental limitation in the maximum achievable sweeping rate [33]. Recently, significant advantage in the field of the

swept laser is achieved by the demonstration of Fourier-domain mode-locking (FDML) lasers with sweeping rates up to 5.2 MHz [34-36]. In this technique, lasers are based upon a cavity with a long optical delay line (~km) and synchronously tune a narrowband filter with the round-trip time of the cavity. Although FDML lasers demonstrate advanced sweeping performance, the development of new types of swept lasers continues [37, 38], and issues related to the optimization of such lasers in terms of prize, form factor, and performance for OCT applications still need to be addressed.

LIGHT-TISSUE INTERACTION

The interaction of light with tissue occurs through scattering and absorption. The overall effect of these processes is the attenuation of ballistic light in depth, which can be described by the attenuation coefficient μ_t:

$$\mu_t = \mu_s + \mu_a \tag{1-6}$$

where μ_s is the scattering coefficient, and μ_a is the absorption coefficient. In the near infrared part of the optical spectrum, the majority of biological tissues are highly scattering media with the scattering coefficients larger than the absorption coefficients. However, for longer near infrared wavelengths the increased light absorption by water also becomes a significant factor of light attenuation (Figure 1-3).

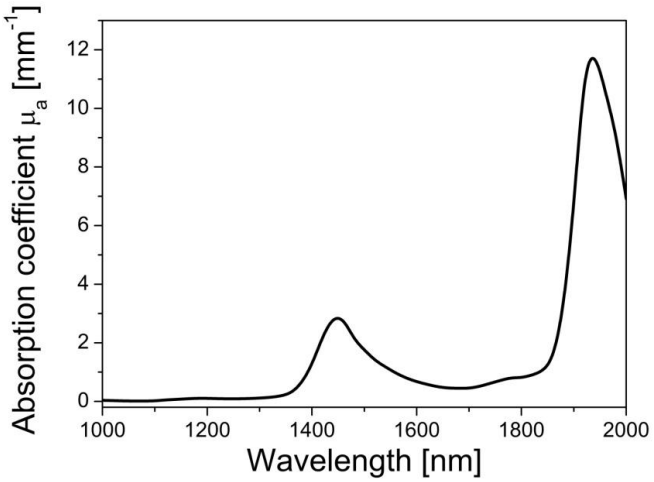

Figure 1-3. The light absorption coefficient of water as a function of wavelength.

Due to the low coherence path length selection and the confocal gating by the sample arm optics, OCT is mostly based on light that has scattered once (in the backward direction).

Consequently, for superficial tissue layers with low scattering coefficients, the single scattering model is appropriate to describe the light attenuation. In this case the ballistic light intensity is described by the law of Lambert-Beer and attenuates exponentially with depth:

$$I(z) = I_0 \exp(-\mu_t z) \tag{1-7}$$

where I_0 is the intensity of the light at the tissue surface, and $I(z)$ is the intensity at depth z. For OCT, the single scattering model results in a detected OCT signal that is described as [39]:

$$i_d(z) \propto \sqrt{\exp(-2\mu_t z)} \tag{1-8}$$

The factor 2 in the exponent is caused by the double path length the detected light travels through the scattering medium, and the square root is because the detector current is proportional to the sample field rather than sample intensity (Equation 1-2).

Scattering by a single particle is characterized by the scattering cross-section σ_s, which describes the light scattering capability in units of cross sectional area. The larger the cross-section, the more likely the scattering occurs. The scattering coefficient of a sample containing many scatterers is the product of the scattering cross-section σ_s and the number of scatterers N per unit volume:

$$\mu_s = N\sigma_s \tag{1-9}$$

In case of high concentration of scatterers the scattering coefficient typically is lower and is described in more complicated way, which will be discussed in Chapter 7.

Classical light scattering theory for small particles was derived by Rayleigh. For spherical particles with a diameter much smaller than the wavelength of the incident light, the scattering cross-section is:

$$\sigma_s = \frac{2\pi^5}{3}\frac{d^6}{\lambda^4}\left(\frac{m^2-1}{m^2+2}\right)^2 \tag{1-10}$$

where d is the particle diameter, and m is the relative refractive index, i.e. the ratio of the (complex) refractive index of the particle to the refractive index of a medium. As can be seen, Rayleigh scattering is strongly dependent on the wavelength of light: the scattering cross-section is inversely proportional to fourth power of wavelength.

For scatterers comparable to or larger than the wavelength of light, the Rayleigh light scattering theory breaks down. In this case, light scattering can be described by solving Maxwell's equations, for which the exact solution for light scattering by a single sphere was given by Mie. Mie theory is applicable for the scattering from spherical, homogeneous, isotropic and non-magnetic particles in a non-absorbing medium. The wavelength-dependence

of Mie scattering is more complex than Rayleigh scattering. In general, the scattering decreases with increasing wavelength of the incident light at a lower rate than for Rayleigh scattering.

The scattering process induces a change in the direction of light propagation that can be described by the angle θ, which is the angle between directions of propagation of incident and scattered light. Depending on the particle size and wavelength of the incident light, a particle has its own scattering profile, which is called the scattering phase function $p(\theta)$. The phase function is a normalized probability distribution as a function of the scattering angle. Plotted in polar coordinates as a function of θ, it represents the scattering diagram of the particle (Figure 1-4).

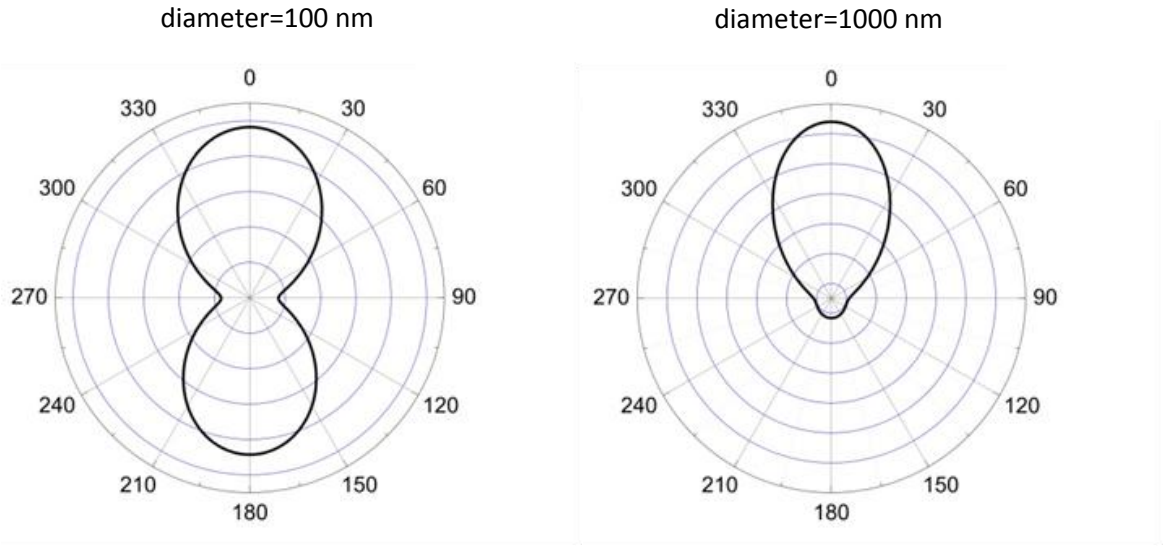

Figure 1-4. Examples of scattering diagram for polystyrene particles with diameters of 100nm (left) and 1000nm (right) for unpolarized light at 1300nm.

To characterize the angle-dependent scattering properties of scatterers in a more simple way, the scattering anisotropy parameter g is used. By definition, the scattering anisotropy parameter g is the average of the cosine of the scattering angle over the phase function:

$$g = \int_0^{\pi} p(\theta)\cos(\theta)2\pi\sin(\theta)d\theta = \langle \cos\theta \rangle \tag{1-11}$$

The scattering anisotropy g provides information about the dominant direction of scattering. The value of g can be in the range from -1 to 1. If forward scattering dominates, then g approaches 1; g approaching 0 represents equal scattering in forward and backward direction, e. g. for Rayleigh scattering.

The scattering coefficient μ_s gives information about the number of scatterers, the size of the scatterer, and differences in the refractive index between the scatterer and its environment. The scattering anisotropy parameter g gives information about the size of the scatterer. Thus, the scattering properties contain diagnostically valuable information on the tissue structure and composition. For example, changes in the tissue morphology can lead to changes in the scattering coefficient, and changes in the tissue composition can lead to changes in the tissue refractive index and the absorption coefficient. Consequently, using carefully calibrated OCT systems, we can measure changes in the optical properties and relate these changes to functional processes in biological tissues, which can be used for tissue diagnostic purposes. As an example, development of cancer involves morphological transformation of the cell architecture, i.e. increase of the nuclei size and increase of the amount of cells, which leads to changes in optical properties [5, 13, 40-42].

OCT IMAGING DEPTH IMPROVEMENT

Besides spatial resolution and imaging speed, the OCT imaging depth is an important characteristic of OCT performance. OCT is a superficial imaging technique with a depth range of 1-2 mm in scattering tissue. For many applications, improvements in the imaging depth can open new possibilities and application areas. As an example, in ophthalmology, imaging of the anterior segment of the eye is important for early diagnosis of eye diseases, in particular glaucoma. Glaucoma is the disease that is associated with elevated intraocular pressure. Elevation of the intraocular pressure results from an imbalance between the production and drainage of aqueous fluid [43-45] and is caused by the closure of the angle between iris and cornea. As a result, Schlemm's drainage channel becomes blocked and results in an increase of the intraocular pressure. Visualization of this area of the anterior segment is difficult due to the highly scattering sclera. OCT systems with improved imaging depth can be successful in imaging of this part of the eye.

One of the possibilities to increase the OCT imaging depth is to use longer imaging wavelengths, for which scattering is lower. The advantage of using longer wavelengths was recognized, and, after the first OCT systems operating at wavelengths around 800 nm, OCT at wavelengths around 1300 nm and 1050 nm were introduced [46-49]. Clear improvement in the OCT imaging depth was demonstrated, and currently 1300 nm OCT systems are routinely used in the clinic. Further improvement of the imaging depth can be achieved with longer wavelengths. However, with increasing wavelength the light absorption by water increases, see

Figure 1-3 [50]. Until approximately 1360 nm the absorption is relatively low and has negligible influence on the light attenuation. However, the water absorption peak at 1460 nm results into an increase in absorption to 2.9 mm^{-1}. Consequently, for wavelengths larger than 1360 nm the light penetration is governed by both absorption and scattering, and the optimal wavelength depends on the relative contribution of the two effects.

The 1600-1800 nm spectral range presents an opportunity for increased OCT imaging depth as the absorption is relatively low (only 0.67 mm^{-1} at 1600 nm compared to 0.11 mm^{-1} at 1300 nm) and scattering is much lower compared to the 1300 nm window. Consequently, for some biological tissues, the decrease in scattering can be larger than the increase in the absorption by water, which can results in an enhanced OCT imaging depth. The reported optical properties of some biological tissues in the NIR spectral range suggest that such enhancement is possible [51-54], which was supported by comparative studies of the OCT light imaging depth at different wavelengths [55, 56]. However, quantification of the imaging depth is difficult because the OCT system performance has to be well calibrated for the imaging wavelengths that are used in the comparison.

SCOPE OF THIS THESIS

In this thesis, entitled “Development of functional near-infrared OCT”, the potential of OCT for improved imaging depth and for additional tissue analysis is investigated. In Chapter 2, we investigated potential wavelength bands for OCT imaging depth improvement by performing an analysis of the wavelength-dependent NIR light penetration depth. The proposed imaging depth quantification formalism is tested using Intralipid optical transmission measurements, and is applied to three kinds of biological tissues. In Chapter 3, the OCT imaging depth is quantified and measured around 1300 nm and 1600 nm using a TD-OCT setup of which the technical characteristics at the two wavelength regions are matched. The next two chapters focus on methods to extract functional information from the OCT signal. In particular, we focused on measurements of light backscattering characteristics of tissue phantoms (Chapter 4) and cells (Chapter 5). In Chapter 4 we determined the relation between the OCT signal amplitude and the scattering anisotropy g. Chapter 5 shows OCT measurements of the optical properties of the thin samples: absolute measurements of the scattering coefficient in thin phantoms, and measurements of relative changes in the backscattering in a single layer of retinal pigment epithelium (RPE) cells during the development of apoptosis. Chapter 6 describes the construction of a swept laser and its fundamental performance characteristics. A swept Ti:Sapphire laser with intracavity acousto-optic tunable filter that we developed is investigated, mainly focusing on the possibilities for optimization of the sweeping performance for application to SS-OCT. Finally, Chapter 7 provides a general discussion and conclusions.

REFERENCES

1. D. Huang, E. A. Swanson, C. P. Lin, J. S. Schuman, W. G. Stinson, W. Chang, M. R. Hee, T. Flotte, K. Gregory, C. A. Puliafito, and J. G. Fujimoto, "Optical Coherence Tomography," Science **254**, 1178-1181 (1991).
2. B. Cense, N. A. Nassif, T. Chen, M. Pierce, S. H. Yun, B. H. Park, B. E. Bouma, G. J. Tearney, and J. F. de Boer, "Ultrahigh-resolution high-speed retinal imaging using spectral-domain optical coherence tomography," Optics Express **12**, 2435-2447 (2004).
3. M. E. J. van Velthoven, D. J. Faber, F. D. Verbraak, T. G. van Leeuwen, and M. D. de Smet, "Recent developments in optical coherence tomography for imaging the retina," Progress in Retinal and Eye Research **26**, 57-77 (2007).
4. A. M. Zysk, F. T. Nguyen, A. L. Oldenburg, D. L. Marks, and S. A. Boppart, "Optical coherence tomography: a review of clinical development from bench to bedside," Journal of Biomedical Optics **12** (2007).
5. F. J. van der Meer, D. J. Faber, D. M. B. Sassoon, M. C. Aalders, G. Pasterkamp, and T. G. van Leeuwen, "Localized measurement of optical attenuation coefficients of atherosclerotic plaque constituents by quantitative optical coherence tomography," IEEE Transactions on Medical Imaging **24**, 1369-1376 (2005).
6. T. Gambichler, G. Moussa, M. Sand, D. Sand, P. Altmeyer, and K. Hoffmann, "Applications of optical coherence tomography in dermatology," Journal of Dermatological Science **40**, 85-94 (2005).
7. M. C. Pierce, J. Strasswimmer, B. H. Park, B. Cense, and J. F. de Boer, "Advances in optical coherence tomography imaging for dermatology," Journal of Investigative Dermatology **123**, 458-463 (2004).
8. L. L. Otis, M. J. Everett, U. S. Sathyam, and B. W. Colston, "Optical coherence tomography: A new imaging technology for dentistry," Journal of the American Dental Association **131**, 511-+ (2000).
9. R. S. Jones, C. L. Darling, J. D. B. Featherstone, and D. Fried, "Remineralization of in vitro dental caries assessed with polarization-sensitive optical coherence tomography," Journal of Biomedical Optics **11** (2006).
10. K. Messeih, W. Waite, W. G. Jung, U. Schoop, Z. Chen, and P. Wilder-Smith, "Non-invasive, high-resolution optical coherence tomography for the early detection of dental caries," Lasers in Surgery and Medicine, 69-69 (2004).
11. X. J. Wang, T. E. Milner, J. F. de Boer, Y. Zhang, D. H. Pashley, and J. S. Nelson, "Characterization of dentin and enamel by use of optical coherence tomography," Applied Optics **38**, 2092-2096 (1999).
12. K. Barwari, D.M.de Bruin, E.C.C. Cauberg, D. J. Faber, T. G. van Leeuwen, H. Wijkstra, J. de la Rosette, and M. Pilar Laguna, "Advanced Diagnostics in Renal Mass Using Optical Coherence Tomography: A Preliminary Report," Journal of Endourology **25**, 311-315 (2011).
13. E. C. C. Cauberg, D. M. de Bruin, D. J. Faber, T. M. de Reijke, M. Visser, J. J. M. C. H. de la Rosette, and T. G. van Leeuwen, "Quantitative measurement of attenuation coefficients of bladder biopsies using optical coherence tomography for grading urothelial carcinoma of the bladder," Journal of Biomedical Optics **15**, 066013-066016.
14. Z. Hu, and A. Rollins, "Quasi-telecentric optical design of a microscope-compatible OCT scanner," Opt. Express **13**, 6407-6415 (2005).
15. A. Baumgartner, S. Dichtl, C. K. Hitzenberger, H. Sattmann, B. Robl, A. Moritz, Z. F. Fercher, and W. Sperr, "Polarization-sensitive optical coherence tomography of dental structures," Caries Research **34**, 59-69 (2000).
16. M. J. Everett, K. Schoenenberger, B. W. Colston, and L. B. Da Silva, "Birefringence characterization of biological tissue by use of optical coherence tomography," Optics Letters **23**, 228-230 (1998).

17. D. J. Faber, E. G. Mik, M. C. G. Aalders, and T. G. van Leeuwen, "Toward assessment of blood oxygen saturation by spectroscopic optical coherence tomography," Optics Letters **30**, 1015-1017 (2005).
18. D. J. Faber, M. C. G. Aalders, E. G. Mik, B. A. Hooper, M. J. C. van Gemert, and T. G. van Leeuwen, "Oxygen saturation-dependent absorption and scattering of blood," Physical Review Letters **93** (2004).
19. D. J. Faber, E. G. Mik, M. C. G. Aalders, and T. G. van Leeuwen, "Light absorption of (oxy-)hemoglobin assessed by spectroscopic optical coherence tomography," Optics Letters **28**, 1436-1438 (2003).
20. Y. H. Zhao, Z. P. Chen, C. Saxer, S. H. Xiang, J. F. de Boer, and J. S. Nelson, "Phase-resolved optical coherence tomography and optical Doppler tomography for imaging blood flow in human skin with fast scanning speed and high velocity sensitivity," Optics Letters **25**, 114-116 (2000).
21. J. M. Schmitt, S. H. Xiang, and K. M. Yung, "Differential absorption imaging with optical coherence tomography," Journal of the Optical Society of America A-Optics Image Science and Vision **15**, 2288-2296 (1998).
22. R. P. Earhart, and T. E. Parker, "Least-mean-squares algorithm to determine submicrometer particle diameter, volume fraction, and size distribution width by elastic light scattering," Applied Optics **41**, 4421-4431 (2002).
23. J. W. Goodman, *Statistical optics* (Wiley, New York, 1985).
24. T. G. van Leeuwen, D. J. Faber, and M. C. Aalders, "Measurement of the axial point spread function in scattering media using single-mode fiber-based optical coherence tomography," IEEE Journal of Selected Topics in Quantum Electronics **9**, 227-233 (2003).
25. A. F. Fercher, C. K. Hitzenberger, G. Kamp, and S. Y. Elzaiat, "Measurement of Intraocular Distances by Backscattering Spectral Interferometry," Optics Communications **117**, 43-48 (1995).
26. M. Wojtkowski, A. Kowalczyk, R. Leitgeb, and A. F. Fercher, "Full range complex spectral optical coherence tomography technique in eye imaging," Optics Letters **27**, 1415-1417 (2002).
27. S. R. Chinn, E. A. Swanson, and J. G. Fujimoto, "Optical coherence tomography using a frequency-tunable optical source," Optics Letters **22**, 340-342 (1997).
28. S. H. Yun, G. J. Tearney, J. F. de Boer, N. Iftimia, and B. E. Bouma, "High-speed optical frequency-domain imaging," Optics Express **11**, 2953-2963 (2003).
29. F. Lexer, C. K. Hitzenberger, A. F. Fercher, and M. Kulhavy, "Wavelength-tuning interferometry of intraocular distances," Applied Optics **36**, 6548-6553 (1997).
30. M. A. Choma, M. V. Sarunic, C. H. Yang, and J. A. Izatt, "Sensitivity advantage of swept source and Fourier domain optical coherence tomography," Optics Express **11**, 2183-2189 (2003).
31. R. Leitgeb, C. K. Hitzenberger, and A. F. Fercher, "Performance of fourier domain vs. time domain optical coherence tomography," Optics Express **11**, 889-894 (2003).
32. J. F. de Boer, B. Cense, B. H. Park, M. C. Pierce, G. J. Tearney, and B. E. Bouma, "Improved signal-to-noise ratio in spectral-domain compared with time-domain optical coherence tomography," Optics Letters **28**, 2067-2069 (2003).
33. R. Huber, M. Wojtkowski, K. Taira, J. G. Fujimoto, and K. Hsu, "Amplified, frequency swept lasers for frequency domain reflectometry and OCT imaging: design and scaling principles," Optics Express **13**, 3513-3528 (2005).
34. R. Huber, M. Wojtkowski, and J. G. Fujimoto, "Fourier Domain Mode Locking (FDML): A new laser operating regime and applications for optical coherence tomography," Optics Express **14**, 3225-3237 (2006).
35. R. Huber, D. C. Adler, and J. G. Fujimoto, "Buffered Fourier domain mode locking: unidirectional swept laser sources for optical coherence tomography imaging at 370,000 lines/s," Optics Letters **31**, 2975-2977 (2006).

36. W. Wieser, B. R. Biedermann, T. Klein, C. M. Eigenwillig, and R. Huber, "Multi-Megahertz OCT: High quality 3D imaging at 20 million A-scans and 4.5 GVoxels per second," Optics Express **18**, 14685-14704.
37. A. Silva, K. J. Boller, and I. D. Lindsay, "Wavelength-swept Yb-fiber master-oscillator-power-amplifier with 70nm rapid tuning range," Optics Express **19**, 10511-10517.
38. Y. J. B.W. Tilma, J.Kotani, E.Smalbrugge, H.P.M.M.Ambrosius, P.J.Thijs, X.J.M.Leijtens, R.Notzel, M.K.Smit, and E.A.J.M.Bente, "Integrated tunable quantum-dot laser for optical coherence tomography in the 1.7 um wavelength region," IEEE Journal of Quantum Electronics **47** (2011).
39. D. J. Faber, F. J. van der Meer, and M. C. G. Aalders, "Quantitative measurement of attenuation coefficients of weakly scattering media using optical coherence tomography," Optics Express **12**, 4353-4365 (2004).
40. M. Mogensen, and G. B. E. Jemec, "Diagnosis of non-melanoma skin cancer with Optical Coherence Tomography," Journal of Investigative Dermatology **126**, S47-S47 (2006).
41. W. G. Jung, J. Zhang, J. R. Chung, P. Wilder-Smith, M. Brenner, J. S. Nelson, and Z. P. Chen, "Advances in oral cancer detection using optical coherence tomography," IEEE Journal of Selected Topics in Quantum Electronics **11**, 811-817 (2005).
42. P. F. Escobar, J. L. Belinson, A. White, N. M. Shakhova, F. I. Feldchtein, M. V. Kareta, and N. D. Gladkova, "Diagnostic efficacy of optical coherence tomography in the management of preinvasive and invasive cancer of uterine cervix and vulva," International Journal of Gynecological Cancer **14**, 470-474 (2004).
43. R. Ursea, and R. H. Silverman, "Anterior-segment imaging for assessment of glaucoma," Expert review of ophthalmology, 2010, **5**, pp. 59-74. pp. 59-74.
44. A. Konstantopoulos, P. Hossain, and D. F. Anderson, "Recent advances in ophthalmic anterior segment imaging: a new era for ophthalmic diagnosis?," British Journal of Ophthalmology,(2007), **91**, pp. 551-557.
45. S. Radhakrishnan, A. M. Rollins, J. E. Roth, S. Yazdanfar, V. Westphal, D. S. Bardenstein, and J. A. Izatt, "Real-Time Optical Coherence Tomography of the Anterior Segment at 1310 nm," Archives of Ophthalmology, **119**, (2001), pp. 1179-1185.
46. K. Bizheva, B. Povazay, B. Hermann, H. Sattmann, W. Drexler, M. Mei, R. Holzwarth, T. Hoelzenbein, V. Wacheck, and H. Pehamberger, "Compact, broad-bandwidth fiber laser for sub-2-mu m axial resolution optical coherence tomography in the 1300-nm wavelength region," Optics Letters **28**, 707-709 (2003).
47. M. A. Choma, K. Hsu, and J. A. Izatt, "Swept source optical coherence tomography using an all-fiber 1300-nm ring laser source," Journal of Biomedical Optics **10** (2005).
48. A. Unterhuber, B. Povazay, B. Hermann, H. Sattmann, A. Chavez-Pirson, and W. Drexler, "In vivo retinal optical coherence tomography at 1040 nm-enhanced penetration into the choroid," Optics Express **13**, 3252-3258 (2005).
49. B. Povazay, B. Hermann, A. Unterhuber, B. Hofer, H. Sattmann, F. Zeiler, J. E. Morgan, C. Falkner-Radler, C. Glittenberg, S. Blinder, and W. Drexler, "Three-dimensional optical coherence tomography at 1050 nm versus 800 nm in retinal pathologies: enhanced performance and choroidal penetration in cataract patients," Journal of Biomedical Optics **12** (2007).
50. G. M. Hale, and M. R. Querry, "Optical Constants of Water in the 200-nm to 200-µm Wavelength Region," Applied Optics **12**, 555-563 (1973).
51. T. L. Troy, and S. N. Thennadil, "Optical properties of human skin in the near infrared wavelength range of 1000 to 2200 nm.," Journal of Biomedical Optics **6**, 167-176 (2001).
52. A. Bashkatov, É. Genina, V. Kochubey, and V. Tuchin, "Optical properties of the subcutaneous adipose tissue in the spectral range 400–2500 nm," Optics and Spectroscopy **99**, 836-842 (2005).

53. W. F. Cheong, S. A. Prahl, and A. J. Welch, "A review of the optical properties of biological tissues," IEEE Journal of Quantum Electronics **26**, 2166-2185 (1990).
54. D. J. Maitland, J. J. T. Walsh, and J. B. Prystowsky, "Optical properties of human gallbladder tissue and bile," Applied Optics **32**, 586-591 (1993).
55. A. W. Sainter, T. A. King, and M. R. Dickinson, "Effect of target biological tissue and choice of light source on penetration depth and resolution in optical coherence tomography," Journal of Biomedical Optics **9**, 193-199 (2004).
56. L. Carrion, M. Lestrade, Z. Q. Xu, G. Touma, R. Maciejko, and M. Bertrand, "Comparative study of optical sources in the near infrared for optical coherence tomography applications," Journal of Biomedical Optics, **12** (2007) 014017.

CHAPTER 2

Wavelength-dependent NIR light penetration depth in Intralipid and biological tissues

The light penetration depth in biological tissues depends on the wavelength. We propose a method for the estimation of the light penetration depth in different biological tissues in the spectral range 1000-2000 nm. The scattering power parameter and the water content are used to characterize the optical properties of tissues. In particular, a comparison of the light penetration depth at 1300 nm and 1600 nm is performed. Light transmission measurements with different concentrations of Intralipid demonstrate good agreement with theoretical predictions. Calculations based on the published values of the optical properties of sclera, enamel, and dentin show that significant improvement in the light penetration depth can be achieved in enamel, moderate – in sclera, and no improvement is expected in dentin.

INTRODUCTION

Optical coherence tomography (OCT) has proven to be an important imaging modality in biomedical optics [1, 2]. OCT imaging performance is determined by the technical characteristics of the system (axial and lateral resolutions, sensitivity, imaging rate) and by the optical properties of the biological tissue under investigation (scattering and absorption coefficients, scattering anisotropy parameter).

One of the limitations of current OCT systems is the shallow imaging depth, which is in the range of 1-2 mm in scattering tissues. An increase of the imaging depth can improve the diagnostic potential of OCT. Since the optical properties of the tissue vary with wavelength [3], the imaging performance of OCT systems depends on the center wavelength of the light source that is used. Considering an OCT system with equivalent performance for different wavelengths (such as in Chapter 3), an optimal wavelength can be chosen to achieve the highest imaging depth for a particular tissue.

According to Mie theory, the general trend for the scattering coefficient is to decrease with increasing wavelength. As a result, the light penetration depth potentially can be increased by using longer wavelengths. Historically, after the introduction of OCT with 800 nm central wavelength, OCT at longer wavelengths was demonstrated and improvements in the imaging depth was shown [4, 5]. Current commercially available OCT systems operate in the spectral range of 800-1300 nm. Interest in using wavelengths longer than 1300 nm is growing, but the higher light absorption by water at these wavelengths raises questions about the feasibility of imaging depth improvements.

Knowledge of optical properties of different biological tissues does not cover all wavelengths, and especially for the NIR range not all optical properties are known. To compare the light penetration depth at different wavelengths, it is necessary to predict the optical properties for an extended spectral range. In this work, we propose a method that allows for a comparison of the light penetration depth in different biological tissues without direct measurements at these wavelengths. In particular, we compare the light penetration depth at 1300 nm and 1600 nm. The first wavelength is widely used in current OCT systems [6, 7], whereas the second wavelength is recognized as a potential wavelength for OCT imaging depth improvement [8].

THEORY

Light propagation inside turbid media is described by scattering and absorption. The probability of light to interact with the tissue per unit path length equals the attenuation coefficient μ_t, which is the sum of scattering and absorption coefficients: $\mu_t = \mu_s + \mu_a$. The reciprocal of μ_t is the mean free path length (e.g. the expectation value of the path length light

travels without interaction). The light penetration depth can (arbitrarily) be defined as equal to the mean free path: $D = 1/\mu_t$.

If multiple scattering effects are avoided, i.e. all light that is scattered is removed from the light beam and does not contribute to the measured transmitted intensity, then the light inside a turbid media is attenuated exponentially with depth. The intensity I of light at a certain depth *d* can be described by Lambert-Beer's law:

$$I = I_0 \exp(-\mu_t d) \tag{2-1}$$

where I_0 is the intensity of the incident light.

The main biological tissue chromophores responsible for the light absorption are melanin, hemoglobin, oxyhemoglobin, bilirubin and water. In the NIR spectral range (for wavelengths longer than 1000 nm) light absorption is dominated by the presence of water. The water content varies in biological tissues, but for most of them it is in the range of 70- 80%. Therefore, the volume fraction of water in tissue C is the parameter determining the absorption of NIR light and the absorption coefficient of biological tissues can be described as $\mu_a = C\mu_{a,water}$.

The scattering coefficient is wavelength dependent and in general tends to decrease for longer wavelengths. The wavelength dependency of the scattering coefficient μ_s can be approximated empirically in the form of a power law:

$$\mu_s \sim A\lambda^{-SP} \tag{2-2}$$

where A and SP are the model parameters for scattering amplitude and scattering power, respectively [9-11]. Parameter A is associated with the scattering strength: tissues with high scattering coefficient μ_s have high A parameter and vice versa. The value of SP is related to the average size of the scatterers: for particles with diameter d much smaller than the wavelength of light ($d<<\lambda$) the SP parameter is 4 (Rayleigh scattering regime, see Equation 1-10). With increasing particles size, the SP decreases (Mie scattering). The SP parameter determines how strong the scattering changes with wavelength, and thus if the SP parameter is high, then the variation in scattering with wavelength is stronger, and the possible gain in penetration depth is larger. Thus, the wavelength dependent light penetration depth D_λ in biological tissues is $D_\lambda = 1/(C\mu_{a\,water} + \mu_s)$. To quantify the enhancement or decrease of light penetration depth with wavelength, we calculate the ratio R of the light penetration depths at wavelengths λ_1 and λ_2 ($\lambda_1<\lambda_2$). Based on the empirical scattering power law with SP parameter, the scattering coefficient at λ_2 is described in terms of the scattering coefficient at λ_1, i.e.

$(\mu_s)_{\lambda_2} = (\lambda_1/\lambda_2)^{SP}(\mu_s)_{\lambda_1}$. Then, the ratio R of the light penetration depths D at λ_2 and λ_1 can be calculated:

$$R = \frac{D_{\lambda_2}}{D_{\lambda_1}} = \frac{(\mu_t)_{\lambda_1}}{(\mu_t)_{\lambda_2}} = \frac{(\mu_s)_{\lambda_1} + C(\mu_a)_{\lambda_1}}{(\lambda_1/\lambda_2)^{SP}(\mu_s)_{\lambda_1} + C(\mu_a)_{\lambda_2}} \quad (2\text{-}3)$$

For R>1 the use of λ_2 light results in a larger penetration depth. A quantitative analysis of both the absorption and scattering characteristics in terms of SP and μ_a shows how much we can gain or lose in light penetration depth using different wavelengths.

EXPERIMENTAL SETUP

To measure the optical properties of optical phantoms we perform light transmission measurements using the experimental setup depicted in Figure 2-1. Fiber coupled light from a supercontinuum light source (Fianium SC 450-4) is collimated (Fiber collimating package F230SMA-C, focal length 4.64 mm, Thorlabs) and directed to a 1 mm diameter diaphragm. A glass cuvette (1 mm optical pathlength) with scattering medium is placed directly behind diaphragm. The transmitted light is coupled to a monochromator (Oriel, Cornerstone 130 1/8 m, 0.12 mm slit size, 2 nm spectral resolution) for spectral measurements in the wavelength range of 1250 – 1650 nm. The distance between cuvette and input slit of the monochromator is 250 mm long to reduce the detection of multiple scattered light. A long-pass filter (Thorlabs, FEL0950) with a cut-on wavelength of 950 nm is implemented in front of the monochromator input slit to block the visible light. Light at the exit of the monochromator is detected by a photodetector (New Focus, model 2011) and the obtained signal is captured by a data acquisition card (National Instrument, USB-6009) and stored in a personal computer.

Figure 2-3. Layout of the experimental setup for light transmission measurements: *L*- collimator; *D*- diaphragm; *S* – cuvette with scattering sample; *MF* – multimode fiber; *F* – long-pass filter.

MEASUREMENTS WITH INTRALIPID

Measurements are conducted with Intralipid (Fresenius-Kabi) as a scattering medium. Intralipid is widely available fat emulsion, of which the scattering coefficient can be easily adjusted by water dilution. Intralipid is often used as a tissue simulating phantom in optical measurements [11].

By dilution of 22.7 vol.% stock solution with deionized water the following concentrations are prepared: 0.7, 1.4, 2.8, 5.7, 11.4 and 17 vol.%. The value of I_0 is measured on a cuvette filled with heavy water (which has negligible absorption in the spectral range of interest [12]), and I on the cuvette filled with Intralipid solution. Then, using Equation 2-1, the attenuation coefficient for each concentration is calculated using the thickness of the cuvette. Figure 2-2(a) shows the obtained attenuation coefficients. As can be seen, the attenuation coefficient decreases up to approximately 1360 nm, then starts to increase to a maximum at approximately 1460 nm, and, after the water peak, again decreases for longer wavelengths. To obtain the scattering coefficient μ_s , the absorption coefficient of water μ_a is subtracted from the total attenuation coefficient (Figure 2-2(b)) using the water volume fraction C obtained from the dilution and the known absorption coefficient of water [13]. The thus obtained scattering coefficient decreases monotonically with increasing wavelength. This clearly demonstrates that the peak in the attenuation in 1400-1500 nm spectral range is solely due to light absorption by water.

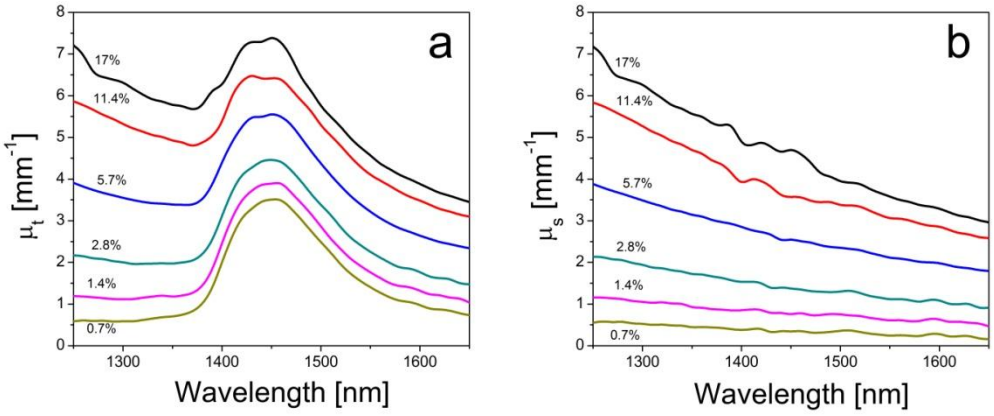

Figure 2-4. Experimentally determined attenuation (a) and scattering (b) coefficients as a function of wavelength for solutions with varying volume percentage of Intralipid (indicated).

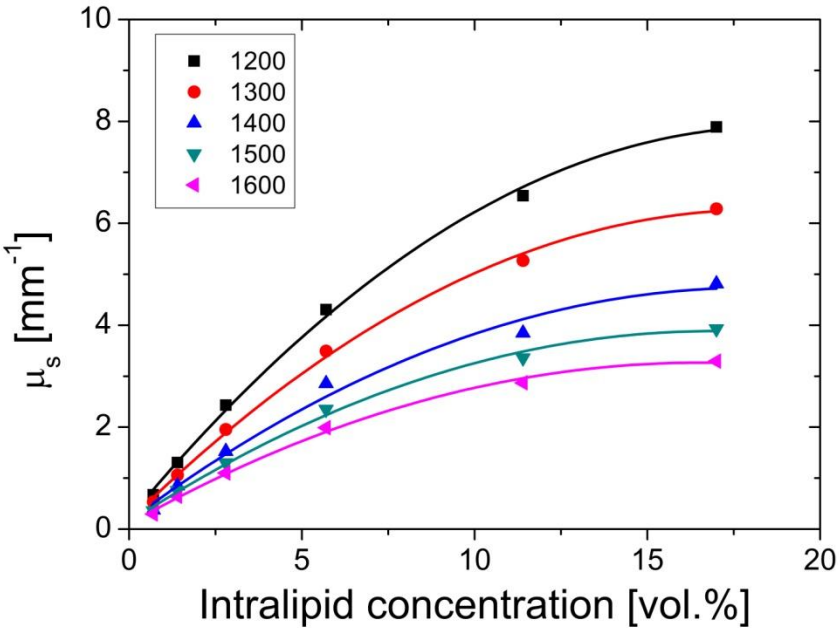

Figure 2-5. Measured (concentration dependent) scattering coefficient of Intralipid at wavelengths from 1200 to 1600 nm (solid symbols). Lines are a guide to the eye.

Figure 2-3 depicts, as a function of Intralipid concentration, the scattering coefficient of Intralipid at different wavelengths. As can be seen, up to 5.7 % IL the increase of μ_s is linear, which is expected for the independent and single scattering regime. However, for higher concentrations, the measured value of the scattering coefficient is lower than expected, with the same trend at different wavelengths. This saturation effect can be explained by the increased influence of multiple and dependent scattering effects on the measurements. To estimate the contribution of multiple scattering to our signal, we modeled our measurement geometry by calculating the total transmission of a slab of thickness d (corresponding to our cuvette thickness of 1 mm) using diffusion theory according to Star [14]. The calculation yields ballistic (T_{bal}) and diffuse (T_{diff}) contributions, the latter of which is integrated over the acceptance angle of the setup. We then estimate the measurement error as:

$$\varepsilon = \frac{\mu_{t,measured} - \mu_t}{\mu_t} = \frac{\frac{1}{d} Ln\left(T_{bal} + T_{diff} \frac{\theta_d^2}{4} \right) - \mu_t}{\mu_t} \qquad (2\text{-}4)$$

where θ_d is the setup acceptance angle of detection. T_{diff} is a function of the optical properties and cuvette thickness d. For values of μ_s = 15 mm^{-1}, μ_a = 0.1 mm^{-1}, g = 0.34, d = 1 mm, θ_d = 0.5/250, the error in the μ_t estimation is ≈ 1% due to detection of multiply scattered light. This suggests that the observed deviation from the expected linear increase of the scattering

coefficient with Intralipid concentration is mainly due to dependent scattering, which will be discussed in Chapter 7.

The scattering power parameter SP can be obtained by fitting the wavelength dependent changes of the scattering coefficient (Equation 2-2). Fitting of the data presented in Figure 2-2(b) resulted in SP values as shown in Figure 2-4. As can be seen, the SP is almost constant. The average value is SP = 3.0 ± 0.3 (which is higher than SP = 2.4 as reported by van Staveren [9]).

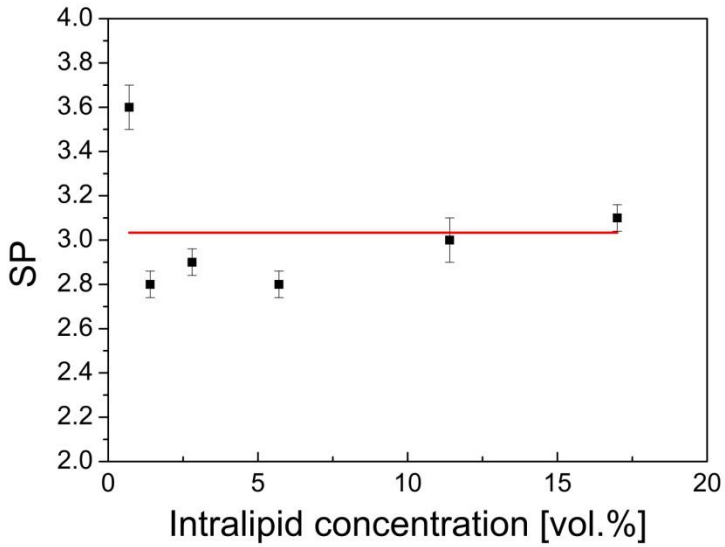

Figure 2-6. Experimental results of the SP parameter for varying Intralipid concentration (obtained from Fig. 2-3). The horizontal line indicates the average SP value.

Measurements of the attenuation coefficient (Figure 2-2(a)) shows that for wavelengths longer than 1500 nm the light attenuation decreases, which suggests that improvement in light penetration depth can be achieved for this wavelength range. To quantify this we calculate the ratio R of light penetration depths at wavelengths 1300 nm and 1600 nm for each Intralipid concentration based on our experimental results. Then, to compare experimental results with theoretical calculations, the ratio of the light penetration depths R at 1600 nm to 1300 nm is calculated using Equation 2-3 with a scattering power parameter SP of 3.0 and the known optical absorption of water (light absorption coefficient by water is 0.11 mm^{-1} at 1300 nm and 0.67 mm^{-1} at 1600 nm). Figure 2-5 shows the obtained results and, as can be seen, the experimental results closely correspond to the theoretical calculations.

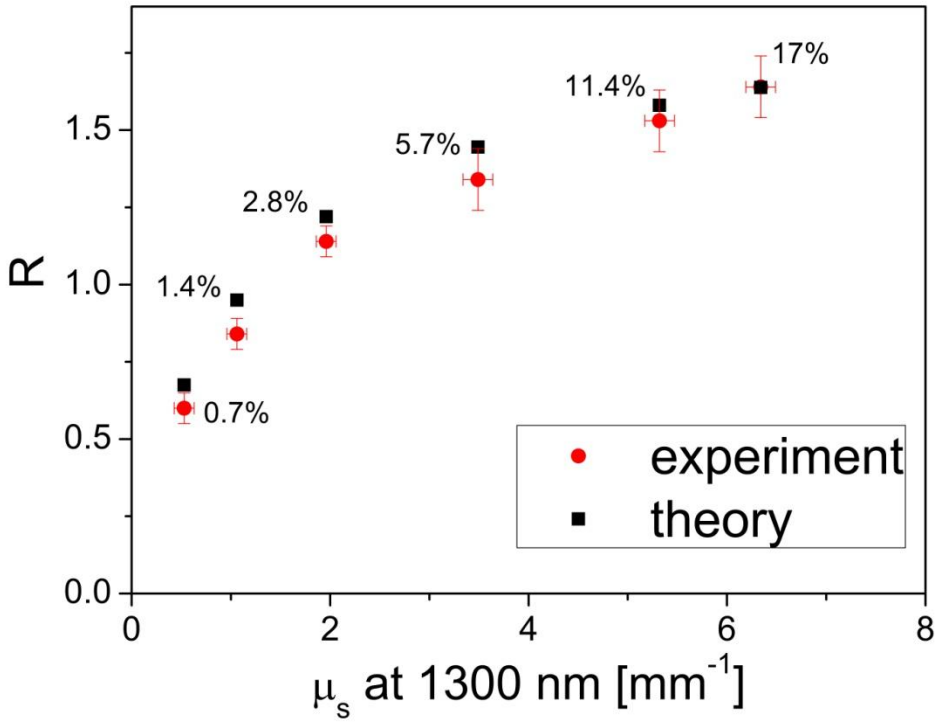

Figure 2-7. Light penetration depth ratio *R* at 1600 nm to 1300 nm for different concentrations of Intralipid; Experimental results (symbols) and theoretical calculations (solid line). The theoretical points are calculated using the known water content for each IL concentration and *SP* = 3.0.

APPLICATION TO BIOLOGICAL TISSUES

Our measurements with Intralipid demonstrate that the calculations based on the scattering power parameter SP and known water content C give a good approximation for the comparison of the light penetration depths at different NIR wavelengths. This method can be extended to biological tissues using the published values of their optical properties. An advantage of our method is that comparisons can be performed for biological tissues at wavelengths where the optical properties are not reported, i.e. without direct measurements at these wavelengths.

We performed light penetration calculations for rabbit eye sclera, human enamel and dentin (Table 2-1) as these tissues represent key application areas for OCT and are tissues with very different optical properties in terms of absorption and scattering. Sclera is a tissue with a high scattering coefficient, high *SP* and water content of 70%; enamel has a low scattering coefficient, high SP and almost no water; dentin is a tissue with a high scattering coefficient, low SP and low water content.

Table 2-1. Optical properties of biological tissues analyzed in this article. Grey cells are calculated values.

Tissue	Volume fraction of water	λ, nm	μ_s at λ , mm^{-1}	SP	R	Ref.
Rabbit eye sclera	0.70	500	86.0 ± 29.0	2.3±0.2	1.5±0.1	[15]
		550	75.5 ± 25.2			
		700	50.4 ± 15.4			
		850	29.8 ± 7.5			
		1050	16.3 ± 3.2			
Enamel	0.01	543	10.5 ± 3	2.9±0.2	1.8±0.1	[16]
		632	6.0 ± 1.8			
		1053	1.5 ± 0.5			
Dentin	0.15	543	28.0 ± 8.4	0.12±0.03	1.02±0.01	[16]
		632	28.0 ± 8.4			
		1053	26.0 ± 7.8			

First, the SP parameter is calculated based on the reported values of the scattering coefficient. The value of μ_s is fitted using Equation 2-2 with SP and A as a fitting parameter. Then, using Equation 2-3, we calculated the wavelength dependent changes in the light penetration depth ratio R for enamel, dentin and sclera in the spectral range 1050 – 2000 nm, with the ratios calculated relative to the light penetration depth at 1050 nm (i.e. at 1050 nm R=1 for all tissues). Figure 2-6 shows that there is no significant change in the light penetration depth for dentin, which can be explained by the low SP parameter and low water content. Scattering changes slowly with increasing wavelength and the influence of the absorption by water is insignificant. In the case of the sclera, the light penetration depth is increasing up to 1850 nm, and then starts to decrease due to increasing optical absorption by water. It is interesting to note, that the increase is almost monotonic, and, despite of the high water content, the influence of the absorption by water at 1400-1500 nm is low. This monotonic behavior can be explained by the fact that sclera has a high scattering coefficient and high scattering power parameter SP, which means that the scattering is the dominating process

determining the light attenuation in the sclera. Finally, for enamel the light penetration depth is monotonically increasing for longer wavelengths, which is the result of a high SP parameter and very low water content.

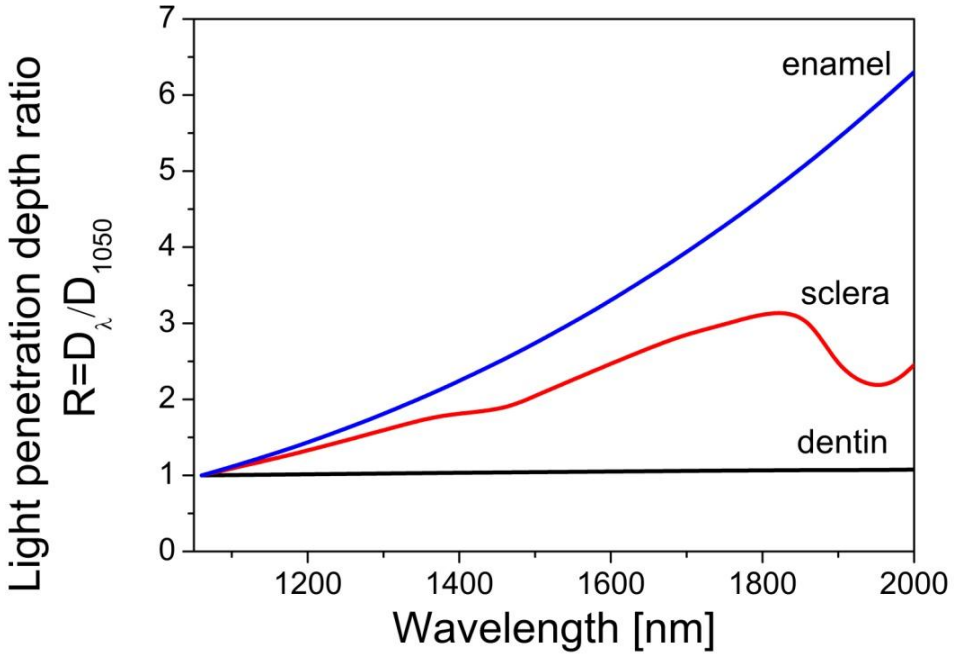

Figure 2-8. Theoretical calculations of changes in the light penetration depth for enamel, dentin and sclera, based on the water contents and scattering powers given in table 2-1.

To compare differences in light penetration depths at 1300 nm and at 1600 nm, the ratio $R = D_{1600}/D_{1300}$ is calculated (Equation 2-3). For dentin R is 1, for rabbit eye sclera R is 1.5, and for enamel it is highest: R is 1.8. These results demonstrate that the light penetration depth D with 1600 nm light can be higher in sclera and enamel, but not for dentin. If we compare R values, we can note that the increase in R mainly corresponds to the increase in SP, i.e. for higher SP the value of R is also higher. As an example, for enamel with low scattering coefficient and no water content, but high SP = 2.9, the R is highest. In contrast, for dentin with low SP = 0.12 and low water content, the R is 1.

It is important to note that for real OCT systems with broadband light sources the weighted attenuation coefficient for spectrum of the light source should be used. Furthermore, the wavelength dependent backscattering properties of the scatterers should be taken into account, which is the topic of Chapter 3.

CONCLUSIONS

In conclusion, we demonstrated a method for predicting of the wavelength dependent changes in the light penetration depth in biological tissues. Using this method, we compared the light penetration depth at 1300 nm and at 1600 nm in Intralipid (based on the light transmission measurements) and in some biological tissue (based on the published optical properties). Our results show that improved light penetration depth at 1600 nm can be achieved for the biological tissues with high SP parameter, high scattering coefficient, and low water content. This information is important for predicting the imaging depth for OCT systems operating at different wavelengths and imaging different tissue types.

REFERENCES

1. D. Huang, E. A. Swanson, C. P. Lin, J. S. Schuman, W. G. Stinson, W. Chang, M. R. Hee, T. Flotte, K. Gregory, C. A. Puliafito, and J. G. Fujimoto, "Optical Coherence Tomography," Science **254**, 1178-1181 (1991).
2. A. M. Zysk, F. T. Nguyen, A. L. Oldenburg, D. L. Marks, and S. A. Boppart, "Optical coherence tomography: a review of clinical development from bench to bedside," Journal of Biomedical Optics **12** (2007).
3. W. F. Cheong, S. A. Prahl, and A. J. Welch, "A review of the optical properties of biological tissues," IEEE Journal of Quantum Electronics **26**, 2166-2185 (1990).
4. A. Unterhuber, B. Povazay, B. Hermann, H. Sattmann, A. Chavez-Pirson, and W. Drexler, "In vivo retinal optical coherence tomography at 1040 nm-enhanced penetration into the choroid," Optics Express **13**, 3252-3258 (2005).
5. B. Povazay, B. Hermann, A. Unterhuber, B. Hofer, H. Sattmann, F. Zeiler, J. E. Morgan, C. Falkner-Radler, C. Glittenberg, S. Blinder, and W. Drexler, "Three-dimensional optical coherence tomography at 1050 nm versus 800 nm in retinal pathologies: enhanced performance and choroidal penetration in cataract patients," Journal of Biomedical Optics **12** (2007).
6. M. A. Choma, K. Hsu, and J. A. Izatt, "Swept source optical coherence tomography using an all-fiber 1300-nm ring laser source," Journal of Biomedical Optics **10** (2005).
7. K. Bizheva, B. Povazay, B. Hermann, H. Sattmann, W. Drexler, M. Mei, R. Holzwarth, T. Hoelzenbein, V. Wacheck, and H. Pehamberger, "Compact, broad-bandwidth fiber laser for sub-2-mu m axial resolution optical coherence tomography in the 1300-nm wavelength region," Optics Letters **28**, 707-709 (2003).
8. U. Sharma, E. W. Chang, and S. H. Yun, "Long-wavelength optical coherence tomography at 1.7 ?m for enhanced imaging depth," Opt. Express **16**, 19712-19723 (2008).
9. H. J. van Staveren, C. J. M. Moes, J. van Marie, S. A. Prahl, and M. J. C. van Gemert, "Light scattering in Intralipid-10% in the wavelength range of 400-1100 nm," Applied Optics **30**, 4507-4514 (1991).
10. J. R. Mourant, T. Fuselier, J. Boyer, T. M. Johnson, and I. J. Bigio, "Predictions and measurements of scattering and absorption over broad wavelength ranges in tissue phantoms," Applied Optics **36**, 949-957 (1997).
11. B. W. Pogue, and M. S. Patterson, "Review of tissue simulating phantoms for optical spectroscopy, imaging and dosimetry," Journal of Biomedical Optics **11**, 041102-041116 (2006).
12. J. M. Schmitt, S. H. Xiang, and K. M. Yung, "Differential absorption imaging with optical coherence tomography," Journal of the Optical Society of America A-Optics Image Science and Vision **15**, 2288-2296 (1998).
13. G. M. Hale, and M. R. Querry, "Optical Constants of Water in the 200-nm to 200-µm Wavelength Region," Applied Optics **12**, 555-563 (1973).
14. A.J. Welch, M.J.C. van Gemert, *Optical-Thermal Response of Laser-Irradiated Tissue,* Chapter 6 (Springer, second edition).
15. B. Nemati, H. G. Rylander, and A. J. Welch, "Optical properties of conjunctiva, sclera, and the ciliary body and their consequences for transscleral cyclophotocoagulation," Applied Optics **35**, 3321-3327 (1996).
16. D. Fried, R. E. Glena, J. D. B. Featherstone, and W. Seka, "Nature of light scattering in dental enamel and dentin at visible and near-infrared wavelengths," Applied Optics **34**, 1278-1285 (1995).

CHAPTER 3

Quantitative comparison of the OCT imaging depth at 1300 nm and 1600 nm

Published in: *Biomedical Optics Express*, Vol. 1, Issue 1, pp. 176-185 (2010)

One of the present challenges in optical coherence tomography (OCT) is the visualization of deeper structural morphology in biological tissues. Owing to a reduced scattering coefficient, a larger imaging depth can possibly be achieved by using longer wavelengths. In this work, we analyze the OCT imaging depth at wavelengths around 1300 nm and 1600 nm by comparing the scattering coefficient and OCT imaging depth for a range of Intralipid concentrations at constant water content. We observe an enhanced OCT imaging depth for 1600 nm compared to 1300 nm for Intralipid concentrations larger than 4 vol.%. For higher Intralipid concentrations, the imaging depth enhancement reaches 30 %. The ratio of scattering coefficients at the two wavelengths is constant over a large range of scattering coefficients and corresponds to a scattering power of 2.8 ± 0.1. Based on our results we expect for biological tissues an increase of the OCT imaging depth at 1600 nm compared to 1300 nm for samples with high scattering power and low water content.

1. INTRODUCTION

Optical coherence tomography (OCT) is a high resolution, non-invasive, coherence-gated imaging technique with a wide range of applications in medicine [1-5]. One of the present challenges in OCT is the visualization of deeper structural morphology in biological tissues, which can improve existing and create new applications. For current OCT systems the imaging depth is approximately 1–2 mm. The large scattering coefficient of biological tissues limits the amount of light that can be collected from structures located deep in the tissue. Since the optical properties of biological tissues vary significantly with wavelength, the imaging depth can be improved by using a light source with an optimal imaging wavelength.

The general trend for the scattering coefficient is to decrease with increasing wavelength. Therefore, a longer wavelength is potentially more advantageous for deeper imaging. The first OCT system operated in the 800 nm spectral range. The longer wavelength OCT systems, operating in the 1300 and 1050 nm spectral bands, were introduced soon after and an improved imaging depth was demonstrated [6-10]. However, the use of longer wavelengths for imaging depth improvement is restricted by the increased optical absorption of water [11]. Nevertheless, the spectral window from 1600 to 1800 nm, between two primary water absorption bands (1400 to 1500 nm and 1900 to 2200 nm), is recognized as a promising choice to further increase the OCT imaging depth. OCT in this part of the spectrum was demonstrated [12-14], and a direct comparison of OCT systems operating at 810, 1330, and 1570 nm was presented [15]. Also, a comparison of light penetration depth for different OCT light sources in skin dermis, liver, and gallbladder was reported [16]. Although these studies have shown that the use of longer wavelengths enables an enhanced imaging depth for certain types of biological tissues, the advantage of using the 1600 – 1800 nm spectral band remains to be quantified. Since the different OCT wavelengths were compared based on images that were obtained with different OCT setups, the measured imaging depth depended not only on tissue properties, but also on the technical characteristics of the used OCT systems.

In this study, we perform a quantitative comparison of the OCT imaging depth at 1300 nm and 1600 nm wavelengths using a single time-domain OCT set-up of which the technical performance at the two wavelengths is matched. Using Intralipid with a constant absorption coefficient as tissue phantom material, we determine the influence of the scattering on the OCT imaging depth.

2. MATERIALS AND METHODS

2.1 Time-domain optical coherence tomography

The OCT experiments are conducted with a home-built time-domain OCT system. A schematic of the set-up is depicted in Figure 3-1(a). Light from a supercontinuum light source (Fianium SC 450-4) is coupled into a single-mode fiber (1550 BHP, Thorlabs) and collimated (FiberPort system, PAF-X-18-PC-C, focal length 18.4 mm, Thorlabs) at the input of a 50/50 Michelson interferometer. In the sample and reference arms, identical achromatic lenses with focal length 45 mm are used to focus the light on the sample and reference mirrors, respectively. Depth scanning is performed by moving the reference arm mirror (at a velocity V=20 mm/sec), which is mounted together with the lens on a translator (Physik Instrumente M 664.164). In the sample arm, the beam is focused at the front glass-Intralipid interface of the 1 mm thick cuvette. We have fixed focus configuration, i.e the focus position doesn't change during an A-scan. The angle between the probe beam and the cuvette is ~ 70° to avoid specularly reflected light in the signal. Light returning from reference and sample arms is combined and coupled into a single-mode fiber. The interferometric signal is detected with a photodiode (New focus, model 2011), band-pass filtered and demodulated by a lock-in

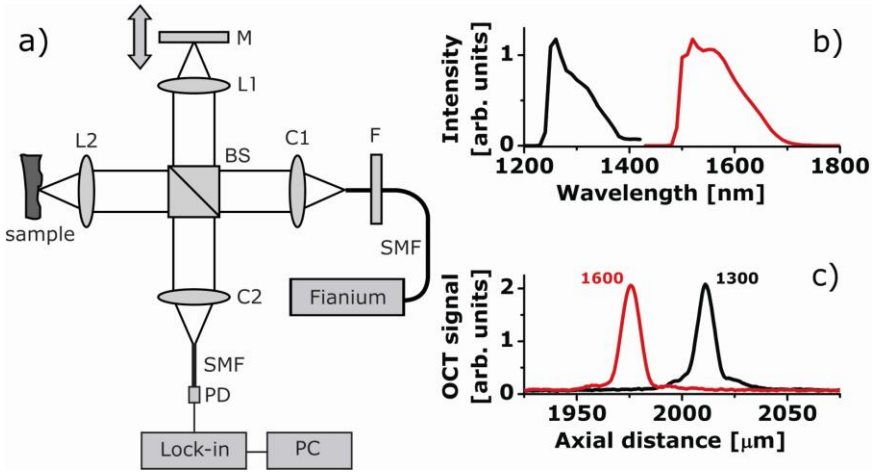

Figure 3-9. a) Overview of the time domain OCT set-up used in the experiments: BS – beamsplitter; C1,C2 - fiber collimating ports; L1, L2 - reference and sample arm lenses; M - reference mirror; SMF - single mode fibers; F - long pass filter; PD - photodetector; Lock-in – Lock-in amplifier; PC - personal computer; Fianium – supercontinuum light source; b) OCT input spectra for the two wavelength bands; c) coherence function at the two OCT wavelengths (measured with an OD3 filter in sample arm).

amplifier set to the Doppler frequency $f = 2V/\lambda_0$. To reduce noise, the signal is averaged over 100 A-scans. The sample is not scanned in the lateral direction. The central wavelength λ_0 and the bandwidth of the light coupled into the interferometer is changed between 1300 and 1600 nm bands using long pass filters (Thorlabs, FEL1250 and FEL1500, respectively) and by adjusting the bandwidth of the light coupled to the fiber using the effect of chromatic aberrations (Figure 3-1(a)).

2.2 Performance matched OCT at 1300 nm and 1600 nm

The OCT detector current signal $i_d(z)$ as a function of depth z is proportional to the square root of the power backscattered from depth z. In the single backscattering approximation and with a coherence length l_c less than the photon mean free path $1/\mu_t$ [17], with μ_t the attenuation coefficient, $i_d(z) \sim P(z)^{1/2} = [P_0 \, K \, \mu_b \, h(z) \, exp(-2\mu_t z)]^{1/2}$ where P_0 is the incident power on the sample; the parameter K is proportional to the coherence length l_c; μ_b is the backscattering coefficient and $h(z)$ is the confocal point spread function (PSF). In the following, we assume either dynamic focusing, or that the data is corrected for the point spread function [18]. The factor of 2 in the exponent accounts for the round-trip attenuation to and from the depth z; the square root accounts for the fact that the OCT signal magnitude is proportional to the amplitude of the field returning from the sample, rather than power.

The OCT signal-to-noise ratio is defined as $SNR = 10log_{10}(P_s/P_{noise})$, where P_s is the power returning from the sample arm with mirror, and P_{noise} is the noise power. We define the imaging depth Z_{image} as the depth at which $P(z) = P_{noise}$, or:

$$Z_{image} = \frac{1}{2\mu_t}[Ln(K\mu_b) + \frac{SNR}{10} Ln(10)] \quad (3\text{-}1)$$

Equation 3-1 shows that the OCT imaging depth is determined by the optical properties of the sample as well as by the characteristics of the OCT setup itself. For a quantitative comparison of the imaging depth at different center wavelengths only in terms of the optical properties of the sample, it is important to take into account the system characteristics at the two wavelengths.

Firstly, the spectral bandwidth of the light coupled into the interferometer (Figure 3-1(b)) is adjusted to reach equal coherence lengths of l_c = 10 µm at both OCT wavelengths (Figure 3-1(c)).

Secondly, the effect of the confocal point spread function on the OCT signal at the two imaging wavelengths is taken into account following the procedure outlined in our previous work [18]. In brief, the change of the OCT signal as a function of distance between the probed location z in the tissue and the focus position z_0 is corrected using the axial PSF, which, in the case of diffuse reflection, has the form: $h(z)=1/\{[(z-z_0)/(2nZ_R)]^2+1\}$, where Z_R is the Rayleigh

length in air and n is the refractive index of the medium. The measured Rayleigh lengths (half the depth of focus) are 0.29 and 0.25 mm at 1300 and 1600 nm, respectively. Due to the achromaticity of the lens, the focus position is different for the two wavelength bands. The positions of the sample arm and reference arm lens are shifted 500 µm when changing from 1300 nm to 1600 nm to compensate for this.

Thirdly, the SNR for a shot-noise limited time-domain OCT system is calculated from the mean square detector current $<i_d^2>$ and the noise variance σ_n^2 as:

$$SNR = 10Log_{10}\frac{\left\langle i_d^{\,2}\right\rangle}{\sigma_n^{\,2}} = 10Log_{10}\left(\frac{\eta P_s}{E_v \Delta f}\right) \tag{3-2}$$

where η is the quantum efficiency of the detector, P_s is the power returning from the sample arm; E_v is the photon energy and Δf is the electronic detection bandwidth. The ratio P_s/E_v in Equation 3-2 equals the number of photons returning from the sample arm per second. Therefore, the input power is adjusted to obtain an equal amount of photons detected from the sample arm with a mirror positioned at the focus The resulting input powers are 4.5 mW and 6.4 mW for 1300 nm and 1600 nm, respectively, and the power of the light coupled to the detector from the sample arm are 0.33 mW and 0.27 mW, respectively (the optical components have different efficiencies at 1300 and 1600 nm). Since the photon energy at 1300 nm is higher than at 1600 nm, the number of detected photons returning from the sample arm is equal for both OCT wavelengths. Because the quantum efficiency of the photodetector is equal at the two OCT wavelengths, the same signal is measured for the two OCT wavelengths. Although our OCT system is not entirely shot-noise limited, the use of the same light source and photodetector ensures that the noise at both wavelengths is matched and an equal SNR is achieved.

Finally, the reference arm power is adjusted using a neutral density filter to optimize the SNR. The lock-in amplifier demodulation frequencies f are 30.5 and 25 kHz for 1300 and 1600 nm, respectively, but the detection bandwidth Δf is equal. As a result of the procedure outlined here, the SNR for an OCT measurement with a mirror in the sample arm is equal at the two OCT wavelengths, which we measured to be 90 dB at 1300 and 1600 nm (see Figure 3-1(c)).

2.3 Phantom preparation

As a scattering medium we use dilutions of a single batch of 22.7 vol.% (20 weight %) Intralipid (Fresenius-Kabi). Our choice is determined by the fact that Intralipid is a common tissue phantom for optical measurements and it allows us to achieve a high concentration of scatterers. For our measurements Intralipid is diluted to lower concentrations by a mixture of deionized water and heavy water (D_2O). Heavy water has an absorption spectrum similar to

water, but the absorption bands are shifted to longer wavelengths [19]. Consequently, heavy water has negligible absorption for wavelengths lower than 1700 nm, which we experimentally verified. The refractive index of D_2O is only slightly different from that of normal water [20], therefore we assume that dilution by heavy water has no significant influence on the scattering properties of Intralipid. The ratio of heavy water and water is such that for all samples the total water concentration (77 vol.%) and, consequently, the absorption is constant, and only the scattering properties vary. We prepared the following samples: 0.7, 1.4, 2.8, 5.7, 8.5, 11.4, 14.2, 17.0, 19.9 and 22.7 volume % Intralipid.

2.4 Determination of optical parameters and imaging depth

OCT measurements at each Intralipid concentration are performed 3 times. For each measurement, 100 A-scans are averaged. Noise background and noise standard deviation are determined from the part of the OCT signal within the first glass wall. After background subtraction, the OCT signal is corrected for the confocal point spread function (dividing the OCT signal by the PSF) [18]. The OCT attenuation coefficient is determined from a single exponential fit of the corrected OCT signal in depth: $i_d(z) = a\ exp(-\mu_t z)$ with a and μ_t the two free running parameters. The influence of multiple scattering effects is minimized by using only the first 190 µm of the OCT signal for fitting. The OCT imaging depth is calculated from the fit by extending the fitted curve to the point where it intercepts the noise floor (defined as the noise mean plus one standard deviation).

The scattering coefficient of our samples is determined from the measured attenuation coefficient by subtracting the water absorption coefficient from the fitted attenuation coefficient. The variation of the absorption coefficient over the wavelengths of the input spectra is taken into account by calculating the water absorption integrated over the input spectra. We obtain μ_a = 0.2 mm^{-1} and μ_a = 1.1 mm^{-1} for 1300 nm and 1600 nm spectra, respectively. Finally, the standard deviation is calculated from the three subsequent measurements.

3. RESULTS

3.1 OCT signal attenuation

Figure 3-2 shows averaged OCT A-scans at three different Intralipid concentrations. The OCT signal magnitude at the first glass/Intralipid interface increases with concentration as is expected from the increasing backscattering with increasing particle concentration. The signal magnitudes for 1300 and 1600 nm are approximately equal, which shows that the backscattering coefficient is similar for both cases (the same amount of photons is detected). For the 0.7 vol.% Intralipid concentration, the OCT signal attenuation with depth is lower at

1300 nm compared to 1600 nm; for the 8.5 vol.% and 22.7 vol.% concentrations the attenuation coefficient is higher at 1300 nm compared to 1600 nm.

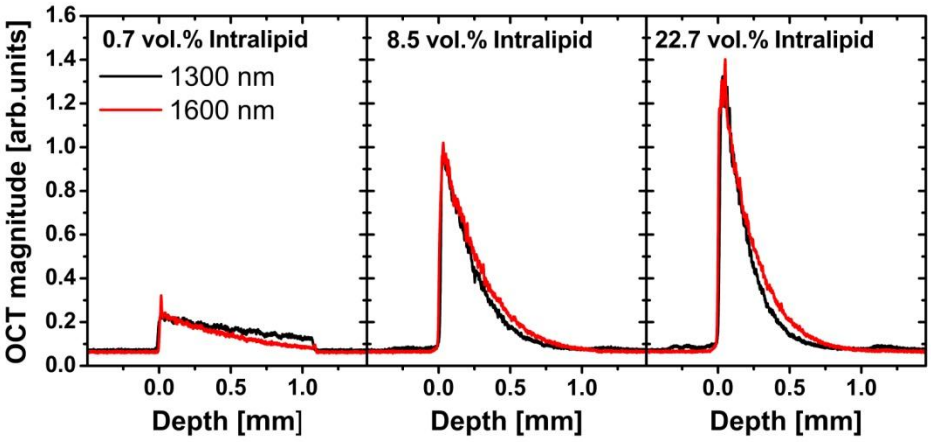

Figure 3-10. OCT signals vs. depth for 0.7%, 8.5% and 22.7 vol.% Intralipid samples for the two wavelengths (data before background subtraction and PSF correction).

Figure 3-3 shows the measured attenuation and resulting scattering coefficient for all Intralipid concentrations. For low Intralipid concentrations the attenuation coefficient is higher at 1600 nm compared to 1300 nm. At Intralipid concentrations larger than ~ 4 vol.% the attenuation coefficient at 1300 nm exceeds that of 1600 nm. As expected, the scattering coefficient is higher at 1300 nm for all measured Intralipid concentrations. Note that variation of the scattering coefficient with Intralipid concentration shows a clear deviation from the linear dependence expected for low-density media: for high Intralipid concentrations we see a non-linear dependence of the scattering coefficient, which is attributed to multiple scattering and/or concentration dependent scattering [21-23].

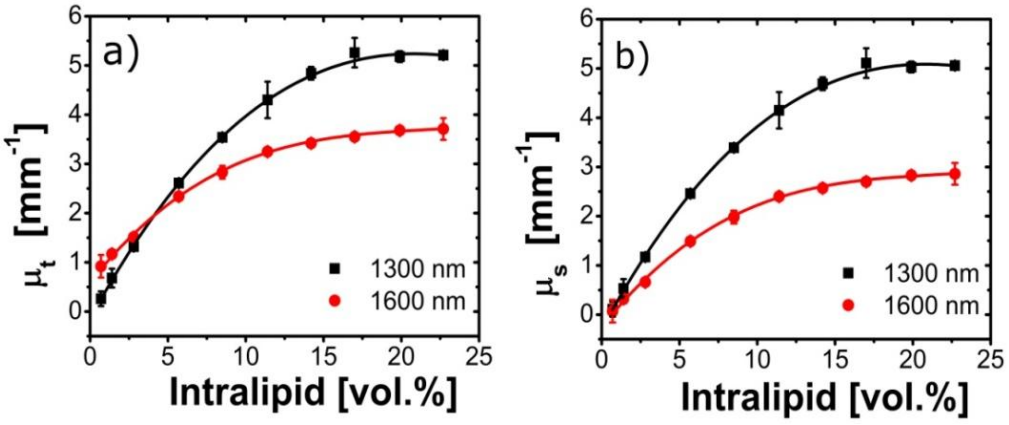

Figure 3-11. Measured OCT attenuation (a) and scattering (b) coefficients versus Intralipid concentration. The solid lines are visual guides. Error bars depict standard deviations of the measurements.

3.2 OCT imaging depth comparison

Figure 3-4 shows the OCT imaging depth for the two OCT wavelengths. At 1300 nm, the imaging depth is larger for low Intralipid concentrations. For example, for the lowest Intralipid concentration (0.7 vol.%) the imaging depth is approximately 3 mm larger for 1300 nm compared to 1600 nm. For 4 vol.% Intralipid the imaging depth at 1600 nm is equal to that at 1300 nm. For higher Intralipid concentrations the imaging depth at 1600 nm is larger. At the maximum Intralipid concentration (22.7 vol.%) the OCT imaging depth is 30% larger for 1600 nm compared to 1300 nm (0.8 mm vs 0.6 mm, respectively). In the limit of high Intralipid concentrations the effect of the water absorption on the total attenuation is small at both wavelengths. Consequently, the imaging depth is dominated by the difference in scattering at the two OCT wavelengths.

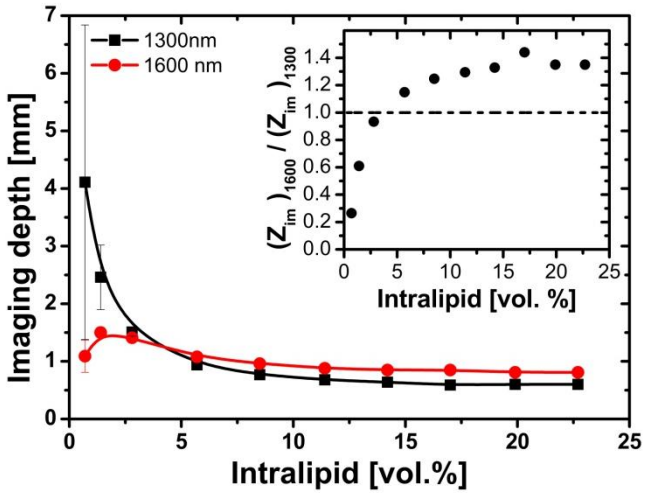

Figure 3-12. OCT imaging depth for varying Intralipid concentration measured at 1300 and 1600 nm. The solid lines are visual guides. Error bars depict standard deviations of the measurements. Inset: ratio of measured OCT imaging depths. The dashed line indicates equal imaging depth at 1300 and 1600 nm.

The inset of Figure 3-4 shows the ratio of the OCT imaging depth at 1600 nm to that at 1300 nm. For high Intralipid concentrations the imaging depth is dominated by scattering, the ratio of imaging depths is larger than unity. In this limit the 1600 nm OCT wavelength has an approximately 30 % larger imaging depth. For low Intralipid concentration, the OCT imaging depth is dominated by absorption, the ratio of imaging depths is smaller than unity and 1300 nm has a larger imaging depth.

It is also interesting to note the dissimilarity of the dependence of the imaging depth at 1300 and 1600 nm on the Intralipid concentration. At 1300 nm it monotonically increases with decreasing Intralipid concentration. The imaging depth at 1600 nm has the same trend, except for low concentrations, where it starts to decrease. This difference can be explained by the

stronger contribution of water absorption to the total attenuation coefficient at 1600 nm compared to 1300 nm: for very low Intralipid concentrations the scattering coefficient decreases, resulting in a decreasing backscattering, which lowers the OCT signal amplitude and the remaining high absorption lead to decrease of imaging depth. A similar effect is expected at 1300 nm, but only for very low Intralipid concentrations, not within our measurement range.

4. DISCUSSION

Since the technical characteristics of the OCT setups at 1300 and 1600 nm imaging wavelengths are matched, only the optical properties of the sample determine the difference in the measured OCT imaging depth. In the determination of the OCT imaging depth, two sample parameters are of importance: the backscatter coefficient μ_b, which determines the initial magnitude of the OCT signal, and the attenuation coefficient μ_t, which determines how fast the OCT signal decays with depth to the noise floor.

The backscatter coefficient μ_b is formally defined as the (total) scattering coefficient of an isotropically scattering particle with a phase function $p_{ISO}(\theta)=p(180)$ where $p(180)$ is the phase function of the original scatterer in the backward direction. This leads to $\mu_b = 4\pi\mu_s p(180)$. In the OCT geometry the following interpretation of μ_b is more appropriate: $\mu_b = \mu_s \int_{NA} p(\theta) 2\pi \sin\theta d\theta$, e.g. the phase function integrated over the numerical aperture (NA) of the OCT sample arm lens in the backscatter direction. From Equation 3-1, the magnitude of the OCT signal immediately after the front glass-Intralipid boundary (z = 0) is therefore proportional to the square root of the scattering coefficient μ_s. Figure 3-2 shows that the OCT magnitude increases with Intralipid concentration, consistent with the observed increase in the scattering coefficient. In addition, the magnitudes of the OCT signal at 1300 and 1600 nm for the same Intralipid concentration are similar. This suggests that the difference in backscattering coefficient at these wavelengths is small. Since μ_s is larger at 1300 nm compared to 1600 nm (Figure 3-3(b)), we conclude that the Intralipid scattering phase function in the backscattering direction (180°) within the detection NA is higher at 1600 nm compared to 1300 nm. This observation is consistent with a reduced size parameter at 1600 nm compared to 1300 nm making the phase function more isotropic at 1600 nm compared to 1300 nm.

Our measurements are performed on samples with constant H_2O content. The reported scattering coefficients are calculated by subtracting a constant absorption from the measured attenuation coefficients (Figure 3-3(a)). Using this method we obtain a μ_s that approaches zero when no scattering is present (zero Intralipid concentration; see Figure 3-3(b)). In addition, the value of the scattering coefficient μ_s at 1300 nm is in good agreement to those found in Ref. [23]. For all Intralipid concentrations the scattering at 1600 nm is lower compared to 1300 nm. However, since the absorption is higher at 1600 nm, the OCT imaging depth is enhanced compared to 1300 nm only for Intralipid concentrations above 4 vol.%. For Intralipid

concentrations lower than 4 vol.% the lower scattering coefficient at 1600 nm is compensated by the higher absorption, resulting in an increased imaging depth for 1300 nm. In the limit of very high Intralipid concentrations the H_2O absorption coefficient can be neglected and the difference between the scattering coefficients at the two wavelengths saturates at $\Delta\mu_s \sim 2.1$ mm^{-1}. Consequently, the OCT imaging depth enhancement also reaches a plateau at a difference of 200 µm, i.e. 30 % higher for 1600 nm compared to 1300 nm.

Recent work on the comparison of the performance of OCT systems with light sources centered at 1300 and 1650 nm [14] showed that the ratio of the attenuation coefficients for 10 wt.% Intralipid at 1300 nm to 1650 nm is 1.24. This value is close to our result for this Intralipid concentration, which is 1.29 (with a minor difference in water absorption and central wavelength). However, because of the differences in setup characteristics and the fact that in the published work the attenuation coefficient was calculated without correction for the refractive index of Intralipid, it is difficult to compare our imaging depth measurements with these published results.

It is interesting to compare the scattering coefficient of Intralipid at 1300 and 1600 nm. For a polydisperse solution of particles, like Intralipid, and the absence of strong absorption, the wavelength dependency of the scattering coefficient is described empirically in the form of a power law: $\mu_s \sim A(\lambda)^{-SP}$, where A and SP are the parameters for scattering amplitude and scattering power, respectively [24]. The parameter A is associated with the magnitude of the scattering, but does not depend on wavelength: tissues with high scattering coefficient μ_s have high A parameter and vice versa. The SP parameter determines how strong the scattering changes with wavelength. The value of SP is related to the average size of the scatterers: for particles with diameter d much smaller than wavelength of light ($d<<\lambda$) the parameter SP approaches 4 (Rayleigh scattering regime). With increasing particles size, the SP decreases (Mie scattering). From this simple model, changes in the scattering coefficient with wavelength ($\lambda_1<\lambda_2$) can be described as follows:

$$(\mu_s)_{\lambda_2} = \left(\frac{\lambda_1}{\lambda_2}\right)^{SP} (\mu_s)_{\lambda_1} \qquad (3\text{-}3)$$

Figure 3-5 shows the measured scattering coefficient at 1600 nm versus that at 1300 nm for all Intralipid concentrations. From a linear fit to the data points using Equation 3-3 we find SP = 2.8 ± 0.1, which is close to a previously reported value of SP for Intralipid SP = 2.4 [24, 25]. In addition, Figure 3-5 shows that the relative difference in the scattering coefficient at 1300 to 1600 nm remains approximately constant for all Intralipid concentrations. We can conclude that concentration dependent scattering effects are similar for the two wavelengths.

Since the SP parameter describes the wavelength dependence of the scattering coefficient, this parameter can be used to predict changes in the OCT imaging depth with wavelength for biological tissues. From Equation 3-3 follows that for samples with a low SP the variation in scattering with wavelength is small. In this case, the increase of the OCT imaging depth with increasing wavelength is expected to be small. For samples with a high SP the scattering coefficient shows a strong variation with wavelength and a relatively large increase of the OCT imaging depth can be expected. Additionally, for samples with significant water content, the higher water absorption in the 1600 – 1800 nm spectral band is a counteracting factor. Therefore, we expect an increase of the OCT imaging depth for samples with high SP and low water content (e.g. enamel) and we do not expect an increase of the OCT imaging depth for samples with a low SP and high water content (e.g. skin). However, since the wavelength dependence of the backscattering coefficient is not known a priori, the procedures, as outlined in this paper, should be followed to determine the optimum OCT imaging wavelength.

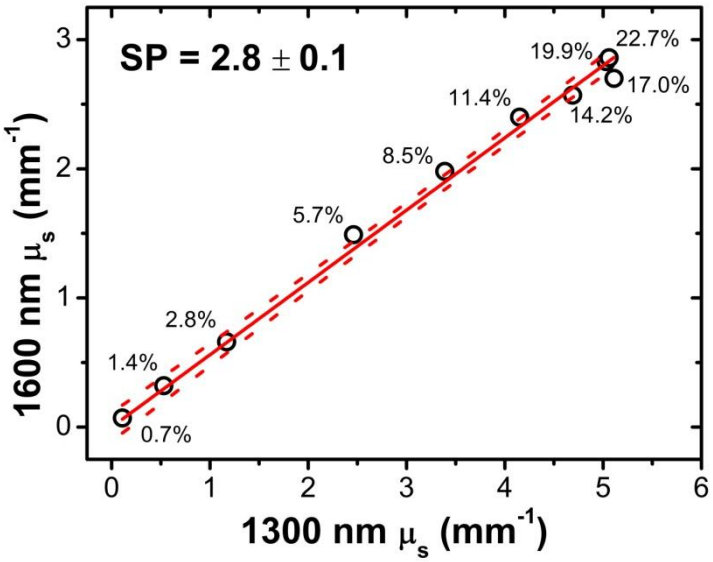

Figure 3-13. Measured μ_s at 1600 nm versus 1300 nm. Sample points are marked according to the Intralipid concentration. From a linear fit to the data (solid line) we determine the SP value for Intralipid (indicated). The dashed lines indicate the 95% confidence interval of the fit.

5. CONCLUSIONS

We present a quantitative comparison of the OCT imaging depth in Intralipid (with constant water content of 77 vol.%) at 1300 and 1600 nm. For Intralipid concentrations larger than 4 vol.% the imaging depth at 1600 nm becomes larger than for 1300 nm. We show that for high Intralipid concentrations the use of 1600 nm light gives a 30 % larger OCT imaging depth compared to 1300 nm. Despite concentration dependent scattering effects, the ratio of scattering coefficients at the two wavelengths is constant. Additionally, we observe that

difference in the backscattering at these wavelengths is small, which suggests that the backscattering phase function at 1600 nm is higher than at 1300 nm. Regarding application to biological tissues, an increase of the OCT imaging depth at 1600 nm for samples with a high scattering power parameter and low water content is expected.

REFERENCES

1. D. Huang, E. A. Swanson, C. P. Lin, J. S. Schuman, W. G. Stinson, W. Chang, M. R. Hee, T. Flotte, K. Gregory, C. A. Puliafito, and J. G. Fujimoto, "Optical Coherence Tomography," Science **254**, 1178-1181 (1991).
2. A. M. Zysk, F. T. Nguyen, A. L. Oldenburg, D. L. Marks, and S. A. Boppart, "Optical coherence tomography: a review of clinical development from bench to bedside," Journal of Biomedical Optics **12** (2007).
3. D. J. Faber, E. G. Mik, M. C. G. Aalders, and T. G. van Leeuwen, "Toward assessment of blood oxygen saturation by spectroscopic optical coherence tomography," Optics Letters **30**, 1015-1017 (2005).
4. F. J. van der Meer, D. J. Faber, M. C. G. Aalders, and T. G. Van Leeuwen, "Identification of plaque constituents using quantitative measurements of tissue optical properties by optical coherence tomography," European Heart Journal **24**, 152-152 (2003).
5. M. E. J. van Velthoven, D. J. Faber, F. D. Verbraak, T. G. van Leeuwen, and M. D. de Smet, "Recent developments in optical coherence tomography for imaging the retina," Progress in Retinal and Eye Research **26**, 57-77 (2007).
6. A. Unterhuber, B. Povazay, B. Hermann, H. Sattmann, A. Chavez-Pirson, and W. Drexler, "In vivo retinal optical coherence tomography at 1040 nm-enhanced penetration into the choroid," Optics Express **13**, 3252-3258 (2005).
7. B. Povazay, B. Hermann, A. Unterhuber, B. Hofer, H. Sattmann, F. Zeiler, J. E. Morgan, C. Falkner-Radler, C. Glittenberg, S. Blinder, and W. Drexler, "Three-dimensional optical coherence tomography at 1050 nm versus 800 nm in retinal pathologies: enhanced performance and choroidal penetration in cataract patients," Journal of Biomedical Optics **12** (2007).
8. J. M. Schmitt, A. Knuttel, M. Yadlowsky, and M. A. Eckhaus, "Optical-Coherence Tomography of a Dense Tissue - Statistics of Attenuation and Backscattering," Physics in Medicine and Biology **39**, 1705-1720 (1994).
9. Y. Yasuno, Y. J. Hong, S. Makita, M. Yamanari, M. Akiba, M. Miura, and T. Yatagai, "In vivo high-contrast imaging of deep posterior eye by 1-mu m swept source optical coherence tomography and scattering optical coherence angiography," Optics Express **15**, 6121-6139 (2007).
10. M. A. Choma, K. Hsu, and J. A. Izatt, "Swept source optical coherence tomography using an all-fiber 1300-nm ring laser source," Journal of Biomedical Optics **10** (2005).
11. G. M. Hale, and M. R. Querry, "Optical Constants of Water in the 200-nm to 200-µm Wavelength Region," Appl. Opt. **12**, 555-563 (1973).
12. B. E. Bouma, L. E. Nelson, G. J. Tearney, D. J. Jones, M. E. Brezinski, and J. G. Fujimoto, "Optical Coherence Tomographic Imaging of Human Tissue at 1.55 mu m and 1.81 mu m Using Er- and Tm-Doped Fiber Sources," Journal of Biomedical Optics **3**, 76-79 (1998).
13. H. Kakuma, K. Ohbayashi, and Y. Arakawa, "Optical imaging of hard and soft dental tissues using discretely swept optical frequency domain reflectometry optical coherence tomography at wavelengths from 1560 to 1600 nm," Journal of Biomedical Optics **13**, 014012-014016 (2008).
14. U. Sharma, E. W. Chang, and S. H. Yun, "Long-wavelength optical coherence tomography at 1.7 um for enhanced imaging depth," Opt. Express **16**, 19712-19723 (2008).
15. L. Carrion, M. Lestrade, Z. Xu, G. Touma, R. Maciejko, and M. Bertrand, "Comparative study of optical sources in the near infrared for optical coherence tomography applications," Journal of Biomedical Optics **12**, 014017-014018 (2007).
16. A. W. Sainter, T. A. King, and M. R. Dickinson, "Effect of target biological tissue and choice of light source on penetration depth and resolution in optical coherence tomography," Journal of Biomedical Optics **9**, 193-199 (2004).

17. J. M. Schmitt, A. Knuttel, and R. F. Bonner, "Measurement of Optical-Properties of Biological Tissues by Low-Coherence Reflectometry," Applied Optics **32**, 6032-6042 (1993).
18. D. J. Faber, F. J. van der Meer, and M. C. G. Aalders, "Quantitative measurement of attenuation coefficients of weakly scattering media using optical coherence tomography," Optics Express **12**, 4353-4365 (2004).
19. J. M. Schmitt, S. H. Xiang, and K. M. Yung, "Differential absorption imaging with optical coherence tomography," Journal of the Optical Society of America a-Optics Image Science and Vision **15**, 2288-2296 (1998).
20. "Refractive index database," http://refractiveindex.info.
21. A. Giusto, R. Saija, M. A. Iatì, P. Denti, F. Borghese, and O. I. Sindoni, "Optical Properties of High-Density Dispersions of Particles: Application to Intralipid Solutions," Appl. Opt. **42**, 4375-4380 (2003).
22. G. Zaccanti, S. D. Bianco, and F. Martelli, "Measurements of Optical Properties of High-Density Media," Appl. Opt. **42**, 4023-4030 (2003).
23. J. Kalkman, A. V. Bykov, D. J. Faber, and T. G. van Leeuwen, "Multiple and dependent scattering effects in Doppler optical coherence tomography," Opt. Express **18**, 3883-3892.
24. H. J. van Staveren, C. J. M. Moes, J. van Marie, S. A. Prahl, and M. J. C. van Gemert, "Light scattering in Intralipid-10% in the wavelength range of 400?1100 nm," Appl. Opt. **30**, 4507-4514 (1991).
25. C. Chen, J. Q. Lu, H. F. Ding, K. M. Jacobs, Y. Du, and X. H. Hu, "A primary method for determination of optical parameters of turbid samples and application to intralipid between 550 and 1630nm," Optics Express **14**, 7420-7435 (2006).

CHAPTER 4

Determination of the scattering anisotropy with optical coherence tomography

Published in: *Optics Express*, Vol. 19, Issue 7, pp. 6131-6140 (2011)

In this work we demonstrate measurements with optical coherence tomography (OCT) of the scattering phase function in the backward direction and the scattering anisotropy parameter g. Measurements of the OCT attenuation coefficient and the backscattering amplitude are performed on calibrated polystyrene microspheres with a time-domain OCT system. From these measurements the phase function in the backward direction is determined. The measurements are described by the single scattering model and match Mie calculations very well. Measurements on Intralipid demonstrate the ability to determine the g of polydisperse samples and, for Intralipid, g = 0.35 ± 0.03 is measured, which is well in agreement with g from literature. These measurements are validated using the Intralipid particle size distribution determined from TEM measurements. Measurements of g and the scattering phase function in the backward direction can be used to monitor changes in backscattering, which can indicate morphological changes of the sample or act as contrast enhancement mechanism.

2. INTRODUCTION

Optical coherence tomography (OCT) is a non-invasive imaging modality that is used to image the morphology of turbid media. An important application of OCT is to quantitatively determine the optical properties of tissue. The attenuation coefficient of the OCT signal can be used to characterize tissue [1-3] and to determine the OCT imaging depth [4]. In contrast to frequently reported measurements of the OCT attenuation coefficient, quantitative measurements of the OCT backscattering are reported less often. The OCT backscattering coefficient can be quantified [5] and used for tissue characterization, visualization, and/or contrast enhancement [6]. In addition, the variation of the OCT magnitude in time can provide quantitative information about flow [7] and diffusion [8]. Quantitative measurement of the OCT (or low coherence interferometry) magnitude as a function of angle and/or wavelength [9, 10] can provide information on the scattering phase function and the size of the scatterer.

The scattering phase function, which describes the angular probability distribution of the scattered light, is parameterized by the scattering anisotropy parameter g, which is the average of the cosine of the scattering angle. The scattering anisotropy plays an important role in diffusive light transport, for example in diffuse reflectance spectroscopy. Also in OCT, g plays an important role as it determines the amount of backscattering and in the quantification of multiple scattering effects in (Doppler) OCT [11]. The possibility to extract g from OCT measurements is very attractive, because, in comparison with commonly used goniometric or integrating sphere methods, the non-invasive nature of OCT allows for in-vivo application.

Two models are available for a quantitative description of the OCT signal: the single scattering model and a comprehensive model based on the Extended Huygens-Fresnel principle [12]. The first model gives good results for weakly scattering, non-absorbing media [13] and describes the OCT signal by a single exponential decay function. The latter model can be used to estimate g from a fit of the model to the OCT signal in depth, but is valid only for samples with small-angle forward scattering (e.g. high g). The obtained root-mean-square scattering angle θ_{rms} can be related to g if the phase function is known. In this model the scattering coefficient μ_s and θ_{rms} (or g) only can be separated when multiple scattering effects are significant. However, an increase of μ_s can counteract a decrease of θ_{rms} (i.e. increase of g) in the fit model and the fit parameters are not (statistically) independent [14].

Here we present a simple method based on the single scattering model to determine g from OCT measurements. We demonstrate experimentally, for the first time to our knowledge, that this model can be used for measurements of the scattering phase function in the backward direction and in specific cases for measuring g.

2. MATERIALS AND METHODS

2.1 Single scattering model of the OCT signal

In a loss less time-domain OCT system without focus tracking the OCT detector current $i_d(z)$ as a function of depth z is equal to the backscatter profile of the sample as function of z convoluted with the complex coherence function $\gamma(2z/c)$ [15]. For a perfect mirror in air positioned in the sample arm located at z = 0 (a single reflector), the OCT detector current signal is:

$$i_d(z) = \eta \,\mathrm{Re}\left\{\gamma\left(\frac{2z}{c}\right)\right\} \otimes r_{mirror} h(z)\delta(z)\sqrt{P_r P_s} \tag{4-1}$$

where η is the detector conversion factor from the incident light power to the electric current, $Re\{\}$ is the real part of the complex coherence function, c is the speed of light, r_{mirror} is the field reflection coefficient of the mirror, $h(z)$ is the confocal point spread function [16], $\delta(z)$ = 1 for z = 0 and $\delta(z)$ = 0 for all other z. The powers P_r and P_s are the powers incident on the reference and sample arm, respectively. Performing the convolution in Equation 4-1 and taking the square of the OCT signal at z = 0 ,

$$i_d(z=0)^2\Big|_{mirror} = \eta^2 \, r_{mirror}^2 P_r P_s \tag{4-2}$$

where it is assumed that $h(0)$ = 1, i.e. the mirror is in the focus. For a scattering medium the situation is more complicated. A one-dimensional single scattering model is assumed where homogenously distributed scatterers all add coherently to the OCT signal. Assuming that the OCT signal for a homogenous scattering medium is the sum of all scattering contributions (see section 4.3 for a discussion), the detector current is:

$$i_d(z) = \eta \,\mathrm{Re}\left\{\gamma\left(\frac{2zn_{med}}{c}\right)\right\} \otimes h(z)\sqrt{P_r P_s}\sqrt{\mu_{b,NA}}\sqrt{\exp(-2\mu_s z)} \tag{4-3}$$

with n_{med} the group refractive index of the medium, $\mu_{b,NA}$ the effective backscattering coefficient (quantifying the part of the light that is backscattered into the detection NA of the OCT system); μ_s the scattering coefficient. The factor 2 in the exponent of Equation 4-3 accounts for the round-trip attenuation to and from depth z. In a scattering medium with attenuation μ_s the amplitude of the OCT signal can be found by extrapolating the attenuated OCT signal to z = 0. The square of the OCT signal at the interface is:

$$i_d(z=0)^2\Big|_{scat} = \eta^2 \frac{l_c}{n_{med}} P_r P_s \mu_{b,NA} Q \tag{4-4}$$

where coherence length l_c is defined in single pass and according to Schmitt et al. [13] and Goodman [15]. Note that this coherence length definition is a factor $\sqrt{\pi/8\ln 2} \approx 0.75$ smaller than the commonly used definition related to the axial resolution in OCT, which is defined as the full width at half maximum of the Gaussian–shaped coherence point spread function of the OCT amplitude [17]. The constant Q describes the heterodyne intensity back-coupling efficiency from a scattering medium compared to that of a mirror and ranges from 0 to 1 (see section 4.3). From this analysis it can be observed that μ_b can be determined by dividing Equation 4-2 by Equation 4-4. The backscattering coefficient is:

$$\mu_{b,NA} = \frac{i_d(z=0)^2\big|_{scat}}{i_d(z=0)^2\big|_{mirror}} \frac{n_{med} r_{mirror}^2}{l_c Q} \tag{4-5}$$

with the backscattering coefficient μ_b proportional to the scattering coefficient times the phase function integrated over the NA in the backscattering direction, p_{NA}. Note that by taking the ratio of two OCT measurements additional loss factors in the OCT system do not influence the determination of μ_b.

In the absence of absorption, the scattering coefficient μ_s can be determined from the slope of the OCT signal. For media with the absorption and in the single scattering approximation, the light travels in a ballistic way and Lambert-Beer's law can be applied to calculate the total OCT attenuation coefficient μ_t, which equals $\mu_t=\mu_s+\mu_a$. Consequently, μ_s can be obtained by subtracting the absorption coefficient from the total attenuation coefficient obtained from the slope of the OCT signal. The scattering phase function in the backscattering direction can be obtained by integrating the scattering phase function $p(\theta)$ over angles from π - *NA* to π. The phase function integrated over the NA, p_{NA} describes the fraction of scattered photons which are detected by OCT system, i.e. $p_{NA}=\mu_{b,NA}/\mu_s$. Consequently, p_{NA} can be determined using Equation 4-5 and μ_s :

$$p_{NA} \equiv \int_{\pi-NA}^{\pi} p(\theta) 2\pi \sin(\theta) d\theta = \frac{\mu_{b,NA}}{\mu_s} = \frac{n_{med} r_{mirror}^2}{l_c Q \mu_s} \frac{i_d(z=0)^2\big|_{scat}}{i_d(z=0)^2\big|_{mirror}} \tag{4-6}$$

Since p_{NA} is related to the phase function, the scattering anisotropy g can be determined from a determination of p_{NA} if the shape of the phase function is known a priori.

2.2 OCT measurements

For our study we utilize a home-built time-domain OCT system, which is described in detail in Ref. [4]. In summary, light from a Fianium light source is filtered to obtain a spectrum centered at 1300 nm, which is coupled into a fixed focus OCT setup. The axial resolution of this system is 9.7 ± 0.1 µm as was determined from the full width at half maximum of the OCT

magnitude point spread function. The signal to noise ratio is 90 dB. The Rayleigh length, measured with mirror in the sample arm, is 292 ± 9 μm. The corresponding Gaussian beam waist is 9.6 ± 0.2 μm and the numerical aperture NA of the sample arm lens is 0.043 ± 0.001. Prior to the experiment, the OCT system is calibrated for quantitative measurements of the backscattered power. Due to the limited dynamic range of the OCT system, the power from the mirror is measured using different calibrated neutral density filters in the sample arm. From the dependence of the OCT signal on the optical attenuation the reflected power and the OCT magnitude can be directly compared to the signals for the scattering sample (no optical attenuation in the sample arm) in Equation 4-6.

OCT measurements on suspensions of scatterers are performed in a 1 mm thick glass cuvette. The cuvette is placed in the sample arm at ~ 70° angle relative to the incident beam to avoid specular reflections in the OCT signal. The sample arm beam is focused at the first glass-medium interface. Measurements for every solution are performed independently for 5 times. For each measurement, the average of 100 A-scans is taken. After background subtraction the OCT signal magnitude is corrected for the confocal point spread function [16]. The OCT attenuation coefficient is determined with a two parameter single exponential fit of the measured OCT signal in depth (corrected for the refractive index of water). To reduce the effects of multiple scattering, the scatterers concentration is kept low to create samples with scattering coefficients below 5 mm^{-1} (as calculated with Mie theory). In addition, only the first 500 data points (190 μm) of the OCT signal (starting at ~ 60 μm depth after sample front surface) are used for fitting the single exponential decay. The scattering coefficient is calculated by subtracting the water absorption coefficient (μ_a = 0.2 mm^{-1}) from the fitted attenuation coefficient. Finally, the scattering cross section σ_s is calculated by dividing the scattering coefficient by the known particle concentration. The OCT signal amplitude at the front glass-sample boundary is determined from the exponential fit by extending the fitting line to zero depth (see Figure 4-1). Zero depth was determined from the crossing of the OCT signal with the vertical drop line at half height. With this method the OCT signal magnitude is determined on an absolute scale in [$mW^{1/2}$] units. This is indicated in Figure 4-1 on the right hand side scale for a measurement of a scattering medium for 400 nm diameter particles. The peak of the backscattered power in the heterodyne (OCT) signal is of the order of 90 picoWatts.

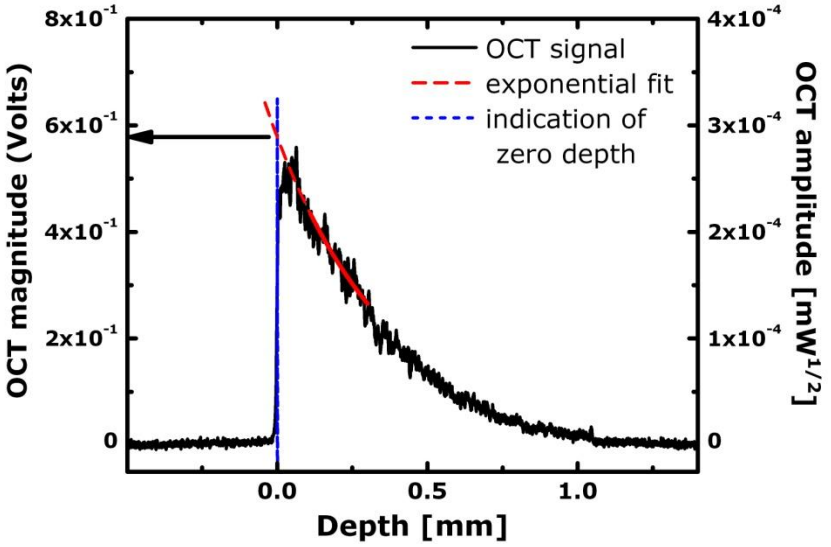

Figure 4-14. OCT measurement of backscattered power from a suspension of 400 nm diameter polystyrene microspheres in water. The vertical scale on the left is converted to absolute units of square root of power using the power calibration and is indicated on the right. The attenuation coefficient is determined from the single exponential decay fit (solid red line); the amplitude of the OCT signal from the sample surface is determined by extending the exponential fit to zero depth (dashed red line). Zero depth is indicated (dashed blue line).

2.3 Scattering samples

Polystyrene microspheres (Thermo Scientific, USA) are used as scatterers, certified by NIST traceable procedures, with the concentration of the sample calculated based on the used dilution (1 wt.% concentration). The microspheres have mean diameters of 203 ± 5, 400 ± 9, 596 ± 6, 799 ± 9, and 994 ± 10 nm and size distribution standard deviations of 4.7, 7.3, 7.7, 4.8 and 10 nm, respectively. Mie calculations are performed based on mean diameters to calculate the scattering cross section and phase function of the polystyrene particles. The refractive index of water (n_{water}=1.32) and polystyrene are used (n_{polyst}=1.57 [18]) as input. From Mie calculations, the scattering anisotropy, i.e. the g of these microspheres, is calculated to be: 0.07, 0.29, 0.62, 0.73, and 0.81 for increasing sphere diameter. Also, from the calculated phase functions, the scattering efficiency in the backscattering direction p_{NA} is calculated by integrating the phase function over the NA of the sample arm focusing lens.

Measurements performed on Intralipid samples are used as an example of our technique to a polydisperse medium. Intralipid is an aqueous suspension of polydisperse lipid droplets, which is often used as a tissue phantom for optical measurements. Recently we showed that for high Intralipid concentrations multiple and dependent scattering effects play

an important role and lead to nonlinear changes in the scattering coefficient with concentration [11]. To avoid these effects, measurements with low concentrations Intralipid (0.7, 1.4 and 2.8 vol.%) are performed. The samples are prepared by dilution of a single batch of 22.7 vol.% Intralipid (Fresenius-Kabi) with deionized water. The refractive indexes used for Mie calculations of Intralipid are: n_{water} = 1.32 for water; n_{lip} = 1.46 for lipid droplets [19].

To correlate our OCT measurements to the size of the scatterers in the polydisperse Intralipid suspension, transmission electron microscopy (TEM) measurements are performed to determine the size distribution of the scatterers in Intralipid. For TEM imaging the samples were cryoprotected with glycerin and frozen in liquid ethane at the temperature of liquid nitrogen. The samples were replicated in a vacuum better than 3×10^{-7} mbar at a temperature of -120°C. A platinum layer (2 nm) was evaporated at an angle of 45^0 and carbon (20 nm) was deposited at an angle of 90^0. The replicas were cleaned with house hold bleach and collected on 300 mesh copper grids. The replicas were then imaged with a FEI T2 electron microscope at a magnification of 26500. Images were collected with a SIS Velata camera in a 2048×2048 format. QWin-pro (Leica) software was used to determine the diameters. In total, 2019 particle diameters were measured.

3. RESULTS

3.1 Polystyrene microspheres

From an OCT measurement, like the measurement shown in Figure 4-1, the scattering coefficient for a solution of particles is determined. Figure 4-2(a) shows the scattering cross section of polystyrene microspheres for the different diameters obtained from the scattering coefficient. The experimental results are compared to Mie calculations and good agreement is observed (typical error is within 10 %). Consequently, it can be assumed that multiple scattering effects are negligible and that the single scattering model is valid for a description of the OCT signal. From the data in Figure 4-2(a) and the measured OCT magnitude at the interface, p_{NA} is determined using Equation 4-6. Measurements of p_{NA} for all diameters are used to calculate the average heterodyne intensity back-coupling efficiency Q = 0.26 ± 0.04, which is used to compare p_{NA} to Mie calculations in Figure 4-2(b). The experimental points match the calculated values reasonably well and the oscillations in p_{NA} due to the diameter dependent lobe structure of the backscattering efficiency are clearly observable.

3.2 Intralipid

The phase function in the backscattering direction p_{NA} can be used to estimate the average size of the scatterers and, consequently, g. To determine the average diameter, the crossing point of the horizontal line through the experimental point of p_{NA} and the calculated curve of p_{NA} for each scatterer size has to be found. The obtained crossing point specifies the

average particle diameter (Figure 4-2(b)). Finally, the average particle diameter corresponds to a scattering anisotropy g (Figure 4-2(c)).

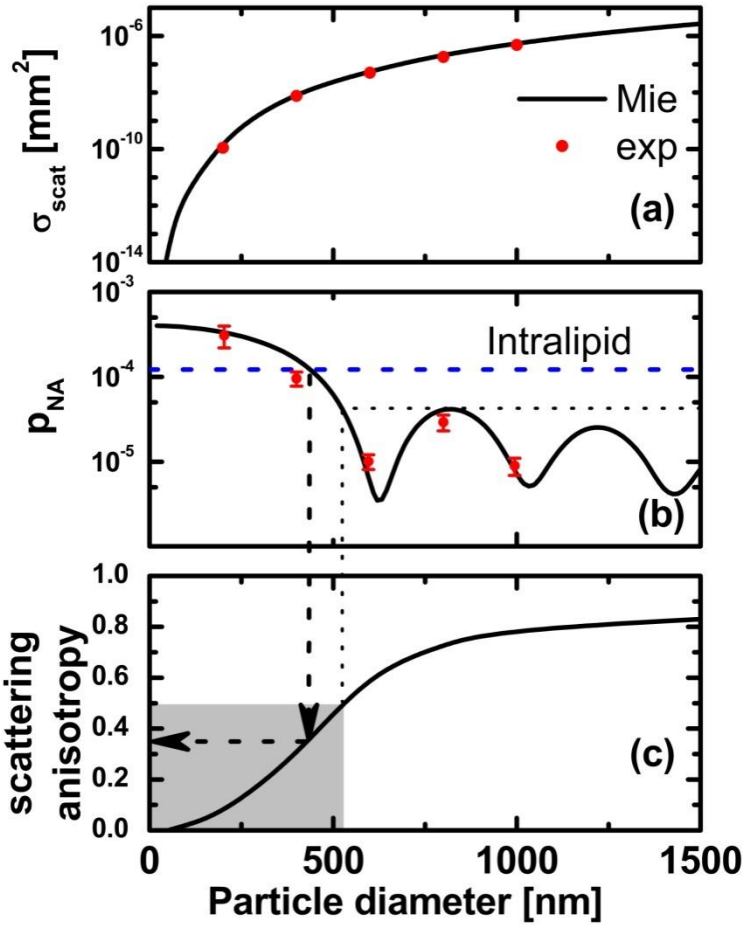

Figure 4-15. Results of Mie calculations and experimental measurements of: a) scattering cross-section of polystyrene microspheres (error bars are smaller than symbols); b) scattering phase function p_{NA} of polystyrene microspheres (error bars are standard deviations); the dashed line indicates the measured value of p_{NA} for Intralipid (standard deviation is given in the text); c) Mie calculations of g versus particle diameter at 1300 nm for polystyrene microspheres. Arrows show the average particle diameter and the g of Intralipid. Dotted lines indicate the limits of our method for particle diameter and scattering anisotropy (grey zone – region of applicability).

To demonstrate our method on non-calibrated samples we apply it to Intralipid as a polydisperse suspension of scatterers. Following the same procedure as for polystyrene microspheres, p_{NA} of Intralipid is determined. For low particle concentration, p_{NA} is independent of the concentration of scatterers and the p_{NA} values for all measured Intralipid concentrations ($1.30 \cdot 10^{-4}$, $1.26 \cdot 10^{-4}$ and $1.11 \cdot 10^{-4}$ for 0.7, 1.4 and 2.8 vol.% Intralipid correspondingly) are averaged. The resulting value ($p_{NA} = (1.22 \pm 0.21) \cdot 10^{-4}$) is plotted in Figure 4-2(b) (although the refractive indexes of polystyrene spheres and Intralipid droplets are different, this has negligible influence on the calculated p_{NA}). From Figure 4-2(b), the crossing point of the line of

the calculated p_{NA} of polystyrene microspheres and the measured p_{NA} of Intralipid corresponds to a particle diameter of 438 ± 21 nm. Consequently, from Figure 4-2(c) where we calculate g for varying particle diameter, this particle diameter corresponds to the scattering anisotropy g = 0.35 ± 0.03. This value agrees very well with previously reported measurements of g for Intralipid at 1300 nm g = 0.32 ± 0.07 [20].

To validate our experimental results, Mie theory calculations are performed based on the Intralipid particle size distribution measured by TEM, see Figure 4-3. The fraction of particles f vs. particle diameter d is given in the Table 4-1. The mean particle diameter is calculated to be 214 nm. Based on the particle size distribution in Table 4-1, the average scattering phase function p_{NA} of Intralipid in the backscattering direction is calculated using [21] :

$$p_{NA} = \frac{\sum_d p_{NA}(d)\mu_s(d)}{\sum_d \mu_s(d)} = \frac{\sum_d p_{NA}(d)\sigma_s(d)f(d)}{\sum_d \sigma_s(d)f(d)} \tag{4-7}$$

which is the average of p_{NA} over all particle diameters weighted with the scattering coefficient for every diameter. The resulting average phase function of Intralipid in the backward direction is p_{NA} = 0.94·10^{-4}. This corresponds to an average scatterer diameter d = 465 nm, which gives a scattering anisotropy g = 0.40.

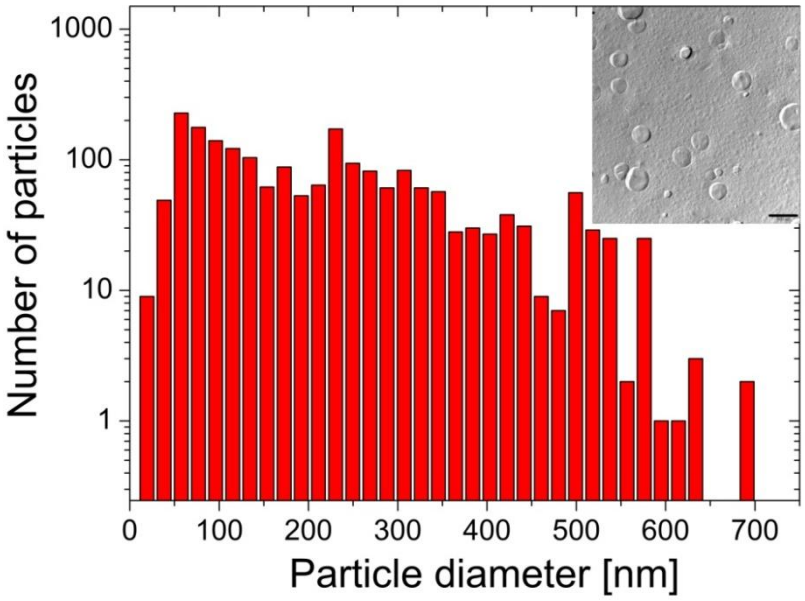

Figure 4-16. Particle size distribution of Intralipid measured by transmission electron microscopy. In total, 2019 cross-sections were measured. The mean diameter is 214 nm. Inset: TEM image of Intralipid (bar – 500 nm).

Table 4-2. Particle size distribution of Intralipid.

d [nm]	fraction	d [nm]	fraction	d [nm]	fraction	d [nm]	fraction
19.2	0.004455	**192**	0.026238	**364.8**	0.013861	**537.6**	0.012376
38.4	0.024257	**211.2**	0.031683	**384**	0.014851	**556.8**	0.00099
57.6	0.112871	**230.4**	0.085149	**403.2**	0.013366	**576**	0.012376
76.8	0.087624	**249.6**	0.046535	**422.4**	0.018812	**595.2**	0.000495
96	0.069307	**268.8**	0.040594	**441.6**	0.015347	**614.4**	0.000495
115.2	0.060396	**288**	0.030198	**460.8**	0.004455	**633.6**	0.001485
134.4	0.051485	**307.2**	0.041089	**480**	0.003465	**652.8**	0
153.6	0.030693	**326.4**	0.030198	**499.2**	0.027723	**672**	0
172.8	0.043564	**345.6**	0.028218	**518.4**	0.014356	**691.2**	0.00099

4. DISCUSSION

4.1 Method

With the demonstrated procedure it is possible to determine g for monodisperse polystyrene particles with diameters smaller than ~ 500 nm (at an OCT operating wavelength of 1300 nm). With increasing particle diameter oscillations of the scattering phase function become present and cause the measured value of p_{NA} to coincide with a multitude of diameters, which makes a unique determination of g impossible (Figure 4-2(b)). However, using additional measurements (e.g. at different wavelengths [22] or different angles [9]) or using additional information (e.g. the particle concentration) the average size of the scatterers and the scattering anisotropy g also can be determined for particles larger than ~ 500 nm.

However, even without the possibility to perform quantitative measurements, relative changes in the scattering phase function can be used to detect changes in tissue morphology and/or act as a contrast enhancement mechanism in OCT images. Furthermore, in contrast with the backscattering coefficient, the scattering phase function does not depend on the concentration of scatterers and therefore can distinguish between changes in scattering due to refractive index contrast changes or due to changes in the scatterer size.

The accuracy in the determination of p_{NA} and g depends on a large number of factors. As can be seen from Equation 4-6, μ_s, l_c, *NA* and Q are parameters that need to be accurately determined to calculate p_{NA}. The errors in all these parameters are summarized in the determination of the heterodyne intensity back-coupling efficiency Q, which has an error of

15 %. Any systematic error in Q and its relation to the theoretical value needs to be investigated (see section 4.3) as well as methods to reduce the error in Q.

4.2 Results

The physical size distribution for Intralipid (Figure 4-3) that we obtained shows a size distribution with a decreasing number of particles with increasing size. The average physical diameter is 214 nm, which is larger than 97 nm, reported by van Staveren et al. [19], which was measured for a different weight fraction solution and of Intralipid from a different manufacturer. Also our average size is larger than 123 nm, as was measured by Michels et al. [23], however, that value was obtained with an indirect method using integrating spheres measurements correlated with Monte Carlo simulations.

For polydisperse particle solutions the described method results in values for the size d and scattering anisotropy g that are averaged over the size distribution. However, since these properties are measured using an optical technique instead of a direct size measurement technique, the averages tend to underestimate the contribution of small particles since the scattering strength decreases strongly with decreasing size. For Intralipid, for example, the difference between the average physical diameter of the scatterers (214 nm) and the optically measured average scatterer diameter (438 nm) demonstrates the strong impact of the size determination method being used (TEM versus OCT). This is a well known phenomenon in, for example, dynamic light scattering where the different sizes are weighted with their respective scattering strength.

Like for the average diameter, also for g the described method is more sensitive to larger diameters [21]. However, since g is a parameter describing diffusive light transport, its optically weighted value is the only relevant parameter. The experimental value we obtain for Intralipid (g = 0.35 ± 0.03) is in good agreement with the value obtained using diffuse reflection spectroscopy (0.32 ± 0.07). In comparison to g determined from the Intralipid particle size distribution measured with TEM (g = 0.40), the value we obtained from our OCT measurements is lower. This difference can be explained by the underestimation of the small diameter particles in TEM measurements.

4.3 Efficiency factor Q

The heterodyne detection efficiency factor Q for small scatterers is of fundamental interest in OCT [6, 13, 24] and we identified two major reasons that cause a reduction of the heterodyne detection efficiency Q for a homogenous distribution of scatterers compared to a mirror to values less than 1. First, the OCT magnitude for a sum of scatterers depends on the random axial position of the scatterers in the sample (causing speckle). As a result, the envelope of the OCT signal (e.g. the mean value of the speckle pattern) is smaller than the

addition of all individual particle envelopes. Second, the OCT backscatter efficiency for small particles depends on lateral offset of the scatterer in the focused beam. The spherical wave originating from a particle is less efficiently coupled back to the single mode fiber compared to the planar wavefront reflected from the mirror. A full quantification of these effects is subject to future work.

5. CONCLUSIONS

In conclusion, we have presented experimental measurements of the scattering phase function in the backward direction p_{NA} by OCT and demonstrated the feasibility of such measurements to determine the scattering anisotropy g. The proposed method is well applicable to scatterers with diameters below ~ 500 nm (for measurements at 1300 nm). We applied this method to a polydisperse Intralipid solution and obtain g = 0.35 ± 0.03, which is close to that found in literature.

REFERENCES

1. D. J. Faber, F. J. van der Meer, and M. C. G. Aalders, "Quantitative measurement of attenuation coefficients of weakly scattering media using optical coherence tomography," Optics Express **12**, 4353-4365 (2004).
2. F. J. van der Meer, D. J. Faber, D. M. B. Sassoon, M. C. Aalders, G. Pasterkamp, and T. G. van Leeuwen, "Localized measurement of optical attenuation coefficients of atherosclerotic plaque constituents by quantitative optical coherence tomography," IEEE Transactions on Medical Imaging **24**, 1369-1376 (2005).
3. F. J. van der Meer, D. J. Faber, M. C. G. Aalders, and T. G. Van Leeuwen, "Identification of plaque constituents using quantitative measurements of tissue optical properties by optical coherence tomography," European Heart Journal **24**, 152-152 (2003).
4. V. M. Kodach, J. Kalkman, D. J. Faber, and T. G. van Leeuwen, "Quantitative comparison of the OCT imaging depth at 1300 nm and 1600 nm," Biomedical Optics Express **1**, 176-185.
5. D. Levitz, L. Thrane, M. H. Frosz, P. E. Andersen, C. B. Andersen, J. Valanciunaite, J. Swartling, S. Andersson-Engels, and P. R. Hansen, "Determination of optical scattering properties of highly-scattering media in optical coherence tomography images," Optics Express **12**, 249-259 (2004).
6. J. M. S. C.Xu, S.G.Carlier and R.Virmani, "Characterization of atherosclerosis plaques by measuring both backscattering and attenuation coefficients in optical coherence tomography," Journal of Biomedical Optics **13**, 034003 (2008).
7. Y. Wang, and R. Wang, "Autocorrelation optical coherence tomography for mapping transverse particle-flow velocity," Optics Letters **35**, 3538-3540.
8. J. Kalkman, R. Sprik, and T. G. van Leeuwen, "Path-Length-Resolved Diffusive Particle Dynamics in Spectral-Domain Optical Coherence Tomography," Physical Review Letters **105**, 198302.
9. J. Pyhtila, R. Graf, and A. Wax, "Determining nuclear morphology using an improved angle-resolved low coherence interferometry system," Optics Express **11**, 3473-3484 (2003).
10. A. E. Desjardins, B. J. Vakoc, G. J. Tearney, and B. E. Bouma, "Backscattering spectroscopic contrast with angle-resolved optical coherence tomography," Optics Letters **32**, 3158-3160 (2007).
11. J. Kalkman, A. V. Bykov, D. J. Faber, and T. G. van Leeuwen, "Multiple and dependent scattering effects in Doppler optical coherence tomography," Optics Express **18**, 3883-3892.
12. L. Thrane, H. T. Yura, and P. E. Andersen, "Analysis of optical coherence tomography systems based on the extended Huygens-Fresnel principle," Journal of the Optical Society of America A-Optics Image Science and Vision **17**, 484-490 (2000).
13. J. M. Schmitt, A. Knuttel, and R. F. Bonner, "Measurement of Optical-Properties of Biological Tissues by Low-Coherence Reflectometry," Applied Optics **32**, 6032-6042 (1993).
14. D. J. Faber, and T. G. van Leeuwen, "Are quantitative attenuation measurements of blood by optical coherence tomography feasible?," Optics Letters **34**, 1435-1437 (2009).
15. J. W. Goodman, *Statistical optics* (Wiley, New York, 1985).
16. T. G. van Leeuwen, D. J. Faber, and M. C. Aalders, "Measurement of the axial point spread function in scattering media using single-mode fiber-based optical coherence tomography," IEEE Journal of Selected Topics in Quantum Electronics **9**, 227-233 (2003).
17. C. Akcay, P. Parrein, and J. P. Rolland, "Estimation of Longitudinal Resolution in Optical Coherence Imaging," Applied Optics **41**, 5256-5262 (2002).
18. A. Unterhuber, B. Povazay, B. Hermann, H. Sattmann, W. Drexler, V. Yakovlev, G. Tempea, C. Schubert, E. M. Anger, P. K. Ahnelt, M. Stur, J. E. Morgan, A. Cowey, G. Jung, T. Le, and A. Stingl, "Compact, low-cost Ti : Al2O3 laser for in vivo ultrahigh-resolution optical coherence tomography," Optics Letters **28**, 905-907 (2003).

19. H. J. van Staveren, C. J. M. Moes, J. van Marie, S. A. Prahl, and M. J. C. van Gemert, "Light scattering in Intralipid-10% in the wavelength range of 400-1100 nm," Applied Optics **30**, 4507-4514 (1991).
20. C. Chen, J. Q. Lu, H. F. Ding, K. M. Jacobs, Y. Du, and X. H. Hu, "A primary method for determination of optical parameters of turbid samples and application to intralipid between 550 and 1630nm," Optics Express **14**, 7420-7435 (2006).
21. J. R. Mourant, J. P. Freyer, A. H. Hielscher, A. A. Eick, D. Shen, and T. M. Johnson, "Mechanisms of light scattering from biological cells relevant to noninvasive optical-tissue diagnostics," Applied Optics **37**, 3586-3593 (1998).
22. N. Bosschaart, D.Faber, T.G.van Leeuwen, M.Aalders, "Measurements of wavelength dependent scattering and backscattering coefficients by low-coherence spectroscopy," Journal of Biomedical Optics **16**, 030503 (2011).
23. R. Michels, F. Foschum, and A. Kienle, "Optical properties of fat emulsions," Optics Express **16**, 5907-5925 (2008).
24. B. Karamata, M. Laubscher, M. Leutenegger, S. Bourquin, T. Lasser, and P. Lambelet, "Multiple scattering in optical coherence tomography. I. Investigation and modeling," Journal of Optical Society of America A **22**, 1369-1379 (2005).

CHAPTER 5

OCT measurements of the optical properties of thin samples

Measurements of the optical properties of thin samples are a challenging task. Determination of the attenuation coefficient from the OCT measurements involves fitting the OCT signal in depth, something that is not possible for very thin samples. In this work we show that, with knowledge of the scattering phase function, absolute measurements of the attenuation coefficient of thin samples are possible. We demonstrate this for measurements on thin Intralipid samples and silicon based TiO_2 tissue phantoms. Furthermore, if the information about the scattering phase function is unknown, the monitoring of the relative changes in the backscattering can give insight in the dynamics of biochemical processes. Measurements of backscattering changes during induced cell death in a single layer of the retinal pigment epithelium cells are presented.

1. INTRODUCTION

Optical coherence tomography (OCT) is an imaging technique that can make high resolution images up to 1-2 mm in depth. Besides imaging, OCT can measure optical properties of the biological tissues, e.g. attenuation and scattering coefficients. A typical method for the determination of the attenuation coefficient is the fitting of a model describing the OCT signal to the detected OCT signal within a region of interest (ROI) [1]. However, most of the biological tissues have layered structure and the thickness of layers sometimes is very small, which makes the fitting procedure not always possible. For example, epithelial tissue layers with thicknesses down to 10 µm have a thickness in the order of the axial resolution and, generally speaking, the ROI should be at least 5 times the axial resolution for a proper fit. At the same time, access to the optical properties of these thin layers is necessary for early diagnosis of diseases. For example, most cancers originate from the epithelial tissue layers and the detection of changes in the optical properties of these layers can be a valuable diagnostic tool [2].

In this work, we propose methods to determine the optical properties of thin tissue layers. First, we show absolute measurements of the scattering coefficient of thin phantoms. Then, monitoring of relative changes in the backscattering in the single cell layer is demonstrated.

2. OCT MEASUREMENTS OF THE ATTENUATION COEFFICIENT OF THIN SAMPLES

To access the optical properties of thin layers, we propose a method based on the analysis of the light backscattering from the layer. The OCT signal strength depends on the scattering coefficient and the scattering phase function of a sample. In the single scattering model the square of the OCT detector current $i_d(z)$ as a function of the depth z can be described as proportional to the light power $P(z)$ backscattered from the depth z:

$$i_d(z)^2 \sim P(z) = P_0 l_c \mu_b h(z) \exp(-2\mu_t z) \tag{5-1}$$

where P_0 is the incident light power, l_c is the coherence length of the light source, μ_b is the backscattering coefficient, $h(z)$ is the confocal point spread function, and μ_t is the attenuation coefficient of a sample. The backscattering coefficient μ_b is the product of the scattering coefficient μ_s and the scattering phase function of the sample $p(\theta)$ and for the OCT geometry is described as:

$$\mu_b = \mu_s \int_{NA} p(\theta) 2\pi \sin(\theta) d\theta \equiv \mu_s p_{NA} \tag{5-2}$$

where p_{NA} is the scattering phase function integrated over numerical aperture NA of the OCT sample arm.

If specular reflections from the sample boundary are avoided, assuming that $l_c << 1/\mu_t$, and the focus position is at $l_c/2$, then the OCT signal is maximal at the depth $z \sim l_c/2$. For this depth the coherence volume is filled by scatterers and the light attenuation is negligible. Based on the OCT signal at this depth, the scattering coefficient of the sample can be calculated from Equations 5-1 and 5-2 as:

$$\mu_s = \frac{P\left(\frac{l_c}{2}\right)}{P_0 l_c h\left(\frac{l_c}{2}\right) p_{NA} \exp\left(-2\mu_t \frac{l_c}{2}\right)} \tag{5-3}$$

Because of the short coherence length of the typical OCT system, we can assume that $z=l_c/2\approx 0$ and Equation 5-3 can be simplified to the form:

$$\mu_s = \frac{P(0)}{P_0 l_c p_{NA}} \tag{5-4}$$

The light power backscattered from the zero depth $P(0)$ is proportional to the square of the OCT signal amplitude at the zero depth and can be calculated if the OCT system is calibrated prior to the measurements [3]. An unknown parameter in Equation 5-4 is p_{NA}. However, whereas μ_s depends on the size of scatterers and concentration of the scatterers, p_{NA} depends primarily on the size of scatterers. This means that if the size of scatterers is known a priori, the p_{NA} can be determined and used for measurements of μ_s.

To demonstrate a feasibility of such measurements, we performed OCT measurements with tissue phantoms. For our study we utilized a home-built time-domain OCT system, which is described in detail in Ref. [4]. In summary, light from a Fianium light source was filtered to obtain a spectrum centered at 1300 nm, which was coupled into a fixed focus OCT setup. The axial resolution of this system was 10 µm, and signal to noise ratio was 90 dB.

For OCT measurements liquid tissue phantoms with Intralipid as a scattering medium were prepared. To calculate p_{NA}, the sample was made thick enough to perform the fitting procedure for the determination of the attenuation coefficient. p_{NA} of Intralipid was measured in a 1 mm glass cuvette. The cuvette was filled with Intralipid and placed in the sample arm of the OCT setup with a focus at the front glass-Intralipid interface. Measurements were performed at different concentrations of Intralipid (0.7, 1.4, 2.8 vol.%). An exponential fit was applied to the OCT signal to determine the attenuation coefficient. The amplitude of the OCT signal at zero depth, i.e. front glass-Intralipid boundary, was used to calculate the backscattered power $P(0)$ (see Chapter 4). Finally, using Equation 5-4, the constant $M = P_0 l_c p_{NA}$ of Intralipid was calculated. All measurements were performed with the same OCT setup, and P_0 and l_c were the same for all measurements. p_{NA} characterizes the size of scatterers, what means that

changes in the concentration of scatterers has no effect on p_{NA} . This is valid for low concentrations of scatterers, where dependent scattering effects are negligible. For this experiment, only measurements with low concentrations of Intralipid (0.7 %, 1.4 %, 2.8 %) were made.

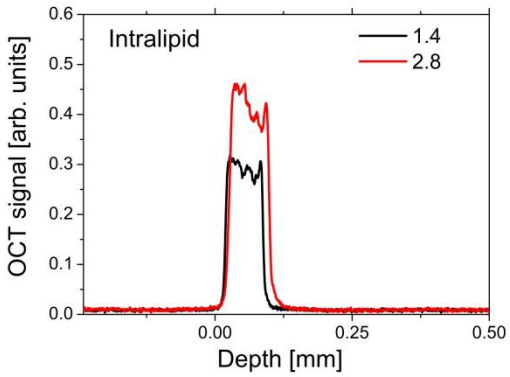

Figure 5-17. OCT measurements with thin layers of Intralipid. Measurements were performed with 1.4 vol.% (black line) and 2.8 vol.% (red line) Intralipid.

Next, thin tissue phantoms based on Intralipid were prepared. A few drops of Intralipid were deposited on a microscope glass slide and covered by another glass slide with one layer of scotch tape at both sides as a spacer. As a result, we obtained a thin layer of Intralipid with a thickness of approximately 50 µm. Phantoms were prepared with 1.4 vol.% and 2.8 vol.% Intralipid. Figure 5-1 shows the acquired OCT signals for these samples. The value of the OCT signal amplitude at zero depth was obtained using the average of the OCT signal starting at the peak signal to 20 µm depth was taken. From the amplitude of the OCT signal we determined the light backscattered power from zero depth $P(0)$. Finally, $P(0)$ was divided by the already known constant M to determine the scattering coefficient μ_s of the thin phantoms. Then we compared values of the scattering coefficient with results of the measurements with the cuvette filled with Intralipid. For 1.4 vol.% Intralipid the scattering coefficient of thick phantom was 0.56 ± 0.04 mm^{-1}, and for thin phantom 0.61 ± 0.05 mm^{-1}. For 2.8 vol.% Intralipid the scattering coefficient was 1.33 ± 0.24 mm^{-1} for thick phantom and 1.13 ± 0.25 mm^{-1} for thin the phantom. As can be seen, the results for each concentration are in good agreement.

To test our method with solid phantoms, silicone based tissue phantoms with TiO_2 as scatterers were made. The procedure of the phantom preparation is described in detail in Ref. [5]. First, we measured thick phantoms of different concentrations to determine M of TiO_2 in silicone. Measurements were performed with 0.2 wt.%, 0.3 wt.%, and 0.4 wt.% TiO_2 phantoms. In the same way as for Intralipid, the scattering coefficient and constant M were determined. Then we measured μ_s of a 50 µm thick sample with 0.2 wt.% TiO_2 concentration. Figure 5-2(a) shows the OCT signal for these samples and it can be seen that application of the fitting

procedure in this case is impossible. With our method the scattering coefficient determined for the thin phantom was μ_s = 1.75 ± 0.45 mm^{-1}, which is close to the scattering coefficient obtained from measurements with thick 0.2 wt.% TiO_2 concentration phantom (1.52 ± 0.44 mm^{-1}).

Table 5-3. Results of the experimental measurements of the scattering coefficient.

Scattering phantom	Concentration of scatterers	Thick phantom	Thin phantom
Intralipid	1.4 vol.%	0.56±0.04	0.61±0.05
	2.8 vol.%	1.33±0.24	1.13±0.25
TiO_2 in silicone	0.2 wt.%	1.52±0.44	1.75±0.45
	0.2 wt.% (two layers)	1.52±0.44	1.68±0.45

Measurements with single layer thin phantoms demonstrated that with the proposed method we can determine the scattering coefficient of thin layers. For a two-layers phantom, with a thin layer of 0.2 wt.% TiO_2 on top of a thick layer of 0.4 wt.% TiO_2, the configuration does not differ from the single layer situation (light incidents directly on the thin layer). Figure 5-2(b) shows the OCT signal for this two-layered tissue phantom. As can be seen, the OCT signal from the top layer is lower than from the underlying layer. Because the scattering phase function is the same for both layers, the difference in the backscattering is due to the difference in the scattering coefficient. We applied again our algorithm and calculated the scattering coefficient of the thin layer to be μ_s = 1.68 ± 0.45 mm^{-1}, again comparable to the expected 1.52 ± 0.44 mm^{-1}. Obtained results are summarized in Table 5-1.

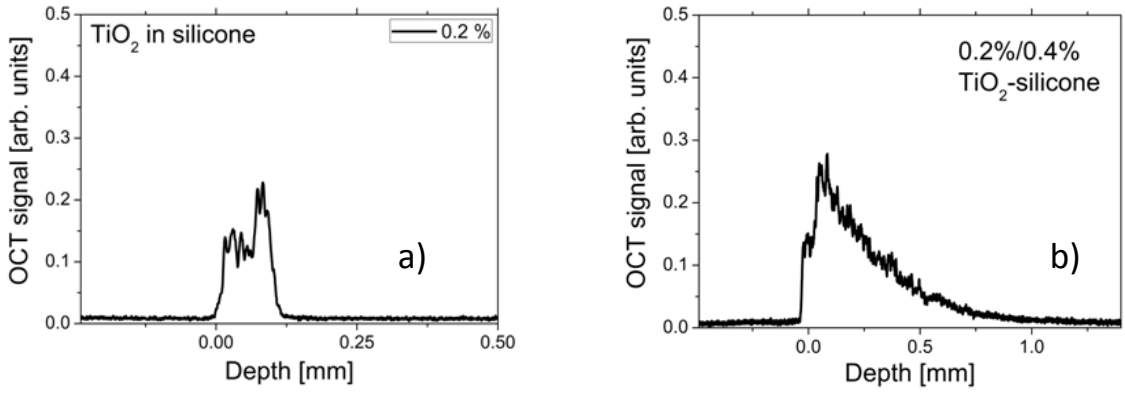

Figure 5-18. OCT measurements with solid TiO_2 phantoms: a) thin layer of 0.2 % TiO_2; b) thin layer of 0.2 % TiO_2 phantom on the top of a thick 0.4 % TiO_2 phantom.

3. OCT MEASUREMENTS OF CHANGES IN THE BACKSCATTERING OF A SINGLE LAYER OF RETINAL PIGMENT EPITHELIUM CELLS

Cells in biological tissues die through the processes of necrosis and apoptosis. Whereas necrosis (or degenerative cell death) is a process induced by external factors such as trauma or infection, apoptosis (or programmed cell death) is a regulated cellular process allowing for cells to self destruct. Apoptosis is responsible for the deletion of cells in normal tissues, and also occurs in the specific pathologic conditions [6, 7]. The morphological and biochemical changes associated with necrosis and apoptosis are different. While necrotic cells swell and lyse, affecting neighbouring cells, apoptotic cells undergo a sequence of subcellular changes [8]. The earliest changes during development of apoptosis are compaction and segregation of the nuclear chromatin with the formation of sharply delineated granular masses, and condensation of the cytoplasm. This is followed by the disintegration of nucleus and fragmentation of the cell into membrane-enclosed apoptotic bodies, containing nuclear fragments and cell organelles [9].

Apoptosis occurs in many disease states. Also, the initial response of tumor cells to successful cancer treatment is often massive apoptosis [9, 10]. This makes detection of the early morphological changes that a cell undergoes during development of apoptosis a potential tool for the diagnosis of diseases and for the monitoring of success of cancer treatment. Apoptosis is a very dynamic process, which makes it challenging to monitor it in-vivo. Most of the current methods for the detection of apoptosis are invasive and time consuming [11]. Regarding non-invasive methods, it was demonstrated that ultrasonic imaging can distinguish living, apoptotic and necrotic cells based on the backscattering strength [12]. However, the low resolution of ultrasound imaging makes it impossible to detect apoptosis in small tissue volumes. Recently it was demonstrated that optical coherence tomography (OCT) can detect changes in the optical properties of cells undergoing apoptosis [13]. Differences in the attenuation coefficient of healthy, apoptotic and necrotic cells were measured.

In OCT the attenuation coefficient and the backscattering coefficient can be determined from OCT signal (Chapter 4). Only recently the changes in the light backscattering during development of apoptosis were investigated [14]. This kind of measurements can be an additional tool for the detection of apoptosis. As discussed before in this Chapter, in thin tissue layers the fitting procedure is impossible, so that monitoring of changes in the backscattering amplitude is the only possibility to access the optical properties of the tissue under study. We proceed to demonstrate in-vitro measurements of changes in optical properties of single layer of cells during the first 90 min of induced cell death.

OCT measurements were performed with retinal pigment epithelium (RPE) cells. RPE cells appear as a monolayer in the retina, forming a barrier between the neurosensory retina

and the choroid. The choice of RPE cells was based on the fact that the disfunction of these cells plays an important role in the development of a range of ophthalmic diseases, for example age-related macular degeneration (AMD) [15]. Therefore the detection of the apoptosis in the RPE layer can help in diagnosis of eye diseases at early stages.

The human RPE cell line ARPE-19 was obtained from the Netherlands Institute for Neurosciences. The samples with cells were grown in cell culture dishes as a single monolayer of cells (thickness approximately 10 µm), which mimics RPE cell layer in the human eye. To induce cell death, 10 % ethanol was added to the culture medium (constant exposure) [16, 17]. Directly after adding of alcohol, OCT measurements were started. Prior to OCT measurement we performed fluorescence-activated cell sorting (FACS) measurements with cells treated in the same way, to make sure that the constant exposure of 10 % alcohol induces cell death.

OCT measurements were performed with a commercially available Santec HSL 2000 OCT swept-source OCT system operating at a center wavelength of 1300 nm, with an axial resolution of 10 µm. To avoid specular reflections, the direction of the incident light was set at approximately 30 degree to the normal. For each series of measurements, a dish with cultured cells was placed on a heating plate to keep the temperature of the cells at 37 degrees (culture conditions). Measurements of each sample were performed during 90 min with a 15 min interval, the size of the imaged area was 2 by 2 mm. The position of the sample was kept constant, i.e. the same area was imaged during each series of measurements. Control measurements were performed with 2 different samples, apoptosis measurements – with 3 samples. The obtained OCT signal was analyzed through the summation of amplitudes of the OCT signal from the imaged area (maximum intensity projection). Then, in each series of measurements, the ratio of the amplitude for each measurement to the amplitude for the first measurement (zero time) was calculated.

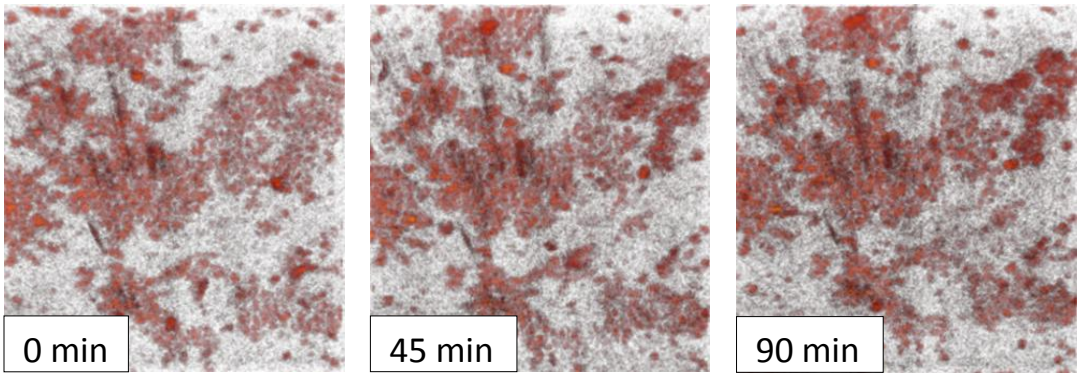

Figure 5-19. OCT images of the RPE cells layer at three different time points (indicated). The imaged area is 2x2 mm.

An example of the OCT image of the single layer of RPE cells at three different time points is shown in Figure 5-3. Darker regions are cells, and lighter regions are empty space.

Figure 5-4(a) shows the results of the OCT measurements on the RPE cells. As can be seen, during control measurements the value of the OCT signal amplitude remains approximately constant. Measurements with cells exposed to 10 % alcohol show a change in the OCT signal amplitude: for the duration of measurements (90 min), a 10 % increase in the OCT amplitude is detected. These results indicate that OCT can detect changes in the backscattering, induced by (intra)cellular processes in the single cell layer.

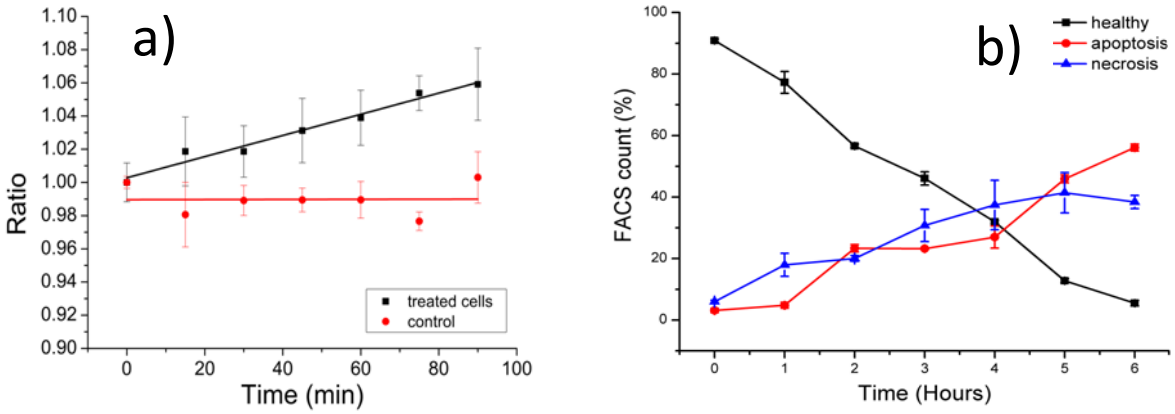

Figure 5-20. a) OCT signal amplitude changes during measurements of RPE cells (healthy (R^2=0.20) and treated by 10 % alcohol (R^2=0.98)). The ratios are calculated relative to zero time point measurements; b) FACS measurements of RPE cells treated by 10 % alcohol.

Our hypothesis is that with the addition of alcohol the cells are forced to go into apoptosis, and that during the measurements only healthy and apoptotic cells are imaged. To verify that and to identify the processes responsible for changes in the light scattering, the OCT measurements were compared with FACS measurements. RPE cells were exposed constantly by 10 % alcohol and FACS measurements were performed every hour. The FACS measurements demonstrated that the amount of healthy cells decreases with time and the amount of necrotic and apoptotic cells increases in time (Figure 5-4(b)). Therefore, the changes observed in the OCT signal can be related to these processes. Additionally, the design of our OCT experiment allowed further differentiation of the processes induced by the 10 % alcohol. We observed that with the addition of higher concentrations of alcohol (which resulted in instantaneous necrosis), necrotic cells rapidly detached from the bottom of the cell dish. Probably this is due to the loss of the cell integrity during necrosis, i.e. rupture of the cell membrane. Consequently, detachment of the cell from the dish bottom may be considered as a confirmation of the cell death (necrotic state). For our configuration of the experiment this means that cells, which

remain attached to the dish bottom, are assumed to be either apoptotic or healthy, and cells which are gone assumed to be necrotic. During OCT measurements (90 minutes), almost all measured cells remained attached to the dish, i.e. the alcohol concentration was not high enough for cells to go to direct necrosis and not enough time for cells to go to necrotic state through process of apoptosis. This leads to conclusion that the detected changes in the OCT signal in this experiment are due to the process of apoptosis.

If we compare control measurements and measurements with cells exposed to alcohol, we see distinct trends in the ratios of the OCT signal amplitude: the ratio is constant for control measurements and increases in time during measurements of cells with alcohol. This suggests that during early development of apoptosis backscattering of light increases. This information can be used for the detection of apoptosis in thin cell mono-layers, like in real biological tissues (RPE layer, epithelial tissue) where standard fitting procedure is impossible.

Changes in backscattering can be caused by different effects: change in the size and shape of scatterers or in the number of scatterers due to morphological changes, or a change in the relative refractive index of the scatterers over the surrounding medium due to biochemical changes. We speculate that for the duration of the OCT experiment it is more likely that only changes in the size of scatterers have an effect on the detected OCT signal [18]. This can include changes in the nuclear size and swelling of cytoplasmic structures, such as mitochondria [19]. However, apoptosis is a fast process, and, even for the duration of our experiment, nuclear disintegration can take place resulting in an increase in the number of scatterers and changes in the refractive index contrast.

Longer time monitoring of changes in backscattering can be interesting for further understanding of intracellular processes during development of apoptosis. However, in the presented experimental configuration this is difficult due to increasing numbers of necrotic cells in time, and, as a consequence, detachment of these cells from the bottom and migration of these cells away from the imaged area.

The method demonstrated here has a number of advantages in comparison with previously reported methods for monitoring of apoptosis. First of all, it allows for the measurement of changes in optical properties of a single layer of cells. Secondly, it allows for the in-vivo monitoring of optical properties of the thin tissue layers. This feature is especially important for assessment of the changes in scattering during drug treatment to see direct response of cells to treatment. Finally, for in-vitro measurements, differentiation of apoptotic and necrotic cells is may be possible due to effect of detachment of necrotic cells from the cell dish.

4. CONCLUSIONS

Our measurements show that OCT can provide access to the optical properties of thin samples. Particularly, we demonstrated absolute measurements of the attenuation coefficient in tissue phantoms, and measurements of relative changes in the backscattering in a single layer of RPE cells. Regarding absolute measurements of the attenuation coefficient, we showed that with knowledge of the scattering phase function, the scattering coefficient can be calculated. This method can be useful for measurements in thin layers of biological tissue.

For the measurements of the backscattering of thin layers of RPE cells, we monitored changes in the light backscattering during induced cell death. We argued that our experimental configuration is such that only healthy and apoptotic cells contribute to the signal. We demonstrated that healthy and cells treated by alcohol have detectable difference in the backscattering, which opens new possibilities for in-vivo detection of apoptosis. Our method can be used for the detection of apoptosis at early stages, where other methods are less effective.

REFERENCES

1. D. J. Faber, F. J. van der Meer, and M. C. G. Aalders, "Quantitative measurement of attenuation coefficients of weakly scattering media using optical coherence tomography," Optics Express **12**, 4353-4365 (2004).
2. R. S. Gurjar, V. Backman, L. T. Perelman, I. Georgakoudi, K. Badizadegan, I. Itzkan, R. R. Dasari, and M. S. Feld, "Imaging human epithelial properties with polarized light-scattering spectroscopy," Nature Medicine **7**, 1245-1248 (2001).
3. V. M. Kodach, D. J. Faber, J. van Marle, T. G. van Leeuwen, and J. Kalkman, "Determination of the scattering anisotropy with optical coherence tomography," Optics Express **19**, 6131-6140.
4. V. M. Kodach, J. Kalkman, D. J. Faber, and T. G. van Leeuwen, "Quantitative comparison of the OCT imaging depth at 1300 nm and 1600 nm," Biomedical Optics Express **1**, 176-185.
5. D. M. de Bruin, R. H. Bremmer, V. M. Kodach, R. de Kinkelder, J. van Marle, T. G. van Leeuwen, and D. J. Faber, "Optical phantoms of varying geometry based on thin building blocks with controlled optical properties," Journal of Biomedical Optics **15**, 025001-025010.
6. C.S. Mulvey, A.L.Curtis, S.K. Singh, and I.J. Bigio, "Elastic scattering spectroscopy as a diagnostic tool for apoptosis in cell cultures," IEEE Journal of Selected Topics in Quantum Electronics **13**, 1663-1670 (2007).
7. J. I. Majno G., "Apoptosis, Oncosis, and Necrosis. An Overview of Cell Death," American Journal of Pathology **146**, 3-15 (1995).
8. C. A. S. C.S.Mulvey, I.J.Bigio, "Wavelength-dependent backscattering measurements for quantitative real-time monitoring of apoptosis in living cells," Journal of Biomedical Optics **14**, 064013 (2009).
9. J. F. R. Kerr, C. M. Winterford, and B. V. Harmon, "Apoptosis. Its significance in cancer and cancer Therapy," Cancer **73**, 2013-2026 (1994).
10. S. W. L. a. A. W. Lin, "Apoptosis in cancer," Carcinogenesis **21**, 485-495 (2000).
11. R. Sgonc, and J. Gruber, "Apoptosis detection: an overview," Experimental Gerontology **33**, 525-533 (1998).
12. G.J. Czarnota, M.C.Kolios, H. Vaziri, S. Benchimol, F.P. Ottenmeyer, M.D. Sherar and J.W. Hunt, "Ultrasonic biomicroscopy of biable, dead and apoptotic cells," Ultrasound in Medicine and Biology **23**, 961-965 (1997).
13. F. van der Meer, D. Faber, M. Aalders, A. Poot, I. Vermes, and T. van Leeuwen, "Apoptosis- and necrosis-induced changes in light attenuation measured by optical coherence tomography," Lasers in Medical Science **25**, 259-267.
14. G. Farhat, V. X. D. Yang, G. J. Czarnota, and M. C. Kolios, "Detecting cell death with optical coherence tomography and envelope statistics," Journal of Biomedical Optics **16**, 026017-026017.
15. L. V. Del Priore, Y.-H. Kuo, and T. H. Tezel, "Age-Related Changes in Human RPE Cell Density and Apoptosis Proportion In Situ," Investigative Ophthalmology and Visual Science (2002), pp. 3312-3318.
16. I. Kurose, H. Higuchi, S. Miura, H. Saito, N. Watanabe, R. Hokari, M. Hirokawa, M. Takaishi, S. Zeki, T. Nakamura, H. Ebinuma, S. Kato, and H. Ishii, "Oxidative stress-mediated apoptosis of hepatocytes exposed to acute ethanol intoxication," Hepatology **25**, 368-378 (1997).
17. M. G. Neuman, N. H. Shear, R. G. Cameron, G. Katz, and C. Tiribelli, "Ethanol-induced apoptosis in vitro," Clinical Biochemistry **32**, 547-555 (1999).
18. C. S. Mulvey, K. Zhang, W.-H. B. Liu, D. J. Waxman, and I. J. Bigio, "Wavelength-dependent backscattering measurements for quantitative monitoring of apoptosis, Part 2: early spectral changes during apoptosis are linked to apoptotic volume decrease," Journal of Biomedical Optics **16**, 117002-117010.

19. J. R. Mourant, M. Canpolat, C. Brocker, O. Esponda-Ramos, T. M. Johnson, A. Matanock, K. Stetter, and J. P. Freyer, "Light scattering from cells: the contribution of the nucleus and the effects of proliferative status," Journal of Biomedical Optics **5**, 131-137 (2000).

CHAPTER 6

Wavelength swept Ti:Sapphire laser

Published in: *Optics Communications (2008)*, 281 (19). pp. 4975-4978.

In this study we demonstrate electronic wavelength sweeping of a continuous wave Ti:Sapphire laser using an acousto-optic tunable filter (AOTF). The dependence of the laser output on the sweeping frequency and on the spectral tuning range was investigated. The lasing up to maximum scan rate 11 kHz for 10 nm tuning range and 5 W pump power was achieved. We detected and quantified the asymmetry in the output for opposite scan directions. We theoretically characterized the maximum sweeping frequency for swept lasers with AOTF's and confirmed calculated results by measurements.

Tunable lasers are an indispensable tool in various scientific fields. As a result of intense research efforts, different wavelength tuning mechanisms have been reported. However, emerging applications promote the development of new tunable lasers with specific characteristics. In particular, significant attention was attracted to wavelength swept lasers. In the sweeping regime the laser output scans continuously and repeatedly over a wide spectral range. Swept lasers have many applications in fields such as spectroscopy [1] or optical coherence tomography (OCT) [2]. For OCT systems, continuously swept lasers with narrow instantaneous line width and broad spectral tuning range are required to achieve long imaging depth and high axial resolution. The sweeping frequency determines the imaging speed and, therefore, it is highly desirable to have this parameter in the range of tens kHz. Although unprecedented sweep rates have been demonstrated with Fourier domain mode locking technique [3, 4], conventional slower tuning techniques are still attractive. For example, in line field OCT, in which swept lasers with low sweeping frequencies (few kHz) can be used [5].

Sweeping can be performed mechanically with dispersive elements as diffraction gratings or prisms [6, 7]. However, mechanical rotation of these elements or their related mirrors complicates the design and/or induces limited stability and tuning speed. Electronic tuning avoids such imperfections. Particularly, acousto-optic tunable filters (AOTF) are capable of yielding stable and fast performance. They offer a wide tuning range, high switching speed (in the range of microseconds) and stable operation against vibration (due to non-mechanical structure). AOTF's were used for tuning of dye lasers [8], semiconductor lasers [9, 10], and pulsed Ti:Sapphire lasers [11]. The latter one was demonstrated in a random wavelength access regime. In this communication we report, first time to our knowledge, the development of a swept continuous wave (CW) Ti:Sapphire laser. Such lasers, operated near 800 nm, where absorption of the light in biological tissues is relatively low, are attractive for implementation in OCT systems and for spectroscopic measurements. We investigated laser sweeping characteristics and the influence of the AOTF as a tunable filter on the laser functioning.

We constructed our laser on the basis of a Z-fold linear cavity CW Ti:Sapphire laser (Del Mar Photonics). We inserted an AOTF in the cavity, replaced an output coupler with a high reflectivity mirror and performed the necessary realignment. The resulting configuration of the swept laser is presented in Figure 6-1. The cavity consists of concave mirrors M4, M5 (100 mm radii of curvature) and flat mirrors M6, M7, M8 (highly reflective in the range 720-940 nm). The physical length of the cavity is 1.5 m. The water cooled Brewster-cut Ti:Sapphire crystal is 13 mm long with 0.08 wt.% titanium concentration. The pump source used is a 532 nm Spectra-Physics Millennia Pro S laser that produces vertically polarized CW optical radiation. The pump beam, after passing a half-wave plate, is directed by the mirrors M1, M2 and M3 to the cavity and is focused into the crystal by the 80 mm focal length lens. Before transformation to tunable operation, with an 8% output coupler and operated in CW mode, the laser had a threshold

pump power of 1.15 W and 22 % slope efficiency. For sweeping operation we implemented the non-collinear TeO_2 AOTF (TF900-400, Gooch and Housego PLC) with a tuning range of 700 - 1100 nm. The filter resolution ranges almost linearly from 0.4 nm at 700 nm to 0.6 nm for 870 nm diffracted light wavelength. The cavity is designed in such a way that diffracted light is back-reflected to the AOTF by the mirror M8 and the zero-order output of the AOTF is used as the laser output. Manufacturer specified diffraction efficiency is more than 90 %, indicating that more than 90 % of the diffracted light is coupled back to the cavity. The angle between diffracted-order and 0-order beams is ≈ 2.6 degrees. The AOTF's diffracted beam pointing stability allows us to avoid the use of the additional optics for keeping the diffracted beam under a constant angle [11]. Wavelength sweeping is performed by applying a triangular shaped drive signal from a function generator (Hameg 8030-5) to the voltage controlled oscillator (21039-78-0.25 AMVCO, NEOS Technologies INC), which creates an RF-signal with 0.25 W maximum power for acoustic wave excitation. Changes in the frequency of the acoustic waves from 40 MHz to 65 MHz (1.8 – 8.3 V drive signal) correspond to diffracted wavelengths from 1020 nm to 665 nm, respectively. We distinguish forward and backward scans when the driving signal voltage increase or decrease respectively. In relation to this, we use the term "sweeping frequency" to describe the periodicity of the waveform which drives the AOTF.

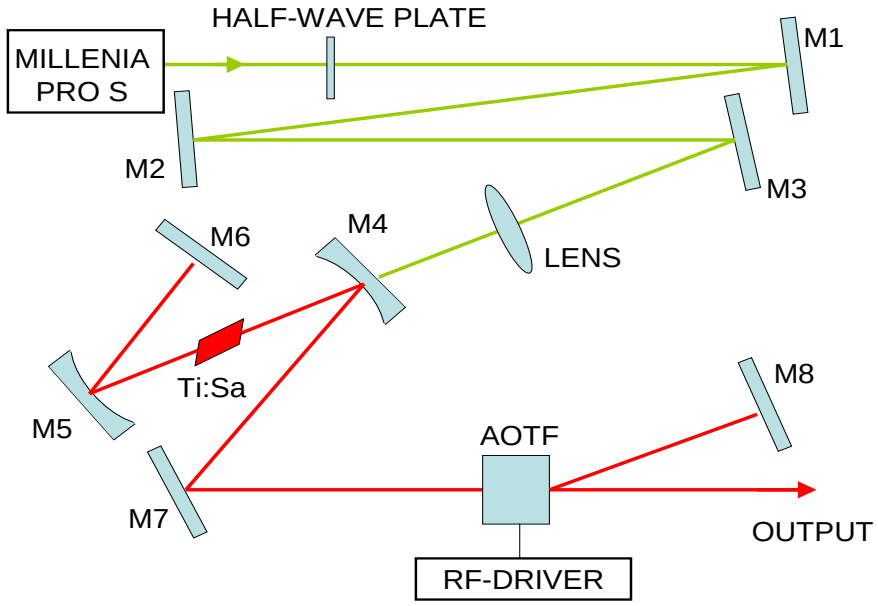

Figure 6-21. Schematic representation of the swept laser with AOTF as tunable element.

For quantitative characterization of the sweeping dynamics we considered the influence of the following controllable parameters: spectral tuning range, pump power and sweeping frequency. The averaged output power was measured for a constant spectral tuning range (from 755 nm to 855 nm) as a function of sweeping frequency with 3, 4 and 5 W pump powers. We detected lasing only in a limited range (Figure 6-2). The increase of pump power resulted in the increase of the maximum sweeping frequency. At the same time, the minimum sweeping frequency changed slightly.

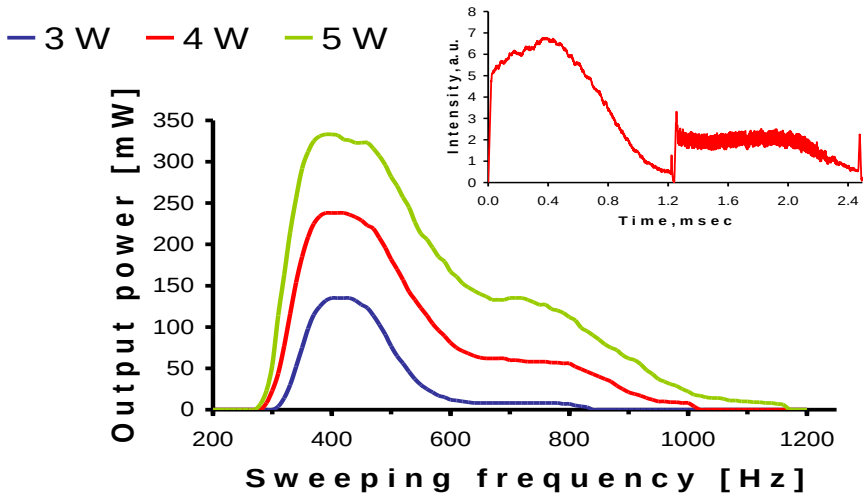

Figure 6-2. Laser output power vs. sweeping frequency for 3, 4 and 5 Watts pump powers (755-855 nm spectral tuning range). Inset: typical output intensity profiles for backward (from 0 to 1.22 msec) and forward (from 1.22 to 2.44 msec) scans (410 Hz sweeping frequency, 100 nm tuning range). The noisy output for forward scan is due to AOTF induced RF-shift (discussed in the text).

We supposed that presence of the minimum frequency is due to a decrease of the AOTF diffraction efficiency for low sweeping rates (more specifically, low AOTF tuning rate). To verify this we measured the AOTF's diffraction efficiency with another CW Ti:Sapphire laser (Spectra Physics model 3900 S). The laser beam (100 mW power, 800 nm wavelength, instantaneous line width < 1GHz) was directed to the AOTF, which was placed outside the laser cavity. We measured the light intensity in the diffracted-order beam during sweeping operation of the AOTF. The obtained results are presented in Figure 6-3. With decreasing sweeping frequency, the diffraction efficiency significantly drops. Furthermore, we observed a slow decrease of the diffraction efficiency for high sweeping frequencies. We suggest that such behavior is due to changes in the effective power of the drive signal for different sweep rates: the diffraction efficiency peaks at a certain RF drive power, deviation from which degrades performance of the AOTF. The stability of the drive signal power in the sweeping regime needs further investigation.

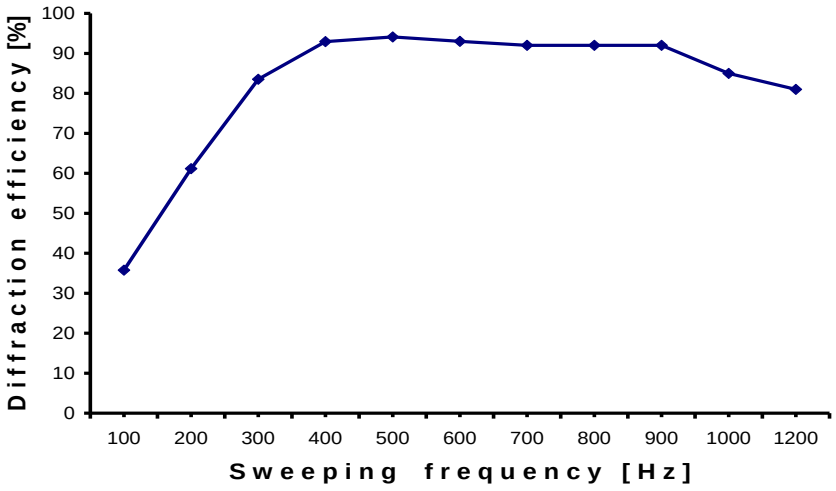

Figure 6-3. AOTF's diffraction efficiency for different sweeping frequencies. Measurements were made at 800 nm for a spectral tuning range of 755-855 nm.

Due to the absence of lasing in the non-sweeping regime we performed measurements of the instantaneous line width with a variable-delay Michelson interferometer in the sweeping regime. We measured the coherence length of the laser emission. The line width for backward and forward scans was calculated as 0.2 nm for the 5W pump power, 100 nm (750-850 nm) wavelength scan range, and the sweeping frequency of 550 Hz. With decreasing sweeping frequency the line width became narrower for backward scan and wider for forward scan (0.16 nm and 0.24 nm for 400 Hz respectively).

Depending on the pump power and tuning parameters the laser generated pulses or CW output. With increase of the sweeping frequency we observed transient dynamics from CW to pulse mode operation and back to CW. This pulsed behavior can be explained by laser spiking. This process, most pronounced for solid-state lasers, leads to the generation of a regular sequence of peaks (spikes) with few microseconds time separation after switching on or after creating disturbances during laser operation [12]. The spiking in the solid-state lasers usually damps out and leads via relaxation oscillation to the establishment of CW output. We observed in our laser, due to tuning dynamics, undamped spiking: by tuning the filter we constantly influenced the cavity losses and the establishment of the steady state conditions was prevented.

Based on a semiconductor laser with a Fabry-Perot filter as tunable element, Huber et al. discussed the limiting factors for swept lasers [13]. The maximum achievable sweep rate is limited by the time constant to build up lasing from the amplified spontaneous emission background, which depends on the laser gain, the pump power, and the cavity round-trip time.

For CW solid-state lasers this time constant is large, which means that many round-trips are required to reach threshold. In addition, for our laser, the inelastic scattering of the photons with the AOTF's traveling acoustic waves causes a radio-frequency shift (RF-shift) of the circulating radiation [14]. For each cavity round-trip light passes the AOTF twice (in opposite directions). During the reverse pass the frequency shift is not cancelled but accumulated. As a consequence a growing unidirectional RF-shift is induced (in the frequency domain). This shift can be parallel or opposite to the wavelength scan direction of the AOTF, which results in dissimilar laser output for opposite scans (Figure 6-2). During a forward scan, the modes are RF-shifted towards the trailing edge of the AOTF pass band, reducing the available time for lasing build up. Conversely, during a backward scan the directions of movement of RF-shift and trailing edge coincide and the available build-up time is longer. Consequently, the threshold pump power for lasing for the forward scan direction is higher than for the backward direction (Figure 6-4). We also note that for a constant spectral tuning range the difference in the maximum sweeping frequency for forward and backward scan directions increases from ~20 Hz to ~250 Hz (for pump powers higher than ~ 2.8 W). We explain this by the wavelength dependence of the gain factor: the high gain near 800 nm promotes the generation to start in this spectral region with smaller number of round-trips and accordingly smaller RF-shift. With increase of the pump power, the laser generation appears in the lower gain regions with larger number of round-trips and, as a consequence, larger RF-shift.

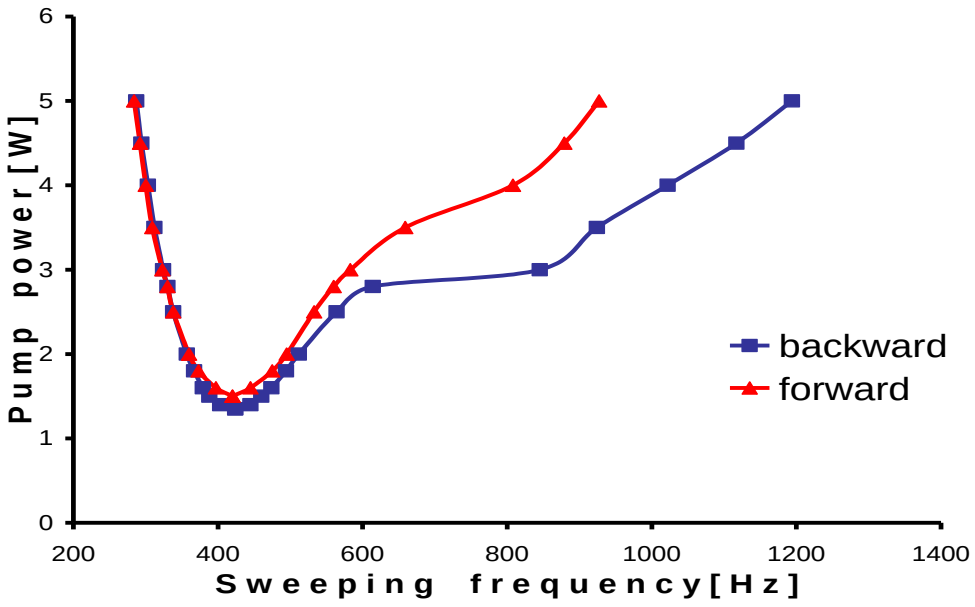

Figure 6-4. Threshold pump power versus sweeping frequency (755-855 nm tuning range) for forward and backward scans. Lasing was observed only for the pump powers higher than indicated by the curves.

For estimation of the highest accessible sweeping frequency, we use similar approximations as in [13], but taking into account the additional RF-shift. The maximum sweeping frequency can be described as:

$$\nu_{\max} = \frac{\Delta\lambda_{AOTF} \pm (n \times \Delta\lambda_{RF})}{2 \times n \times \tau_{rt} \times \Delta\lambda} \tag{6-1}$$

where $\Delta\lambda_{AOTF}$ is the AOTF resolution, n is the number of round-trips to reach the lasing threshold from spontaneous emission, $\Delta\lambda_{RF}$ is the RF-shift for one cavity round-trip, τ_{rt} is the cavity round-trip time and $\Delta\lambda$ is the spectral tuning range. The second term in the numerator represents the influence of the RF-shift with the positive sign for the backward scan and the negative sign for the forward scan (in our case).

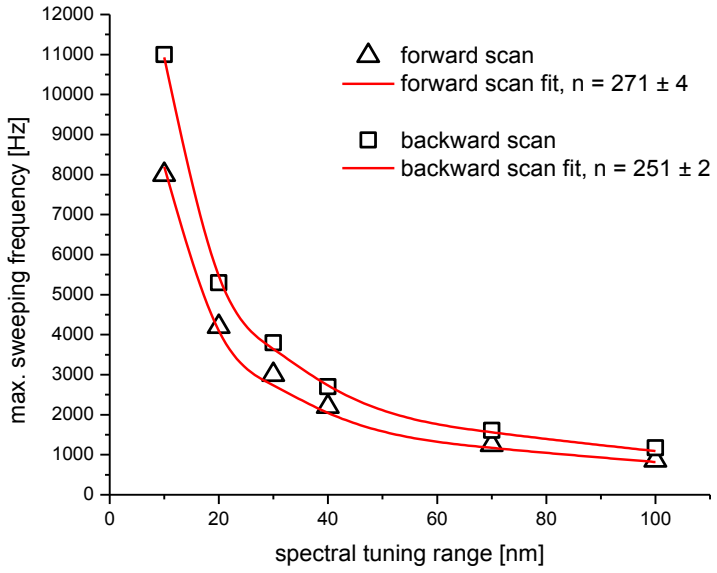

Figure 6-5. Maximum sweeping frequency versus tuning range for forward and backward scans (5W pump power). The solid curves show nonlinear least squares fits using Eq. 1 with the number of round trips as the free running parameter. The other parameters were fixed at the following values: $\Delta\lambda_{AOTF}$ = 0.5 nm; $\Delta\lambda_{RF}$ = 0.0002 nm; τ_{RT} = 10 ns.

From Equation 6-1 is seen that to attain high sweeping rates a short laser cavity, high gain, broad AOTF's band pass, and large RF-shift are required. Equation 6-1 also shows that higher sweeping frequencies can be achieved by reduction of the spectral tuning range. To demonstrate this we measured maximum scan rates for shorter tuning ranges (10, 20, 30, 40, 70 and 100 nm) and compared the results with theoretical predictions. Non-linear least squares fits with the number of round trips as the free running parameter are shown in Figure 6-5. Other parameters are listed in the figure caption. This yielded the following values for the

number of roundtrips: $n = 271$ for the forward scan direction; $n = 251$ for the backward scan direction. For the 5W pump power and 10 nm spectral range (from 795 to 805 nm) the maximum scan frequency for which lasing was detected was highest (8 kHz for the forward scan and 11 kHz for the backward scan) (Figure 6-5). On the contrary, for the spectral range of 185 nm (from 725 to 910 nm) the maximum sweeping frequency was only 450 Hz. The increase of the sweeping frequency leads to a narrowing of the spectral output (due to reduction of the lasing build-up time) (Figure 6-6). The minimum sweeping frequency was also tuning range dependent: for wider spectral ranges it is lower, which is a consequence of the fact that the tuning speed (e.g. describing the frequency of the signal applied to the RF-driver, which in turns generates the signal governing the AOTF's diffraction efficiency) is the product of the sweeping frequency and spectral tuning range. To keep the same tuning speed, increase of one parameter leads to the decrease of the other. Although existence of this low limit is not relevant for OCT applications, behavior of the AOTF in sweeping regime of operation needs further investigations.

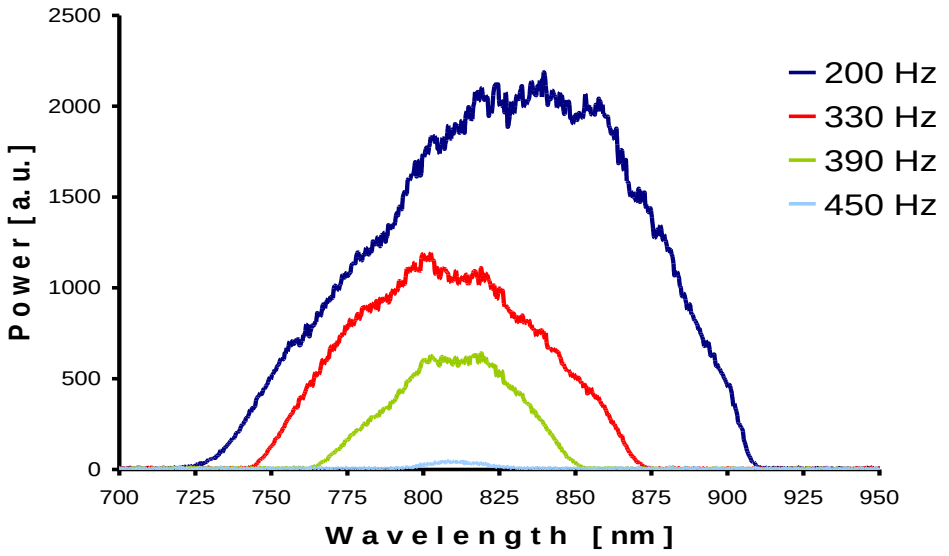

Figure 6-6. Output spectrums for 5W pump power, 680-980 nm spectral tuning range and different sweeping frequencies.

In conclusion, we developed an electronically wavelength swept CW Ti:Sapphire laser. We detected and quantified the influence of the AOTF RF-shift. We measured the changes in the AOTF diffraction efficiency during sweeping regime of operation. Our results demonstrate that the laser output depends on the tuning parameters. A reduced spectral tuning range allows higher scan rates and vice versa. The instantaneous line width is sweeping frequency dependent. Additionally, forward and backward scan directions are not similar. Such lasers with flexible output characteristics can be useful light sources for different applications, in particular OCT. Depending on the application, appropriate tuning parameters can be chosen.

REFERENCES

1. J. Wang, S. T. Sanders, J. B. Jeffries, and R. K. Hanson, "Oxygen measurements at high pressures with vertical cavity surface-emitting lasers," Applied Physics B: Lasers and Optics **72**, 865-872 (2001).
2. A. F. Fercher, C. K. Hitzenberger, G. Kamp, and S. Y. Elzaiat, "Measurement of Intraocular Distances by Backscattering Spectral Interferometry," Optics Communications **117**, 43-48 (1995).
3. R. Huber, D. C. Adler, and J. G. Fujimoto, "Buffered Fourier domain mode locking: unidirectional swept laser sources for optical coherence tomography imaging at 370,000 lines/s," Optics Letters **31**, 2975-2977 (2006).
4. W. Wieser, B. R. Biedermann, T. Klein, C. M. Eigenwillig, and R. Huber, "Multi-Megahertz OCT: High quality 3D imaging at 20 million A-scans and 4.5 GVoxels per second," Optics Express **18**, 14685-14704.
5. S. W. Lee, and B. M. Kim, "Line-field optical coherence tomography using frequency-sweeping source," IEEE Journal of Selected Topics in Quantum Electronics **14**, 50-55 (2008).
6. B. Golubovic, B. E. Bouma, G. J. Tearney, and J. G. Fujimoto, "Optical frequency-domain reflectometry using rapid wavelength tuning of a Cr4+:forsterite laser," Optics Letters **22**, 1704-1706 (1997).
7. N. J. Vasa, M. Fujiwara, S. Yokoyama, M. Uchiumi, and M. Maeda, "Tuning of a Ti3+:Sapphire Laser by an Electro-Optic Beam Deflection Method," Applied Optics **42**, 5512-5516 (2003).
8. D. J. Taylor, S. E. Harris, S. T. K. Nieh, and T. W. Hansch, "Electronic Tuning of a Dye Laser Using the Acousto-Optic Filter," Applied Physics (1971), pp. 269-271.
9. E. V. Andreeva, L. N. Magdich, D. S. Mamedov, A. A. Ruenkov, M. V. Shramenko, and S. D. Yakubovich, "Tunable semiconductor laser with an acousto-optic filter in an external fibre cavity," Quantum Electronics **36**, 324-328 (2006).
10. K. T. K.Takabayashi, N. Hashimoto, M.Doi, S. Tomabechi, T. Nakazawa and K. Morito, "Widely (132 nm) wavelength tunable laser using a semiconductor optical amplifier and an acousto-optic tunable filter," Electronics Letters **19** 1187-1188. (2004).
11. S. Wada, K. Akagawa, and H. Tashiro, "Electronically tuned Ti:sapphire laser," Optics Letters **21**, 731-733 (1996).
12. A.E.Siegman, *Lasers* (Oxford University Press, 1986).
13. R. Huber, M. Wojtkowski, K. Taira, J. G. Fujimoto, and K. Hsu, "Amplified, frequency swept lasers for frequency domain reflectometry and OCT imaging: design and scaling principles," Optics Express **13**, 3513-3528 (2005).
14. Y. Wang, N. Saito, S. Wada, and H. Tashiro, "Narrow-band, widely electronically tuned frequency-shifted feedback laser," Optics Letters **27**, 515-517 (2002).

CHAPTER 7

Discussion and conclusions

Optical Coherence Tomography (OCT) is a relatively novel imaging technique that has found many applications in medicine, e.g. in ophthalmology and cardiology, and its potential application is being studied in various medical disciplines, e.g. in dentistry, dermatology, urology and developmental biology. The strength of OCT is its capability to perform non-invasive, high resolution imaging of tissue structures, with resolutions ranging from 1 – 20 μm. The cross-sectional and 3-dimensional OCT images provide valuable information of the tissue under study, e.g. the retina or the vascular wall. Furthermore, sophisticated analysis of the OCT signals allows the extraction of morphological and physiological information from the tissue. The major weaknesses of OCT are its limitations in imaging depth and in intrinsic tissue contrast, which hamper the progress of OCT into an optical biopsy method [1]. Both limitations are largely influenced by the wavelength dependent optical properties of the tissue under study. In this thesis, we investigated the fundamental limitations of the OCT imaging depth and demonstrated improvement for specific tissues by increasing the OCT center wavelength further into the near-infrared (Chapters 2 and 3). Next, by precise analysis of the OCT signal in relation to the backscattering properties of the tissue, the potential of obtaining more functional information from the OCT signal was explored (Chapters 4 and 5). Finally, we studied swept laser performance and possibilities to optimize it (Chapter 6).

OCT IMAGING DEPTH

One of the current limitations of OCT is its shallow imaging depth which is determined by the technical characteristics of the OCT system and by the optical properties of biological tissues (Equation 3-1). Although the optical properties of biological tissues in some cases can be influenced, for example by optical clearing [2, 3], in general the focus is on improving the technical characteristics of the OCT system. The OCT imaging depth can be improved by optimizing the signal to noise ratio, the coherence length, and the numerical aperture of the sample arm optics (which is incorporated in p_{NA}). However, due to tissue light exposure limits, OCT performance improvement is limited. However, the tissue optical properties change with wavelength, and the optimal central wavelength for the OCT system can be chosen to improve the OCT imaging depth.

The OCT imaging depth depends on the sample properties through two parameters: the light penetration depth and the light backscattering coefficient (Chapter 3). These two parameters both are related to the scattering coefficient of the tissue. Consequently, a change in the scattering coefficient leads to a change in the light penetration depth and in backscattering. For example, if the scattering coefficient is higher, then the light penetration depth is lower. However, a higher scattering coefficient also results in a higher backscattering (for the same scattering phase function). Consequently, a decrease of the scattering coefficient at longer wavelengths does not necessarily leads to the improvement in the OCT imaging

depth. In addition, the absorption coefficient is also wavelength dependent. To achieve optimal OCT performance, all these effects need to be analyzed.

We analyzed the wavelength dependent changes of the light penetration depth in the spectral range of 1000 – 2000 nm (Chapter 2). Due to a lack of reported optical properties of biological tissues in the NIR wavelength region, we used an empirical model (Equation 2-2) to describe the wavelength-dependent changes of the scattering coefficient [4]. This model, which is based on the scattering power parameter SP, characterizes the changes in the scattering with wavelength very well. An advantage of this method is that the SP can be calculated based on values of the scattering coefficients at a few wavelengths only, which does not necessarily need to be in the spectral range of the interest. We performed light transmission measurements with different concentrations of Intralipid and found good agreement with predictions (Fig. 2-4).

The SP parameter for Intralipid was determined with two independent methods: light transmission measurements (Chapter 2) and OCT measurements (Chapter 3). The obtained results are in good agreement: 3.0 ± 0.3 (transmission) and 2.8 ± 0.1 (OCT). In comparison with reported by van Staveren value of SP = 2.4 [4], our results are higher. This difference can be explained by the difference in the particle size distribution of Intralipid (Figure 4-3), which may be due to different producers and (probably) difference in the manufacturing technology of Intralipid. The optical properties of fat emulsions of different brands are reported to be not the same [5], which supports our explanation.

We calculated the NIR light penetration depths for three kinds of biological tissues: sclera, enamel and dentin. The optical properties of these tissues in terms of absorption coefficient and scattering coefficient are highly different. Our analysis shows that improvement in the light penetration depth can be achieved in tissues characterized by a high SP parameter values and low water content. A high SP indicates that a significant reduction of the scattering coefficient can be achieved by shifting to longer wavelengths. For tissues with a low water content, the relatively low light absorption by water in the 1600 nm to 1800 nm spectral region results in a low attenuation coefficient in this spectral range and thus an improvement of the light penetration depth. Our analysis shows that for some biological tissues the improvement in the light penetration depth can be very significant, i.e. 50% for sclera and 80% for enamel (at 1600 nm relative to 1300 nm), which demonstrate the high potential of the 1600 – 1800 nm spectral range for OCT imaging.

To compare and quantify changes in the OCT imaging depth in tissue at 1300 and 1600 nm, we built an OCT setup that can operate with matching technical performance at two wavelengths (Chapter 3). Measurements on high Intralipid concentrations Intralipid demonstrate that at 1600 nm we can achieve a 30 % increase of the OCT imaging depth compared to 1300 nm. This increase is mainly attributed to a reduced scattering coefficient at

1600 nm compared to 1300 nm (Figure 3-3), i.e. lower scattering leads to higher light penetration depth. However, if we compare the changes in the light penetration depth only (transmission measurements, Chapter 2), we see that for high Intralipid concentrations the light penetration depth at 1600 nm is more than 50% better than at 1300 nm (Figure 2-5). This comparison clearly demonstrates that the light backscattering coefficient has a strong influence on the OCT imaging depth.

The backscattering coefficient determines the magnitude of the OCT signal at the surface of the sample, and the attenuation coefficient determines the decay of the OCT signal with depth. Obviously, higher backscattering and lower attenuation lead to a higher OCT imaging depth. However, since the backscattering coefficient is the product of the scattering coefficient and the scattering phase function in the backward direction, a change in the scattering coefficient may in practice be compensated or enhanced by a change in the scattering phase function. This is demonstrated by our Intralipid measurements, where, despite the lower scattering coefficient at 1600 nm, the backscattering coefficients at 1300 nm and 1600 nm are approximately equal (Figure 3-2). This indicates that the lower scattering at 1600 nm is compensated by a larger value of the scattering phase function in the backward direction. Given the same backscattering coefficient, the difference in the OCT imaging depth is mainly determined by the difference in the attenuation coefficient. Because of the higher water absorption at 1600 nm, the OCT imaging depth for low concentrations of Intralipid is larger at 1300 nm. With increasing Intralipid concentration, scattering starts to dominate over absorption. Consequently, for high Intralipid concentrations, OCT with 1600 nm light has a larger OCT imaging depth than 1300 nm.

MEASUREMENTS OF OPTICAL PROPERTIES OF BIOLOGICAL TISSUES

Through the interaction with tissue, properties of light, such as intensity, polarization state and frequency are changed. These changes, which are determined by the optical properties of the tissue, can be related to functional tissue parameters. With ‘functional’ we mean medically relevant information about the condition of the tissue and the processes occurring within the tissue. Consequently, quantitative measurement of optical properties can be used for diagnosis and treatment monitoring [6, 7].

Besides investigating the OCT signal in depth (Chapter 3), we also looked at the OCT signal at the sample surface, which is characterized by the backscattering coefficient. From an OCT measurement of the scattering coefficient and a measurement of the height of the OCT signal at the surface of the scattering medium, we demonstrated in Chapter 4 that we could measure the scattering phase function in the backward direction. Because the scattering phase function is determined by the size and shape of the scattering particles, knowledge of the scattering phase function in the backward direction can provide valuable information about the

microscopic morphology of biological samples. Consequently, physiological processes, which involve changes in the scatterers in tissue, may be detected by OCT.

Our measurements demonstrated that by analysis of the backscatter efficiency of mono-disperse solutions of polystyrene beads, the scattering phase function (in the backward direction) can be related to the particle diameter. Next, we demonstrated that the procedure also can be applied to mixtures of scatterers with different sizes, e.g. Intralipid, resulting in an optically determined average particle diameter. This average diameter is larger than the physical average diameter, but the optically weighted value of the scattering anisotropy g is the only relevant parameter. Indeed, the experimental value we obtain for Intralipid (g = 0.35 ± 0.03) is in good agreement with the value obtained using diffuse reflection spectroscopy (0.32 ± 0.07). For our measurement setup operating at a wavelength of 1300 nm, the maximum particle diameter which can be determined from p_{NA} measurements is approximately 500 nm (corresponding to g=0.5). For larger diameters the oscillations of p_{NA} with wavelength result in non-unique solutions for the particle diameter. This limits the applicability range of our algorithm, but as our method is mainly focused on media with low g that are described by the single scattering model, it complements existing models for OCT that are based on multiple scattering and that enable the extraction of g > 0.8 [8].

An interesting application of the results presented in Chapter 4 is the determination of optical properties of a thin layer of sample or tissue (thickness roughly less than 5 coherence lengths). Due to the convolution of the backscatter profile of the sample with the complex coherence function (Equation 4-1), only a small region of the OCT signal in depth is useful for fitting, which may hamper a precise determination of the attenuation coefficient in thin samples. We demonstrated in Chapter 5 that a priori knowledge of the scattering phase function of the scatterers in the sample (the scattering phase function first was determined on bulk samples) permits the calculation of the scattering coefficient for very thin samples without fitting the decay of the OCT signal in depth. Further research is needed to investigate the difference in the scattering phase function for different tissue types, and the variation from sample to sample for the same tissue types.

Quantitative measurements of the scattering phase function would be ideal. In practise, characteristic parameters as the scattering anisotropy g, and quantitative relative measurements of the backscattering coefficient provide valuable information about changes in the tissue morphology. In contrast to absolute measurements, relative measurements are not limited to small sized scatterers and yield valuable results for large scatterers as well. As an example, changes in the backscattering coefficient due to changes in the size of the scattering structures in the cell, e.g. the nuclei and mitochondria, can be detected, which can be a potential marker suitable for early stage cancer detection [9-11]. Another example is the in-

vitro detection of apoptosis induced changes in cell morphology, which we demonstrated with RPE cells in Chapter 5. Apoptosis induced in a single layer of RPE cells is accompanied with an increase in the backscattering during the development of apoptosis. Previous studies showed that the development of apoptosis leads to an increase of the attenuation coefficient [12]. Our results may give additional information about the biological processes in cells during the development of apoptosis, however more research is needed to validate these experiments and bring this technique to (pre-)clinical practice.

Finally, OCT systems in the wavelength region of 1400 – 2000 nm may be used for the quantitative measurement of the water content of biological tissues, an important functional tissue parameter. Measurement of changes in the hydration state of the biological tissues can be used as diagnostic tool in medicine or in cosmetics [13]. The advantage of water content measurements with OCT is the possibility of extracting spatially resolved spectroscopic information simultaneously with the generation of high resolution images, which can extend the range of biomedical applications of OCT. To determine the water volume fraction in tissue, OCT measurements at two wavelengths with a relatively large difference in the absorption coefficient of water are necessary (a so-called differential absorption technique)[14]. The spectral range of 1400 – 2000 nm is suitable for this kind of measurements due to the large variation of the light absorption by water over this spectral range.

MULTIPLE AND DEPENDENT SCATTERING

Calculations of the scattering coefficient in our optical transmission (Chapter 2) and OCT experiments (Chapter 3) are based on ballistic light. In the simplest model, the amount of light measured on the detector is described by the fraction of non-scattered (ballistic) light in depth. For OCT, the detected light experiences a single backscattering event, and the theoretical description is generally called the single scattering approximation (although single back-scattering would be more appropriate). In our experiments, for low Intralipid concentrations the scattering coefficient increases linearly with concentration, which is expected for low-density media. However, for concentrations of approximately 5 % and higher, a deviation from the linear dependence is observed (see Fig. 2-3 and Fig. 3-3). Such a deviation is observed for both light transmission and OCT measurements, and can be explained by the presence of multiple and dependent scattering effects.

Multiple scattering manifests itself by an increase of the detected signal compared to a measurement in the single backscattering regime (OCT) or to a measurement in the ballistic regime (optical transmission). Although the long distance between the sample and the detector for transmission measurements, and the combination of coherent and confocal gates for OCT measurements suppresses the detection of scattered light (transmission measurements) and multiple scattered light (OCT measurements), their contribution may still be present in the

detected light. With increasing scattering coefficient, the amount of multiple scattered light also increases, and the influence of the multiple scattering on the detected signal becomes stronger. In addition to multiple scattering, also the distance between scatterers has a strong influence on the detected signal. For large distances (much larger than the wavelength), the scattering coefficient can be described by the independent scattering model, i.e. the light scattering from the ensemble of scatterers is the sum of the scattering of individual scatterers. For small inter-particle distances, i.e. distances comparable with the wavelength, the electric fields scatterered from multiple particles interact coherently. This so-called concentration dependent scattering is generally present in high concentration samples and leads to a reduction of the scattering coefficient [15].

Although dependent and multiple scattering both influence the measured attenuation, we hypothesize that their contributions can still be separated using OCT measurements. The contribution of multiple scattered light to the OCT signal increases with depth (especially for tissues with larger g values)[16]. On the other hand, for a distance of a few coherence lengths from the surface of the sample, multiple scattering effects are negligible. Consequently, the non-linear dependence of the backscattered power from the surface of the sample with increasing Intralipid concentration is only due to dependent scattering. In other words, at zero depth only dependent scattering is present, whereas at larger depths – both dependent and multiple scattering are present.

Figure 7-1 shows a comparison of the changes of the measured scattering coefficient μ_s and the square of the OCT signal amplitude at zero depth $|a_{OCT}|^2$ (which is proportional to backscattered power) for varying Intralipid concentrations. Please note that although $|a_{OCT}|^2$ is not affected by multiple scattering, $|a_{OCT}|^2$ deviates from the expected linear relation (as depicted by the dashed line), which indicates the effect of dependent scattering to the OCT signal at high concentrations of Intralipid. Furthermore, the deviation from the linear dependence occurs at lower Intralipid concentrations for the measured scattering coefficient than for the square of the OCT signal amplitude, which means that the non-linear behaviour of the measured attenuation coefficient is affected by both multiple and dependent scattering. A comparison of the relation between $|a_{OCT}|^2$ and μ_s may be used for analysis of contribution of dependent and multiple scattering effects to the OCT measurements of μ_s. In addition, the effect of dependent scattering on the scattering phase function (and the scattering anisotropy g) still has to be taken into account to come to a final conclusion.

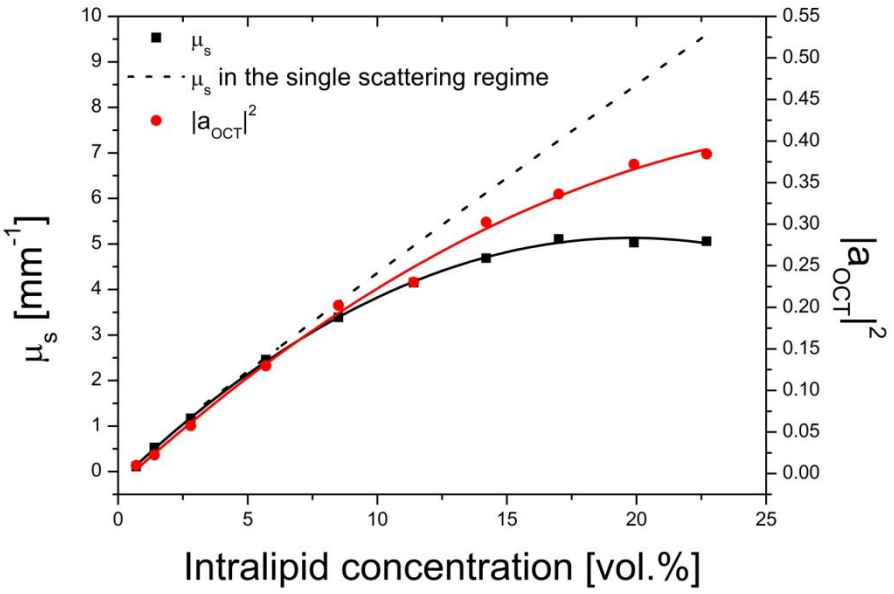

Figure 7-22. Comparison of concentration dependent changes of the scattering coefficient μ_s and square of the OCT signal amplitude at zero depth ($|a_{OCT}|^2$) for varying Intralipid concentration.

Due to the broad particle size distribution in Intralipid, measurements with monodisperse polystyrene microspheres can give more quantitative information about the effects of size and concentration of scatterers on dependent and multiple scattering. In the next section we propose a model to describe the effect of dependent scattering on the measured scattering coefficient.

DEPENDENT SCATTERING FORMALISM

In the theoretical approaches in this thesis, tissue is modelled as a collection of non-interacting spheres because for such a system the optical properties can be calculated using e.g. Mie theory. This model implies that the absorption and scattering coefficients increase linearly with particle concentration [17]. In reality, biological tissues are highly heterogeneous condensed media, whose optical properties are difficult to model. Indeed, real tissue is certainly not a dilute suspension of independently scattering spheres. This gap between theory and reality is partly bridged by using Intralipid as a tissue simulating phantom: it is well known that the optical properties of Intralipid resemble those of tissue [18] and that at least dilute suspensions are adequately described by Mie theory, integrated over the size distribution of Intralipid [4], see also Chapter 4. Nevertheless, as in real tissue, when the suspension becomes denser, the positions of the individual particles become correlated (even though their placement remains random). This implies that the scattering phase function of the suspension is no longer equal to the weighted average of the scattering phase function of the Intralipid

particles because now interference effects need to be considered. As is commonly done in statistical physics [19] we introduce a structure factor $S(\theta)$ that accounts for these correlations. Where the (back-)scattering coefficient is obtained in the independent regime by integrating the phase function $p(\theta)$ over the detection NA, or 4π respectively, in the dependent regime the product of $p(\theta)$ and $S(\theta)$ is integrated, see [20] and [21] for details. Nevertheless, obtaining the structure factor for tissues is not a trivial task. In the present context of Intralipid, we use the previously determined averaged optical radius of 233 nm (Chapter 4) to calculate the concentration-dependent structure factor for spheres in the Percus-Yevick approximation [22].

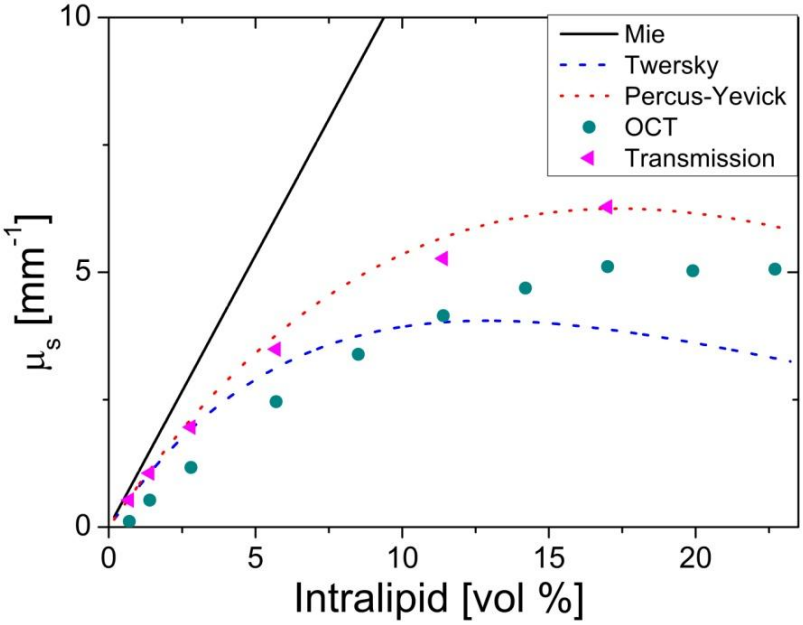

Figure 7-23. The scattering coefficient of Intralipid at 1300 nm: experimental results (light transmission and OCT measurements) and theoretical predictions (Mie, Twersky and Percus-Yevick models calculations).

An analytically more insightful approach can be taken from the results of Twersky [23] that describes the dependent scattering coefficient in terms of the independent scattering coefficient by introducing a pack-factor w: $\mu_{s,dep} = \mu_s \cdot w$. For spheres, w reads:

$$w = \frac{(1-H)^4}{(1+2H)^2} \tag{7-1}$$

This formalism was applied with some success to ultrasonic backscattering from blood [24].

We applied both approaches to our measurements on Intralipid at 1300 nm, as shown in Figure 7-2. As can be seen, the Percus-Yevick approximation matches light transmission measurements of μ_s of Intralipid very well. The OCT results yield lower values, which probably can be explained by additional influence of the multiple scattering, which is negligible for

transmission measurements. Twersky's approximation is accurate only for low concentrations of Intralipid. These results suggest that the Percus-Yevick model can provide an accurate description of dependent scattering effects during measurements of optical properties of samples with high concentration of scatterers.

SWEPT SOURCE OCT DEVELOPMENT

Besides the determination of tissue optical properties, the technical development of OCT systems is of great importance. In this thesis we demonstrated a wavelength swept laser based on CW Ti:Sapphire laser (Chapter 6). Swept lasers operating in the spectral range of 800 nm can find many applications in medicine, e.g. for the imaging of the posterior segment of the human eye. Sweeping was achieved by implementation of an acousto-optical tunable filter (AOTF) in the laser cavity. Swept laser characteristics relevant for OCT are: instantaneous linewidth, spectral tuning range and the sweeping frequency. The instantaneous linewidth is in general a characteristic of the tunable filter and should be properly chosen during the design of the swept laser. Two other parameters, the spectral tuning range and the sweeping frequency, can be adjusted by changing the electronic drive signal. For our Ti-Sapphire swept laser we demonstrated that these two parameters depend on each other, i.e. a higher sweeping frequency leads to a narrower tuning range and vice versa. For 8 kHz sweeping frequency the tuning range is 10 nm, and for 450 Hz – 185 nm. We attributed this phenomenon to the fact that a certain time is necessary to build up lasing in the laser cavity, i.e. the light has to pass many times through the gain medium to be amplified above the lasing threshold (approximately 250 times). This relation between tuning speed and the product of the spectral width and the sweeping frequency is a disadvantage for the use of the Ti-Sapphire lasers for SS-OCT, which requires a high sweeping rate over a broad spectral range.

In general, tunable filters induce wavelength dependent optical losses in the laser cavity, which change the laser dynamics. If the wavelength is scanned too fast, i.e. the time that light with a certain wavelength can pass through the filter is not enough to complete necessary number of cavity round-trips, then lasing does not start. New developments on Fourier-Domain Mode Locking (FDML) have demonstrated that these limitations currently can be overcome [25]. Also, the swept-laser performance can be improved by using a lasing medium with a higher gain, which reduces the number of necessary round-trips, or to build shorter laser cavity to reduce the time necessary for one cavity round-trip. Additionally, the possibility of electronic tuning gives the opportunity to optimise the laser output for OCT imaging (control over the shape of the spectrum, linear tuning in the k-space to eliminate the data resampling).

Although AOTF's have disadvantages (the induced RF shift with each round trip, limited tuning speed), use of an AOTF for the swept operation of the light source is being actively investigated [26]. Furthermore, alternative ways to increase the sweeping frequency exist. For

example, an optical parametric oscillator (OPO) pumped with our swept Ti:Sapphire laser, and periodically poled lithium niobate crystal as nonlinear medium for wavelength conversion, is one of the possibilities [27, 28]. We estimated that 5 nm tuning bandwidth around 800 nm for swept Ti:Sapphire laser can give an OPO sweep output from 1600 nm to 1800 nm. In such a way, a swept light source with sweeping frequency above 10 kHz and tuning range of approximately 200 nm (1600 – 1800 nm) can be created.

An important issue in OCT development is system miniaturization. Compact and low cost OCT systems can increase the accessibility of OCT technology and lead to creation of new applications. The integration of optical devices on semiconductor material received significant attention in the last decades. Different integration approaches and different material systems were demonstrated. For SD-OCT systems a chip-based arrayed-waveguide grating (AWG) spectrometer was demonstrated in OCT imaging [29].

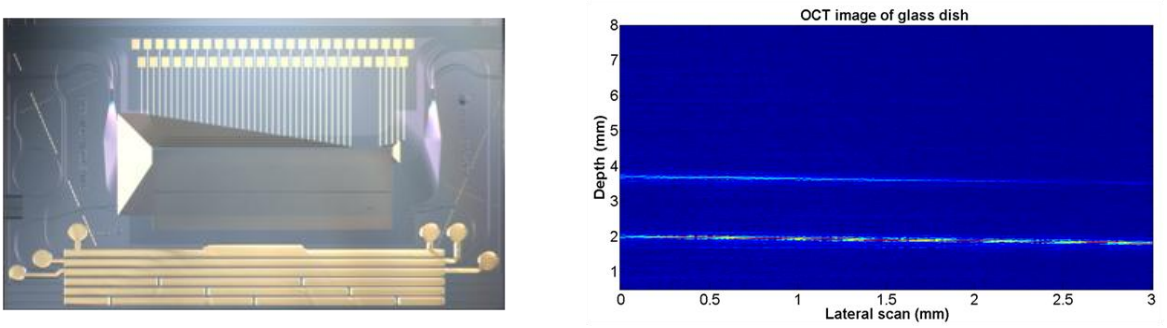

Figure 7-24. Left: photograph of the integrated tunable quantum-dot laser for OCT in the 1.7 um wavelength region (size 10x6 mm); Right: OCT image of the glass plate obtained with this laser.

Recently, development of integrated tunable quantum-dot laser in the 1700 nm wavelength region (1685 – 1745 nm) was reported [30]. For wavelength tuning, an electro-optical tunable filter based on an AWG with electro-optically tunable phase modulators in the arms of the AWG was used. Interferometric imaging of this integrated swept-source was demonstrated with an open air Michelson interferometer coupled to the swept source. An OCT image of a glass plate obtained with this system is presented in Figure 7-3. Full Integration of a swept laser and an interferometer on a single chip is challenging, but a very interesting approach for the further development of OCT systems.

CONCLUDING REMARKS

The work presented in this thesis covers a range of issues encountered in current development of OCT technology. We investigated the possibilities to improve OCT performance (long wavelengths OCT, swept source development), and to extract more information about optical properties of the scattering samples (determination of scattering anisotropy parameter, measurements of the scattering properties of thin samples). The results we obtained demonstrate advances in these areas and raise new questions for further research. Many aspects of light-tissue interaction and technical performance of OCT systems need to be investigated to realize the full potential of OCT and bring it to clinical practice.

REFERENCES

1. S. Jackle, N. Gladkova, F. Feldchtein, A. Terentieva, B. Brand, G. Gelikonov, V. Gelikonov, A. Sergeev, A. Fritscher-Ravens, J. Freund, U. Seitz, S. Schroder, and N. Soehendra, "In vivo endoscopic optical coherence tomography of the human gastrointestinal tract - Toward optical biopsy," Endoscopy **32**, 743-749 (2000).
2. S. G. Proskurin, and I. V. Meglinski, "Optical coherence tomography imaging depth enhancement by superficial skin optical clearing," Laser Physics Letters **4**, 824-826 (2007).
3. V. V. Tuchin, "A clear vision for laser diagnostics (review)," IEEE Journal of Selected Topics in Quantum Electronics **13**, 1621-1628 (2007).
4. H. J. van Staveren, C. J. M. Moes, J. van Marie, S. A. Prahl, and M. J. C. van Gemert, "Light scattering in Intralipid-10% in the wavelength range of 400-1100 nm," Applied Optics **30**, 4507-4514 (1991).
5. R. Michels, F. Foschum, and A. Kienle, "Optical properties of fat emulsions," Optics Express **16**, 5907-5925 (2008).
6. C. L. Darling, G. D. Huynh, and D. Fried, "Light scattering properties of natural and artificially demineralized dental enamel at 1310 nm," Journal of Biomedical Optics **11** (2006).
7. C. Xu, J. M. Schmitt, S. G. Carlier, and R. Virmani, "Characterization of atherosclerosis plaques by measuring both backscattering and attenuation coefficients in optical coherence tomography," Journal of Biomedical Optics **13**, 034003-034008 (2008).
8. D. Levitz, L. Thrane, M. H. Frosz, P. E. Andersen, C. B. Andersen, J. Valanciunaite, J. Swartling, S. Andersson-Engels, and P. R. Hansen, "Determination of optical scattering properties of highly-scattering media in optical coherence tomography images," Optics Express **12**, 249-259 (2004).
9. R. Drezek, M. Guillaud, T. Collier, I. Boiko, A. Malpica, C. Macaulay, M. Follen, and R. Richards-Kortum, "Light scattering from cervical cells throughout neoplastic progression: influence of nuclear morphology, DNA content, and chromatin texture," Journal of Biomedical Optics **8**, 7-16 (2003).
10. T. Q. Xie, M. L. Zeidel, and Y. T. Pan, "Detection of tumorigenesis in urinary bladder with optical coherence tomography: optical characterization of morphological changes," Optics Express **10**, 1431-1443 (2002).
11. J. R. Mourant, M. Canpolat, C. Brocker, O. Esponda-Ramos, T. M. Johnson, A. Matanock, K. Stetter, and J. P. Freyer, "Light scattering from cells: the contribution of the nucleus and the effects of proliferative status," Journal of Biomedical Optics **5**, 131-137 (2000).
12. F. van der Meer, D. Faber, M. Aalders, A. Poot, I. Vermes, and T. van Leeuwen, "Apoptosis- and necrosis-induced changes in light attenuation measured by optical coherence tomography," Lasers in Medical Science **25**, 259-267.
13. S.L.Zhang, C. L. Meyers, S. Kumar, and M. H. Thomas, "Near infrared imaging for measuring and visualizing skin hydration. A comparison with visual assessment and electrical methods," Journal of Biomedical Optics **10**, 031107 (2005).
14. J. M. Schmitt, S. H. Xiang, and K. M. Yung, "Differential absorption imaging with optical coherence tomography," Journal of the Optical Society of America A-Optics Image Science and Vision **15**, 2288-2296 (1998).
15. J. Kalkman, A. V. Bykov, D. J. Faber, and T. G. van Leeuwen, "Multiple and dependent scattering effects in Doppler optical coherence tomography," Optics Express **18**, 3883-3892.
16. L. Thrane, H. T. Yura, and P. E. Andersen, "Analysis of optical coherence tomography systems based on the extended Huygens-Fresnel principle," Journal of the Optical Society of America A-Optics Image Science and Vision **17**, 484-490 (2000).
17. H. C. v. d. Hulst, *Light Scattering by small particles,* (Dover Publications Inc, New York, 1981).

18. B.W.Pogue, M.S.Patterson, "Review of tissue simulating phantoms for optical spectroscopy, imaging and dosimetry," Journal of Biomedical Optics **11**, 041102 (2006).
19. P. Debye, J. H. R. Anderson, and H. Brumberger, "Scattering by an Inhomogeneous Solid. II. The Correlation Function and Its Application," Journal of Applied Physics **28**, 679-683 (1957).
20. G. Gobel, "Dependent scattering effects in latex-sphere suspensions," Waves in Random Media **5**, 413 (1995).
21. J. D. Cartigny, Y. Yamada, and C. L. Tien, "Radiative Transfer With Dependent Scattering by Particles: Part 1---Theoretical Investigation," Journal of Heat Transfer **108**, 608-613 (1986).
22. M. S. Wertheim, "Exact Solution of the Percus-Yevick Integral Equation for Hard Spheres," Physical Review Letters **10**, 321-323 (1963).
23. V. Twersky, "Multiple Scattering of Waves and Optical Phenomena," Journal of the Optical Society of America **52**, 145-169 (1962).
24. L.Y.L.Mo, I-Y. Kuo, K.K. Shung, L. Ceresne, R.S.C. Cobbold. , "Ultrasound scattering from blood with hematocrits up to 100%. ," IEEE Transactions on Biomedical Engineering **41**, 91-95 (1994).
25. R. Huber, M. Wojtkowski, and J. G. Fujimoto, "Fourier Domain Mode Locking (FDML): A new laser operating regime and applications for optical coherence tomography," Optics Express **14**, 3225-3237 (2006).
26. A. Silva, K. J. Boller, and I. D. Lindsay, "Wavelength-swept Yb-fiber master-oscillator-power-amplifier with 70nm rapid tuning range," Optics Express **19**, 10511-10517.
27. M. J. Missey, V. Dominic, P. E. Powers, and K. L. Schepler, "Periodically poled lithium niobate monolithic nanosecond optical parametric oscillators and generators," Optics Letters **24**, 1227-1229 (1999).
28. D. Stothard, I. Lindsay, and M. Dunn, "Continuous-wave pump-enhanced optical parametric oscillator with ring resonator for wide and continuous tuning of single-frequency radiation," Optics Express **12**, 502-511 (2004).
29. V. D. Nguyen, B. I. Akca, K. Wörhoff, R. M. de Ridder, M. Pollnau, T. G. van Leeuwen, and J. Kalkman, "Spectral domain optical coherence tomography imaging with an integrated optics spectrometer," Optics Letters **36**, 1293-1295.
30. Y. J. B.W. Tilma, J.Kotani, E.Smalbrugge, H.P.M.M.Ambrosius, P.J.Thijs, X.J.M.Leijtens, R.Notzel, M.K.Smit, and E.A.J.M.Bente, "Integrated tunable quantum-dot laser for optical coherence tomography in the 1.7 um wavelength region," IEEE Journal Quantum Electronics **47** (2011).

LIST OF PUBLICATIONS

V.M.Kodach, J.Kalkman, D.J.Faber, and T.G.van Leeuwen
“Quantitative comparison of the OCT imaging depth at 1300 and 1600 nm”
Biomedical Optics Express, Vol. 1, Issue 1, pp. 176-185 (2010)

V.M.Kodach, D.J.Faber, J.van Marle, T.G.van Leeuwen, J.Kalkman
‘‘Determination of the scattering anisotropy with optical coherence tomography’’
Optics Express, Vol.19, Issue 7, pp. 6131-6140 (2011)

V.M.Kodach, D.J.Faber, T.G.van Leeuwen
“Wavelength swept Ti:Sapphire laser”
Optics Communications, 281(19), pp.4975-4978 (2008)

M.Amzayyb, R.R.van den Bos, V.M.Kodach, D.M.de Bruin, T.Nijsten, H.A.M. Neumann, M.J.C.van Gemert
“Carbonized blood deposited on fibres during 810, 940 and 1470 nm endovenous laser ablation: thickness and absorption by optical coherence tomography”
Lasers in Medical Science, 2010;25(3), pp.439-447

D.M.de Bruin, R.H.Bremmer, V.M.Kodach, R.de Kinkelder, J.van Marle, T.G. van Leeuwen, D.J.Faber
“Optical phantoms of varying geometry based on thin building blocks with controlled optical properties”
Journal of Biomedical Optics, 15(2), 025001 (2010)